Structural Characterization of III-V Bismide Materials

Grown by Molecular Beam Epitaxy

by

Rajeev Reddy Kosireddy

A Dissertation Presented in Partial Fulfillment
of the Requirements for the Degree
Doctor of Philosophy

Approved April 2020 by the
Graduate Supervisory Committee:

Shane R. Johnson, Chair
David J. Smith
Terry Alford
Emmanuel Soignard

ARIZONA STATE UNIVERSITY

May 2020

ABSTRACT

III-V-bismide semiconductor alloys are a class of materials with applications in the mid and long wave infrared spectrum. The quaternary alloy InAsSbBi is attractive because it can be grown lattice-matched to commercially available GaSb substrates, and the adjustment of the Bi and Sb mole fractions enables both lattice constant and bandgap to be tuned independently. This dissertation provides a comprehensive study of the surface morphology and the structural and chemical properties of InAsSbBi alloys grown by molecular beam epitaxy.

210 nm thick InAsSbBi layers grown at temperatures from 280 °C to 430 °C on (100) on-axis, (100) offcut 1° to (011), and (100) offcut 4° to (111)A GaSb substrates are investigated using Rutherford back scattering, X-ray diffraction, transmission electron microscopy, Nomarski optical microscopy, atomic force microscopy, and photoluminescence spectroscopy. The results indicate that the layers are coherently strained and contain dilute Bi mole fractions.

Large surface droplets with diameters and densities on the order of 3 μm and 10^6 cm^{-2} are observed when the growth is performed with As overpressures around 1%. Preferential orientation of the droplets occurs along the $[01\bar{1}]$ step edges offcut (100) 1° to (011) substrate. The surface droplets are not observed when the As overpressure is increased to 4%. Small crystalline droplets with diameters and densities on the order of 70 nm and 10^{10} cm^{-2} are observed between the large droplets for the growth at 430°C. Analysis of one of the small droplets indicates a misoriented zinc blende structure composed of In, Sb, and Bi, with a 6.543 ± 0.038 Å lattice constant.

Lateral variation in the Bi mole fraction is observed in InAsSbBi grown at high temperature (400 °C, 420 °C) on (100) on-axis and (100) offcut 4° to (111)A substrates, but is not observed for growth at 280 °C or on (100) substrates that are offcut 1° to (011). Improved crystal and optical quality is observed in the high temperature grown InAsSbBi and $CuPt_B$ type atomic ordering on the {111}B planes is observed in the low temperature grown InAsSbBi. Strain induced tilt is observed in coherently strained InAsSbBi grown on offcut substrates.

DEDICATION

To my grandparents Raghava Reddy and Kousalya, Laxma Reddy and Vimala, parents Vishnu Vardhan Reddy and Kusumalatha , and brother Rohith Reddy.

ACKNOWLEDGMENTS

I would like to express my gratitude to my advisor Dr. Shane Johnson for providing me this wonderful opportunity, guiding me throughout the process, and teaching me invaluable skills like effective writing and critical thinking.

I would like to deeply thank Dr. David Smith for being generous and supportive through the tough times, and for all the interesting discussions throughout the process. I would like to extend my special thanks to Dr. Emmanuel Soignard for all the guidance and experimental support. I would like to thank Dr. Terry Alford for the time and effort put into this work.

Many thanks to my friends in the compound semiconductors group who helped me with my research; Stephen Schaefer (for all the fascinating samples and support), Arvind Shalindar (for initial training and help), Marko Milosavljevic (for interesting discussions). I would like to acknowledge Dr. Karl Weiss and Dr. Manuel Ronald for training me on the microscopes. I would like to acknowledge Christine Quintero for all the academic advising support throughout the program.

I owe my heartfelt thanks to my parents Vishnu Vardhan Reddy and Kusumalatha, my brother Rohith Reddy, for the endless love and emotional support throughout. Many thanks to my best friend Shreyas Gummadi for all the inspiration and backing through the tough times. Thanks to my wolfpack friends - Arjun Moturi, Prajwal Reddy, Rahul Reddy, Sravan Kumar, Sharath Reddy, Pradeep Yelimala, Ram MVRK, Jaswin Phirangi for the strength you all have provided me. Thanks to my Telugu gang – Sanjana Reddy, Revanth Reddy, Manasa Reddy, Lahari Reddy, Vishnu Budama, Shantan Reddy, Kalyan Juluru for

the fun times and motivation. Thanks to my current and former colleagues at ASU for the care and help throughout this wonderful journey.

I gratefully acknowledge financial support through the National Science Foundation, Grant No. DMR-1410393 and Air Force Research Laboratory under agreement number FA9453-19-2-0004. I gratefully acknowledge the use of facilities in the Eyring Materials Center at Arizona State University.

TABLE OF CONTENTS

Page

LIST OF TABLES

LIST OF FIGURES

Figure Page

Figure Page

LIST OF ABBREVIATIONS

MBE Molecular Beam Epitaxy

RBS Rutherford Backscattering Spectrometry

XRD X-Ray Diffraction

TEM Transmission Electron Microscopy

BF Bright Field

DF Dark Field

HAADF High Angle Annular Dark Field

FFT Fast Fourier Transform

DIC Differential Interference Contrast

AFM Atomic Force Microscopy

PL Photoluminescence

1. INTRODUCTION

Infrared radiation (IR) refers to that portion of the electromagnetic spectrum in the wavelength range of 750 nm to 1 mm. Further, the infrared spectrum is sub-divided into several regions[1] – the near IR with wavelengths from 0.7 μm to 1 μm; the short-wavelength IR with wavelengths from 1 μm to 3 μm; the mid-wavelength IR with wavelengths from 3 μm to 5 μm; the long-wavelength IR with wavelengths from 8 μm to 12 μm; and the very long- wavelength IR with wavelengths[2] beyond 12 μm as illustrated in Figure 1.

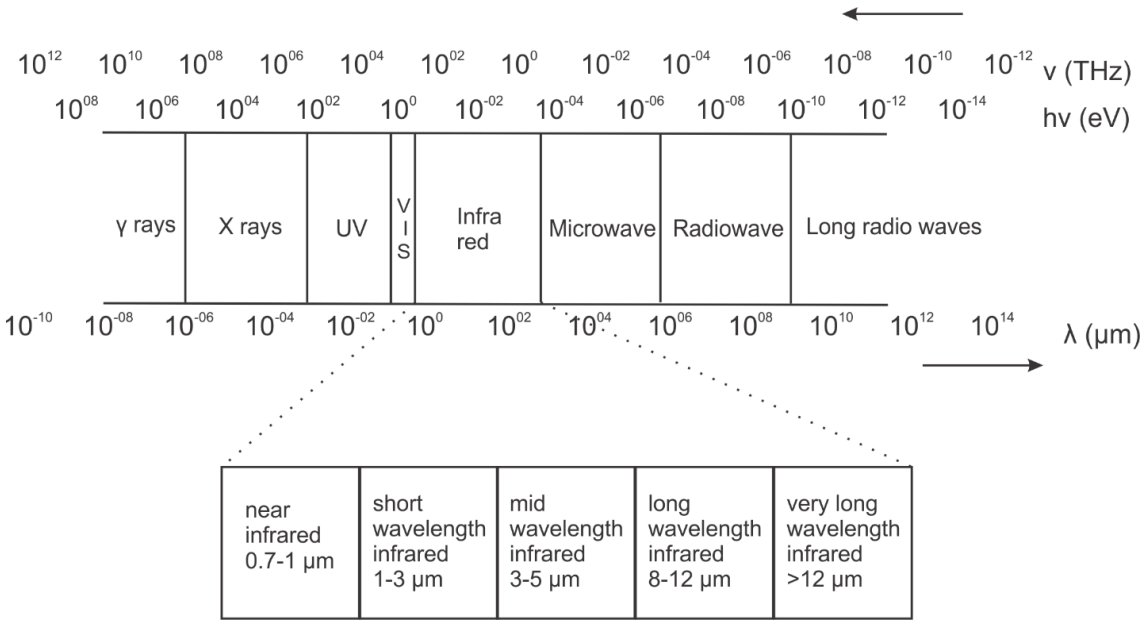

Figure 1: Classification of the infrared spectrum. Regions of increasing wavelength are designated as near wave infrared, short wave infrared, mid wave infrared, long wave infrared and very long wave infrared.

The Atmospheric absorption spectrum as a function of wavelength is shown in Figure 2. Photons with wavelengths from 3.0 μm to 5.0 μm and 8 μm to 12 μm are feebly

absorbed by Earth's atmosphere and hence are attractive for infrared applications. For commercial free space applications mid and long-wavelength infrared windows are targeted because of low atmospheric signal attenuation.

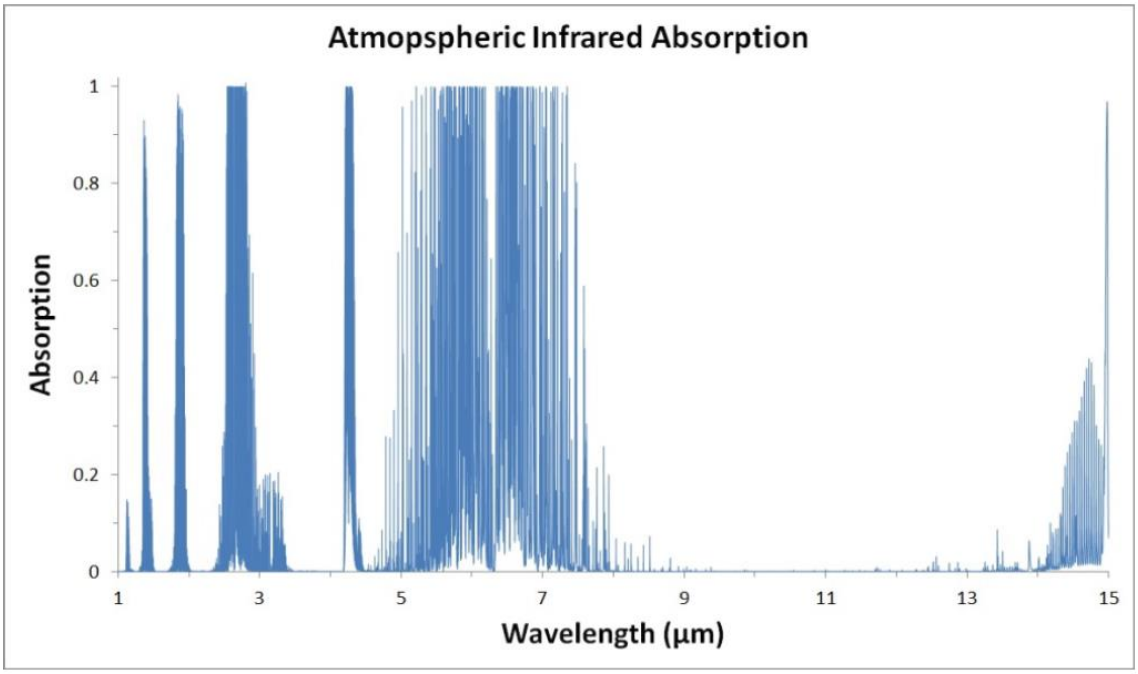

Figure 2: Atmospheric absorption spectrum with absorption on the vertical axis as a function of wavelength on the horizontal axis. The atmosphere is transparent to light in the 3.0-5.0 and 8.0-12.0 µm wavelength ranges.

Optoelectronics refers to the branch of semiconductor electronics focusing on light-emitting and light detecting devices. Development of infrared photodetectors and emitters operating in the mid-wavelength IR and long-wavelength IR is desired for several applications, including, navigation, night vision, launch detection, communications, imaging, and spectroscopy.[2] An emerging class of materials for mid-IR and long-IR applications are the III-V-bismide alloys. The most commonly used elements in the III-V-

Bi alloys are highlighted as Ga (yellow), In (red), As (blue), Sb (green), and Bi (orange) as shown in the section of the periodic table in Figure 3.

4 1.57 90 pm **Be** 9.012182	5 2.04 82 pm **B** 10.811	6 2.55 77 pm **C** 12.0107	7 3.04 75 pm **N** 14.0067	8 3.44 73 pm **O** 15.9994
12 1.31 130 pm **Mg** 24.3050	13 1.61 118 pm **Al** 26.9815386	14 1.90 111 pm **Si** 28.0855	15 2.19 106 pm **P** 30.973762	16 2.58 102 pm **S** 32.065
30 1.65 131 pm **Zn** 65.38	31 1.81 126 pm **Ga** 69.723	32 2.01 122 pm **Ge** 72.64	33 2.18 119 pm **As** 74.92160	34 2.55 116 pm **Se** 78.96
48 1.69 148 pm **Cd** 112.411	49 1.78 144 pm **In** 114.818	50 1.96 141 pm **Sn** 118.710	51 2.05 138 pm **Sb** 121.760	52 2.10 135 pm **Te** 127.60
80 2.00 149 pm **Hg** 200.59	81 2.04 148 pm **Tl** 204.3833	82 2.33 147 pm **Pb** 207.2	83 2.02 146 pm **Bi** 208.98040	84 2.00 146 pm **Po** 208.9824

Figure 3: A section of the periodic table highlighting the elements Ga (yellow), In (red), As (blue), Sb (green), and Bi (orange) used in III-V-Bi epilayers and substrates examined in this work. The element symbol, atomic number, electronegativity value, covalent radius, and atomic mass are shown for every element.

Bismuth is a naturally occurring, stable element, and is relatively non-toxic when compared to mercury (Hg), thallium (Tl), antimony (Sb), lead (Pb) and polonium (Po). Bismuth has the largest atomic number and size of all group-V elements. For many years, bismuth alloyed with conventional III-V semiconductors and its effect on the material electronic band structure has been examined. Bismuth incorporation in InAs reduces the

room-temperature bandgap energy of InAs by 51 meV/% Bi,[3] which is a much greater rate than Sb at 9.3 meV/% Sb.[4] In particular the quaternary alloy InAsSbBi lattice-matched to commercially available GaSb substrates spans bandgap energies from 0.32 to 0.10 eV (4 to 12 μm) at low temperature and 0.27 to 0.042 eV (5 to 30 μm) at room temperature. The InAsSbBi material system offers independent control of strain and bandgap energy by independently adjusting the Sb and Bi mole fractions and improved hole confinement can be achieved compared to InAsSb alone.

The low-temperature bandgap energy of III-V semiconductor alloys is plotted as a function of lattice constant in Figure 4. The quaternary alloy InAsSbBi, indicated by the red shaded region,[5] can be grown lattice-matched to GaSb (lattice constant[6] of 6.0959 Å) and is limited only by a practical maximum compressive strain of 2% for the epitaxial growth of smooth layers, which corresponds to a Matthews-Blakeslee critical thickness[7] of ~10 nm. The corresponding lattice-matched endpoint ternaries InAsSb and InAsBi span a wavelength range of approximately 3–10 μm. InAsSbBi is a highly mismatched alloy with isoelectronic group-V elements of different sizes, ionicities, and electronegativities. While these highly mismatched alloy semiconductors have interesting properties, large miscibility gaps[8] are a challenge to growth of high optical quality alloys. Previous work has reported microstructural and morphological studies of ternary III-V-Bi and III-V-N alloy systems, namely GaAsBi,[9,10,11] GaSbBi,[12,13] InAsBi,[14] and (In,Ga)AsN.[15] However, the microstructural properties of quaternary III-V-Bi alloys have received scant attention. Hence, it is important to investigate the microstructural properties of the InAsSbBi alloy

system to optimize growth conditions and optical performance of this emerging infrared material system.

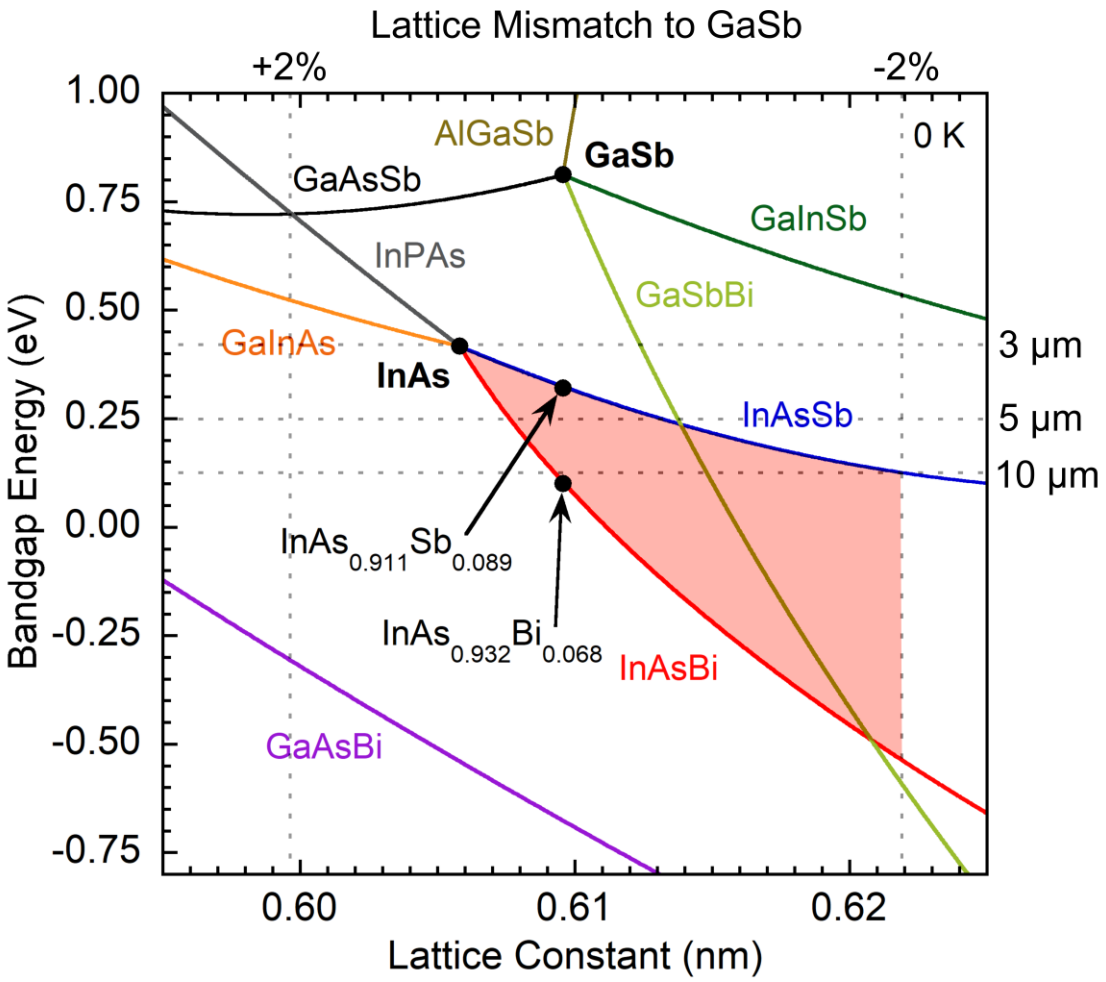

Figure 4: Low temperature bandgap energy as a function of lattice constant for III-V compounds and alloys in the region of 6.1 Å lattice constants. The quaternary alloy InAsSbBi is indicated by the red shaded region. The ternary compounds InAsSb and InAsBi lattice matched to GaSb are shown as black circles and span 4 to 10 μm respectively.

Several pseudomorphic, 210 nm thick, narrow bandgap InAsSbBi layers are grown by molecular beam epitaxy on GaSb substrates at temperatures from 280 °C to 430 °C, Bi/In flux ratios ranging from 0.050 to 0.100, Sb/In flux ratios ranging from 0.120 to 0.126, and As/In flux ratios ranging from 0.940 to 1.300. Growths are performed on both on axis (100) and offcut (100) 1° to (011), (100) 4° to (111) A GaSb substrates. The samples are grown with near-stoichiometric V/III flux ratios of ~ 1.01 to aid in the incorporation of bismuth that typically surface segregates due to its large size. The growth conditions for each sample are provided in Table 1.

The nominal cross section of all the samples studied is shown in Figure 5 and consists of a 500 nm GaSb buffer, a 10 nm InAs/10 nm AlSb partially strain balanced barrier, the InAsSbBi active region, and a terminating 10 nm AlSb/10 nm InAs barrier/cap layer. The GaSb buffer layer is grown at 500 °C except for the last 70 nm where the substrate temperature is reduced to the growth temperature of the InAsSbBi layer,[5] which in the samples studied ranges from 280 to 430 °C. The strain balanced barrier layers provide electrical confinement for the photo generated carriers as indicated by the band offsets for the sample structure as shown in Figure 6. The InAs cap layer also provides a stable surface layer to protect the AlSb from oxidation.

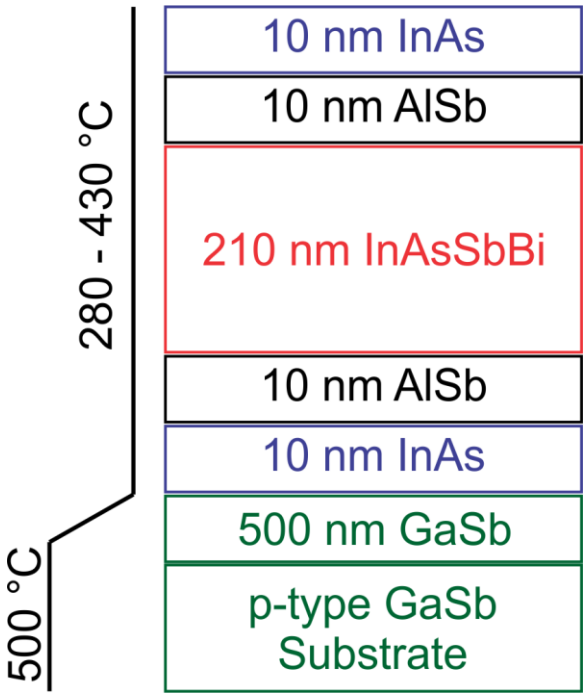

Figure 5: Nominal growth cross-section of bulk InAsSbBi samples. The substrate temperature is reduced from 500 °C to the InAsSbBi growth temperature (280 to 430 °C) during the GaSb buffer growth.

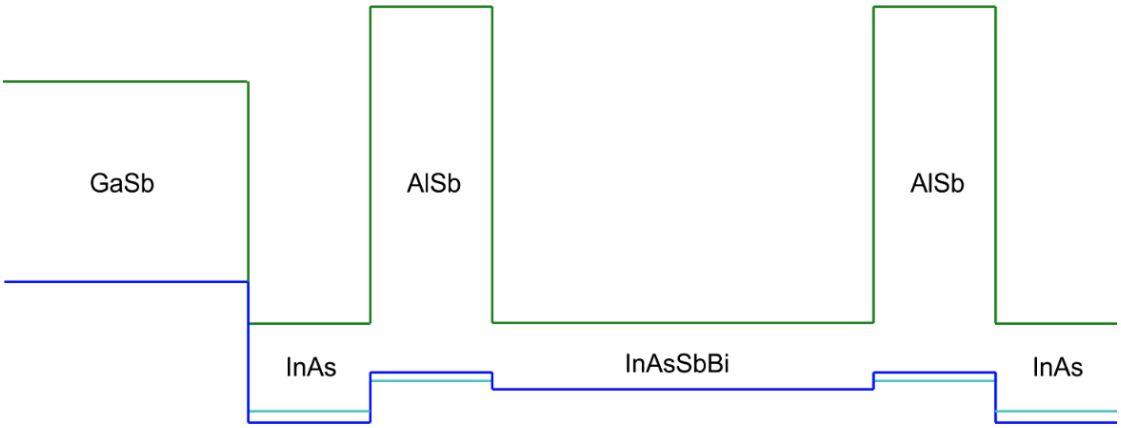

Figure 6: Sample band offset diagram illustrating the alignment of conduction (green), heavy hole (dark blue), and light hole (light blue) bands in the InAsSbBi sample. InAsSbBi exhibits a type-II band alignment with most other III-V materials, including the GaSb substrate.

Table 1. Bulk InAsSbBi sample name, MBE growth temperature, V/III flux ratios, GaSb substrate orientation, and surface morphology.

Sample	Growth temperature (°C)	Flux Ratios			GaSb substrate orientation	Surface morphology
		Bi/In	Sb/In	As/In		
A	430	0.100	0.120	0.911	(100) on axis	Light haze
B	420	0.050	0.120	0.940	(100) on axis	Smooth
C	400	0.050	0.120	0.940	(100) on axis	Smooth
D	400	0.050	0.120	0.911	(100) on axis	Light haze
E	400	0.050	0.120	0.911	(100) 1° to (011)	Light haze
F	400	0.050	0.105	0.911	(100) 4° to (111) A	Light haze
G	280	0.016	0.080	0.970	(100) on axis	Smooth

In this work the experimental methods used to characterize the InAsSbBi layers are discussed in Chapter 2, which are Rutherford backscattering spectrometry (RBS), High resolution X-ray diffraction (XRD), transmission electron microscopy (TEM), Nomarski optical microscopy, atomic force microscopy (AFM), and photoluminescence spectroscopy. The impact of the growth temperature and As/In flux on the structural properties and surface morphology of nearly lattice matched InAsSbBi are examined in Chapter 3. The impact of substrate offcut on the structural properties and surface morphology of nearly lattice matched InAsSbBi is examined in Chapter 4. The crystal and optical quality of InAsSbBi grown at high (400 °C) and low (280 °C) temperature is compared and discussed in Chapter 5.

2. GROWTH METHOD AND CHARACTERISATION TECHNIQUES

2.1 Molecular beam epitaxy growth

For high-performance optoelectronic devices multilayer structures are required. The multilayer structures are achieved by growing single-crystal layers on substrates, the process commonly termed as epitaxy. There are two types of epitaxy, namely, homoepitaxy and heteroepitaxy. In homoepitaxy epilayer is grown on same substrate whereas in heteroepitaxy epilayer is grown on different substrate. Currently, different epitaxial growth methods can be classified as liquid phase epitaxy, vapor phase epitaxy, and molecular beam epitaxy/metal-organic chemical vapor deposition. In particular, molecular beam epitaxy provides several advantages such as high-purity, high-quality layers with abrupt interfaces, good control of thickness, composition, and doping, very reproducible uniformity across the substrate.

The InAsSbBi alloys are grown by molecular beam epitaxy[5] (MBE), an ultrahigh vacuum growth technique illustrated schematically in Figure 7. This is a suitable choice for growth of bismide alloys because it permits growth of non-equilibrium compositions. This is crucial for incorporation of Bi, which has very low equilibrium solid solubility in InAs.[16] Constituent atoms travel ballistically from the high-purity material cells to the surface of the substrate as a consequence of their long mean free path in ultrahigh vacuum ($< 10^{-9}$ torr), allowing atomically sharp and distinct interfaces to be grown. Valved group-V cells (As, Sb, Bi) with micrometer-scale adjustment allow precise control over V/III flux

ratios, which strongly influences Bi incorporation. Reflection high energy electron diffraction (RHEED) provides real-time feedback on the two-dimensional surface reconstruction of the growing sample which in turn indicates whether the surface is rich in group-V or group-III elements. Substrate growth temperatures may be varied over a wide range from approximately 0 °C to 750 °C or higher. An Ircon Modline 3 (model 3G-10C05) optical pyrometer is used to measure the substrate temperature and provide ± 1 °C control over the growth temperature. Growth of bismide alloys, which are highly dependent on growth temperature and constituent V/III flux ratios, makes full use of MBE growth's unique capabilities.

The MBE chamber used is a VG V80H solid source molecular beam epitaxy system. It is capable of growing on 2" or 3" diameter wafers. Special holders permit growth on ¼ wafer slices from 2" wafers. The samples examined in this work are grown at 15 nm/min, which is typical for the growth of many III-V materials. The As/III and Sb/III fluxes are calibrated prior to each growth by growing III-As and III-Sb on their respective III-V native substrates and slowly lowering the V/III flux ratio until the transition from a group-V to a group-III rich surface reconstruction is observed.[5] This procedure accurately and repeatably calibrates the one-to-one V/III flux ratios for As and Sb, with resulting V/III flux ratio accuracy of ± 1%.

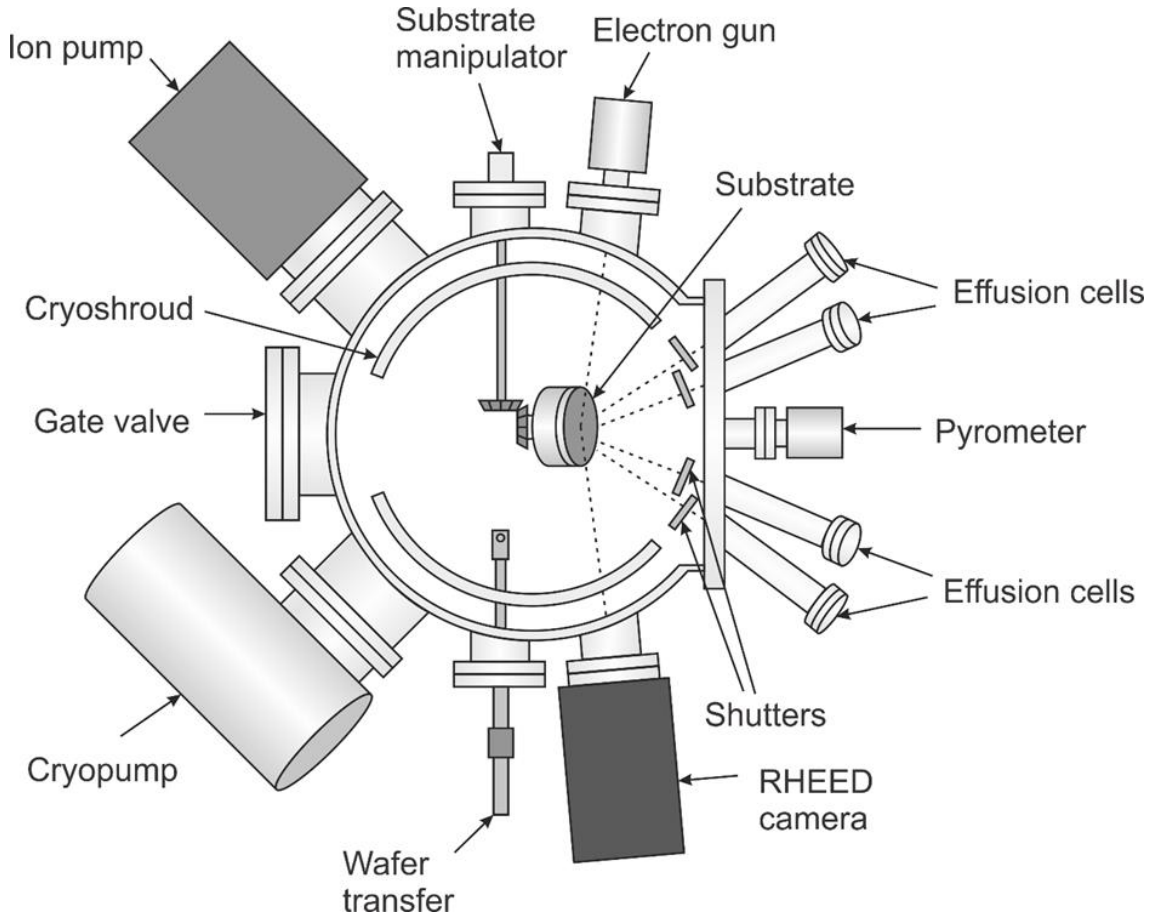

Figure 7: Schematic of molecular beam epitaxy (MBE) growth chamber, with key features highlighted.

2.2 Random Rutherford backscattering

Bohr's model depicts atoms as composed of a positively charged nucleus surrounded by negatively charged electrons bound to the nucleus by electrostatic forces. The existence of the nucleus was established by scattering experiments in which small portions high-energy alpha particles fired at a target were found to backscatter at very large angles.[17] These particles are backscattered due to collisions with the atomic nucleus, a phenomenon which forms the basis of Rutherford backscattering spectrometry.

Rutherford back-scattering is an analytical technique used to obtain multi-element depth concentration profiles that is fast, highly precise, and highly sensitive.[18] In Rutherford back-scattering measurements the surface of the sample is exposed to beam of alpha particles light particles that are accelerated to energies in MeV range in a vacuum chamber. Elastic collisions of these accelerated particles with heavy atoms in the target takes place that results in Coulomb scattering in a central force field. This scattering can be explained by classical mechanics. Because of these collisions there is a loss in kinetic energy of the particles, which are eventually stopped at a sufficient penetration depth in the target. The energy of the backscattered ions can be measured to give information on sample composition as a function of depth.[18]

The incident ion beam is aligned several degrees off-axis to high symmetry crystal directions so that collisions between the ions and atoms in the crystal appear random. This is to ensure that maximum atoms are examined to a depth of few microns. In contrast, aligning the ion beam with a high symmetry crystal direction results in ion channeling, in which the ions are guided into the lattice through coulomb collisions between ions and the channel walls. Ion channeling measurements are capable of probing much deeper into the sample and detecting the presence of interstitial impurities.

Energy is lost by an accelerated particle of mass m_{He} during large angle scattering by a stationary target particle of mass m_{target} as show in Figure 8. The particle kinetic energies before (E_0) and after (E_1) collision are related by Equation 2.1, shown below.[18]

$$\frac{E_1}{E_0} = \left[\frac{(m_{target}^2 - m_{He}^2 \sin^2\theta)^{\frac{1}{2}} + m_{He}\cos\theta}{m_{target} + m_{He}}\right]^2 \qquad (2.1)$$

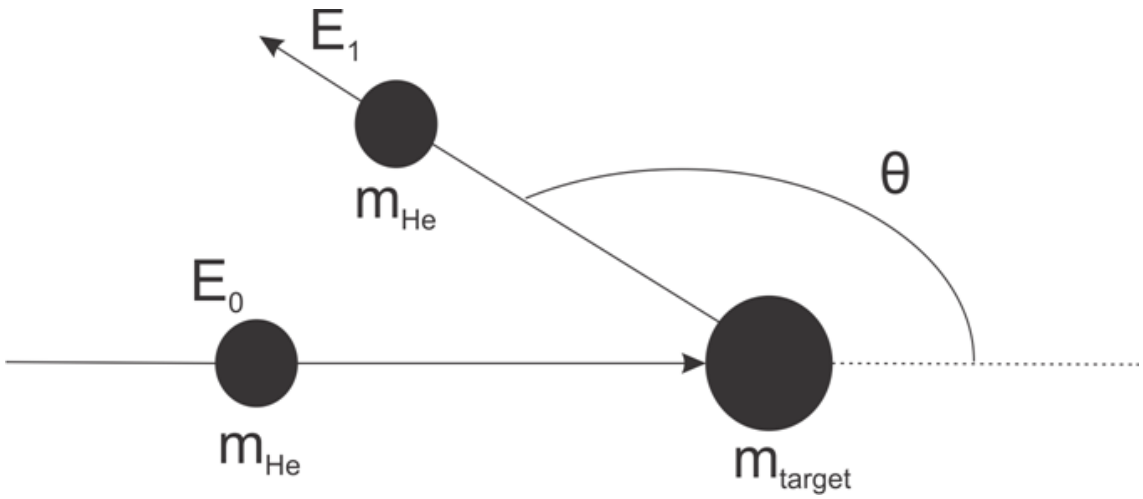

Figure 8: Schematic illustrating incident alpha particle backscattered at an angle θ after interaction with target particle. Kinetic energies of the alpha particle before and after the interaction are E_0 and E_1. The masses of the alpha particles and target atom are m_{He} and m_{target}, respectively.

This ratio of kinetic energies of the incident particle is sensitive to the target atomic mass when the backscattering angle is 180° making RBS useful in detecting specific atomic species when multiple atomic species are present in the sample. However, due to practical limitations including detector size, a backscattering angle of 170° is generally used.[18]

Random Rutherford backscattering spectrometry is used to determine the Bi mole-fraction of the InAsSbBi layer in all samples shown in Table 1. There is a characteristic energy peak in the backscattered ion yield from Bi, since it is the heaviest of all elements present in the sample, thus allowing the Bi mole fraction to be measured to a high degree of accuracy. Sensitivity analysis indicates that this technique is sensitive to Bi mole fraction differences as low as 0.1%.

All the random RBS measurements are carried out using 1.7 MV General Ionex Tandetron accelerator with 2 MeV doubly ionized He atoms and measured using a passivated implanted planar silicon detector. Samples are mounted on a two-axis goniometer that enables polar and azimuthal rotations and in a vacuum chamber at a pressure of 10^{-6} Torr. Ion beam is incident on the sample 8° from the normal and sample is rocked about the normal through an angular range of 5° at a rate of about one round cycle every two hours.

Initially RBS modeling was performed to simulate the backscattered ion yield of proposed cross section of the bulk quaternary InAsSbBi using a simulation software package called RUMP.[19] Representative simulated backscattering ion yields for the nominal InAsSbBi sample cross section are shown in Figure 9.

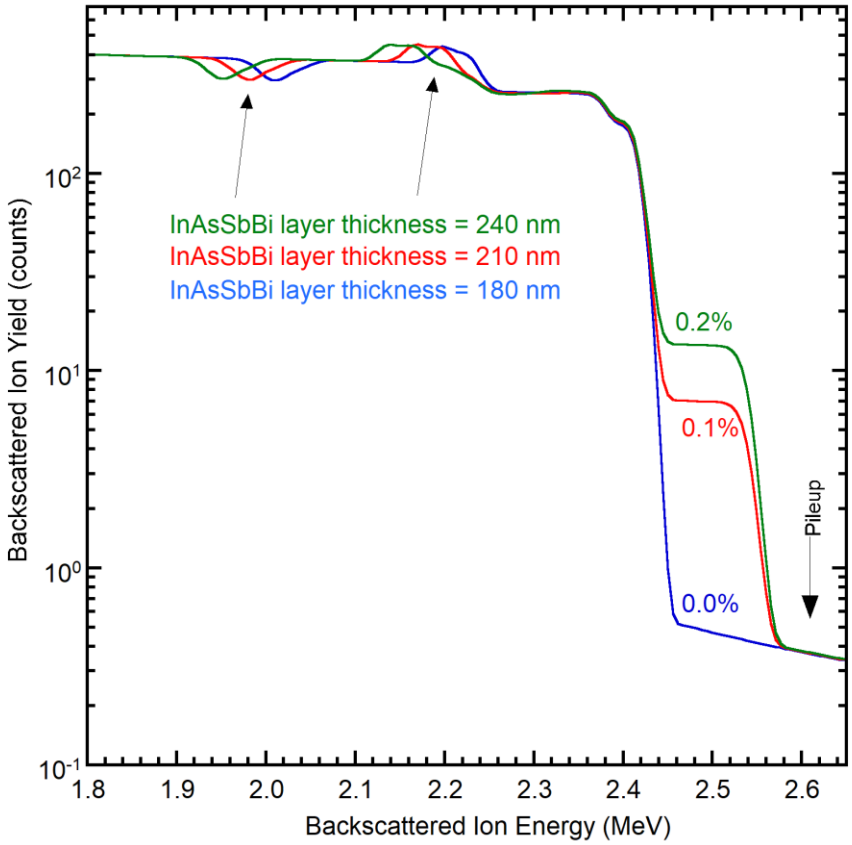

Figure 9: Simulated backscattering ion yield from bulk InAsSbBi on GaSb as a function of Bi mole fraction and InAsSbBi layer thickness. Increase in the Bi mole-fraction increases the height of Bi signal. Increase (decrease) in the InAsSbBi layer thickness the peak and valley features move left (right).

Similarly, for each sample Bi mole fraction is determined by fitting the height of this Bi signal, which increases proportionally to Bi mole fraction. The thickness of InAsSbBi layer is determined by horizontal positions of the peak and valley features between 1.92 MeV and 2.26 MeV. These features move to left (right) as the InAsSbBi layer thickness increases (decreases) as shown in Figure 9.

2.3 X-ray diffraction

X-ray diffraction (XRD) is a commonly used technique for structural characterization of epitaxial films. This technique provides rapid feedback for sample growth and does not require extensive sample preparation. Structural information such as layer thickness, in-plane strain, and lattice constant can be determined. Subsequently, using Bi mole fractions obtained from RBS and strain values obtained from XRD, and simple application of Vegard's law[41,62] the composition of quaternary bismide alloys can be determined.

Generally, crystals exhibit long-range order or translational periodicity. Hence, diffraction from the crystals can be studied using X-rays as the wavelength is on the order of the interatomic distance. Diffraction is a result of scattering of radiation by periodic arrangement of atoms in a crystal. At certain angles this scattering results in a constructive interference to give Bragg diffraction peaks which contain information about the arrangement of atomic planes. In a heterostructure, all the layers and substrate produce Bragg diffraction peaks. In addition, interactions between diffracted waves provide additional information about the microstructure. During the measurements, a fixed X-ray wavelength λ is used and incident angle θ is varied. The interatomic plane separation d_{hkl},wavelength λ used and incident angle θ are related by Bragg's law[20] which forms the basis for X-ray diffraction; n is order of reflection.

$$n\,\lambda = 2d_{hkl}\sin\theta \tag{2.2}$$

In real space Bragg's law interpretation is based on path difference between X-rays scattered from crystal planes with spacing, d_{hkl} as shown in Figure 10. When this path

difference is an integral multiple of wavelength, λ, there will be constructive interference and diffracted intensity will be maximum. This condition is depicted in Equation 2.2 above.

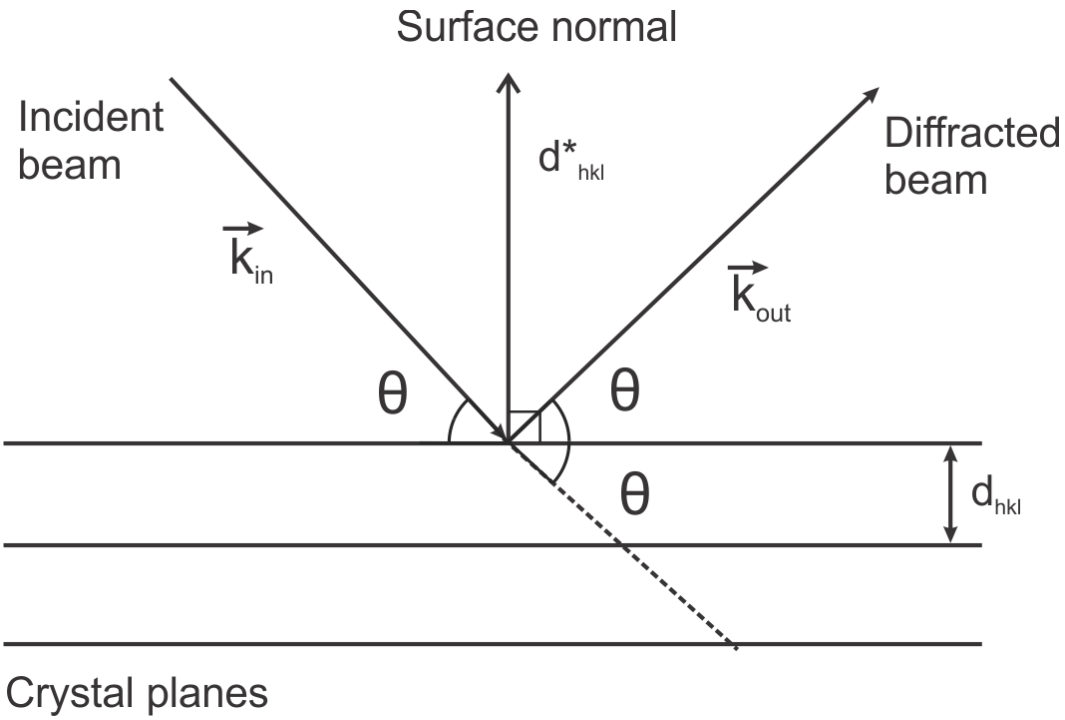

Figure 10. Illustration in real space the condition for Bragg reflection. Incident beam is inclined θ with respect to crystal planes; diffracted beam is at 2θ with respect to the incident beam. Incident beam, plane normal, and diffracted beam are all coplanar.

In reciprocal space Bragg's law interpretation, incident beam is represented as a wave vector, $\overrightarrow{k_{in}}$ with length $\frac{1}{\lambda}$ and the diffracted beam is represented as a wave vector, $\overrightarrow{k_{out}}$ with length $\frac{1}{\lambda}$ as shown in Figure 11. These wave vectors together define a scattering vector, $\vec{q}$ where $\vec{q} = \overrightarrow{k_{in}} - \overrightarrow{k_{out}}$. The angle between incident and diffracted wave vectors is 2θ and hence the length of scattering vector is $2\sin\theta\,|\overrightarrow{k_{out}}|$. Bragg scattering occurs when the

scattering vector$\vec{q}$ is exactly equivalent to reciprocal lattice vector d^*_{hkl} which is normal to the planes hkl and has length $\frac{1}{d_{hkl}}$. This is the Laue condition and is exactly equivalent to the Bragg condition in real space. Finally, on substitution and rearrangement in the $\vec{q} = 2 \sin\theta \, |\overrightarrow{k_{out}}|$ the condition depicted in Equation 2.2 above is achieved.

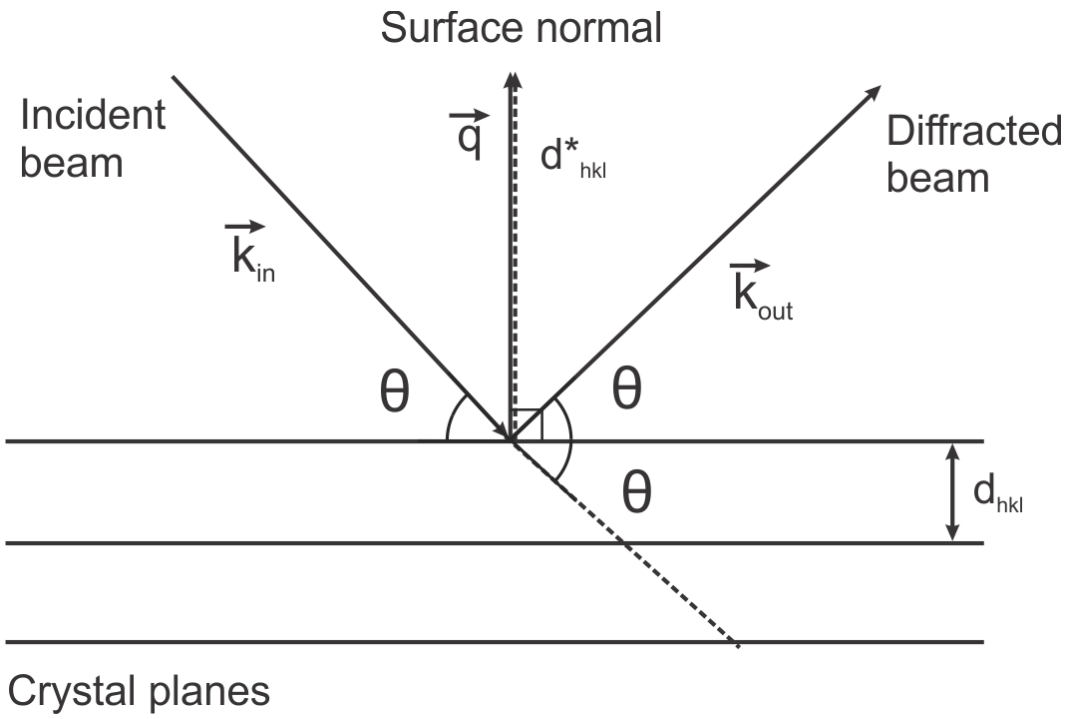

Figure 11. Illustration in reciprocal space the condition for Bragg reflection. Incident beam wave vector is inclined θ with respect to crystal planes; diffracted beam wave vector is at 2θ with respect to the incident beam. Scattering wave vector $\vec{q}$ and reciprocal lattice vector d^*_{hkl} are shown.

The intensities of Bragg reflection are predicted from kinematic or dynamical calculations. It is not possible to get intensity from all the reflections because some reflections are absent as the lattice structure give rise to destructive interference while some reflections give rise negligible intensity because the atomic arrangement give rise to nearly

complete destructive interference. Further, some reflections are not accessible because to create the appropriate scattering vector, either the incident or diffracted beam should be below the sample surface. In wafer samples this is not a possibility as the incident or diffracted beam would be totally absorbed by the sample. Considering the above factors, all the scans and maps in this work are obtained using the (400) and (511) reflections.

A scan is series of steps in which intensity is measured for a change in scattering vector $\vec{q}$. Both change in the incident wave vector or diffracted wave vector result in a change in scattering vector. Omega/2theta scans are most commonly used measurements, in this scan the sample rotation angle $\Delta\omega$ and detector rotation angle $\Delta 2\theta$ are coupled such that $\Delta 2\theta = 2 \times \Delta\omega$ and hence, also known as coupled scans. The difference between the two values θ and ω is called the offset. A reciprocal space map is obtained by collecting omega/2theta scans over a range of offset values.

All the high-resolution X-ray diffraction patterns are measured using a PANalytical X'Pert Pro materials Research X-ray diffractometer with instrumental resolution of ~12 arcsec and Cu $K\alpha_1$ radiation with wavelength of 1.54060 Å. The incident beam optics consist of an X-ray mirror, a 2-crystal Ge (220) 4-bounce monochromator, and a 0.25° divergence slit which control the equatorial divergence of the incident beam. The diffracted beam optics consist of a triple axis monochromator, and a 0.50° receiving slit which improves the resolution. The receiving slit is placed before the detector. All the simulations are carried out using PANalytical X'Pert Epitaxy,[21] a dynamical diffraction modeling program. The diffraction parameters for Bi and InBi are manually added to the software material database.[22,23] The reciprocal space maps from samples are constructed

from approximately fifty ω-2θ triple-axis scans for ω -offsets spaced 3.3 arcsec apart around the (400) reflection and 7.2 arcsec apart around (511) reflection.

2.4 Transmission electron microscopy

Transmission electron microscopy (TEM) is a technique which provides crystallographic and compositional information through diffraction, high resolution imaging, and spectroscopy.[24] Electrons are emitted from a field emission gun and accelerated at high voltages in the range of 100 to 300 kV. Subsequently, these electrons are manipulated to form a parallel beam by a series of gun and condenser lenses present in the microscope column. Finally, this beam is focused on a thin sample which is usually <100 nm. The incident beam of electrons interacts with core and valence electrons and nuclei in the sample giving rise to scattering. Depending on the energy loss after interaction these scattering events are divided into two categories: elastic scattering with no energy loss and inelastic scattering with quantifiable energy loss. Elastically scattered electrons are used for diffraction and imaging in transmission electron microscopy mode,[25,26] and scanning transmission electron microscopy mode.[27] Inelastically scattered electrons are used for spectroscopic studies in energy dispersive X-ray, and electron energy loss spectroscopy techniques.[28] The two modes of imaging, conventional and scanning modes are used to study InAsSbBi samples in this work.

In conventional TEM imaging, depending on size of objective aperture there is amplitude or phase contrast in the final image. Amplitude contrast is further divided into

mass thickness or diffraction contrast. Incoherent elastic scattered electrons give rise to mass thickness contrast and coherent elastic scattering give rise to diffraction contrast. Amplitude contrast is dominant in bright field and dark field imaging wherein a small objective aperture is used. In bright field (dark field) imaging a small objective aperture is placed around the transmitted (diffracted) beam to collect electrons that form the final image. One variant of DF imaging, 200 (objective aperture around 200 reflection) dark field diffraction contrast imaging of zinc blende structured alloys,[25] is a chemically sensitive technique where the structure factor reflects differences in atomic scattering of the constituent elements.

Phase contrast is dominant in high resolution TEM[26] wherein a large objective aperture is used. Coherent elastic scattered electrons are collected to form a high-resolution image. When the sample is thin, and electron absorption is negligible the weak phase object approximation holds, changes in phases of scattered waves occurs. These interfere with the transmitted wave to produce intensity in the final image.[29,30]

Scanning TEM is in principle similar to scanning electron microscopy[31] but uses transmitted electrons for imaging.[27] Depending on the angle of scattering of electrons there is combined mass-thickness and diffraction contrast or only mass thickness contrast in the final image. Different types of detector arrangements such as bright field, medium angle annular dark field, and high angle annular dark field with collection semi-angles 0-22 mrad, 20-60 mrad, and 90-170 mrad respectively are used to detect imaging electrons scattered to different angles. In particular, high angle annular dark field image shows mass thickness contrast primarily dependent on average atomic number of sample and its thickness. For

this reason, this is also known as Z contrast imaging. Z-contrast imaging particularly useful in detecting contrast from heavier atomic number atoms such as Bi.

Transmission electron microscopy requires extensive sample preparation in order to achieve electron transparent condition. All samples are prepared in orthogonal [011] and $[01\bar{1}]$ projections. Initially thin slices that are less than 3 mm in length are cut from the wafers using a diamond wafer saw. The slices are glued together with epoxy so that layer sides are sandwiched between two (100) GaSb substrates. The glued stack is polished on allied multiprep polisher using diamond lapping film on one side with decreasing abrasive diamond grain sizes in the order 9.0, 6.0, 3.0, 1.0, and 0.1 μm without a wedge angle. Next the stack is flipped to perform a final polish by using a wedge angle 1° on the opposite side to reach a wedge thickness of 1-2 μm. Next, the polished sample is glued to a Cu TEM slot grid and Ar+ ion milled while rotating and cooling using liquid nitrogen.

In this work, 200 dark-field and high-resolution TEM imaging are carried out using a Philips CM 200 high-resolution electron microscope which is operated at an acceleration voltage of 200 kV, equipped with objective apertures, and has an interpretable resolution of 2.5 Å. Scanning TEM imaging is carried out using a JEOL ARM 200F which is operated at an accelerated voltage of 200 kV and has a resolution of 0.8 Å and equipped with aberration correctors as shown in the Figure 12.

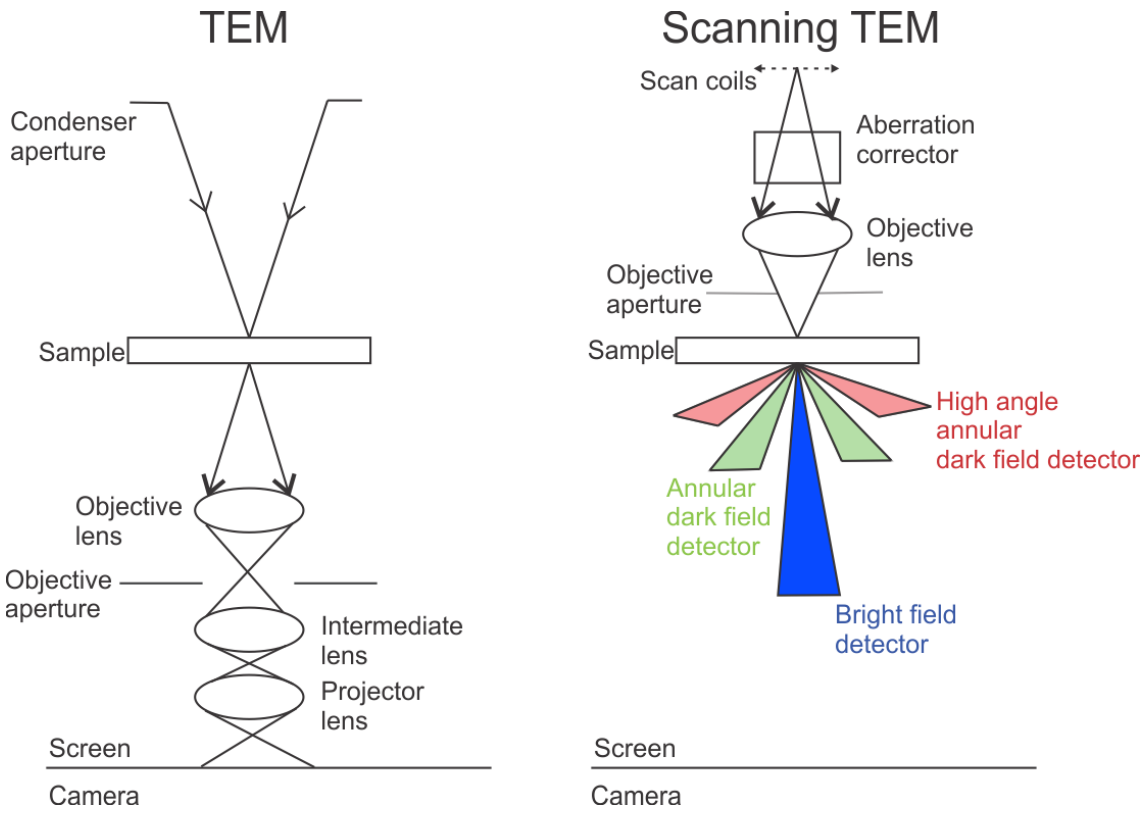

Figure 12: Schematic illustrating transmission electron microscopy (left) and scanning transmission electron microscopy (right). Electrons pass through various apertures and lens systems before interacting with the sample. The final image is formed on the screen below. In scanning mode there are extra scan coils to raster the electron beam across the sample, an aberration corrector, and detectors for electrons scattered to different angles after interaction with sample.

2.5 Nomarski optical microscopy

Nomarski optical microscopy or differential interference contrast microscopy is a straightforward technique used to image the surface of bulk InAsSbBi samples.[40] In this microscopic observation technique, a very small height difference on the surface of the sample, which is not visible with bright field, becomes a 'three-dimensional' image with improved contrast. In this microscopy, contrast arises from the refractive index gradients

of different areas of a sample. This technique uses a combination of polarizer, Nomarski prism, and analyzer along with other optical components. In this technique, light is passed through a polarizer which is reflected by a half-silvered mirror. Next the Nomarski prism separates this polarized light into two perpendicularly polarized light rays. These two rays are reflected at the sample surface and are recombined as they pass through the prism again. Finally, the analyzer selects a component from each of the two interfering rays to produce the differential interference contrast image. Any roughness or height differences on the surface results in a phase difference between the two waves. This phase shift is converted to differential interference contrast. An Olympus MX50 optical microscope with Nomarski prism, analyzer, and polarizer components as shown in Figure 13 is used to carry out differential interference contrast microscopy.[32]

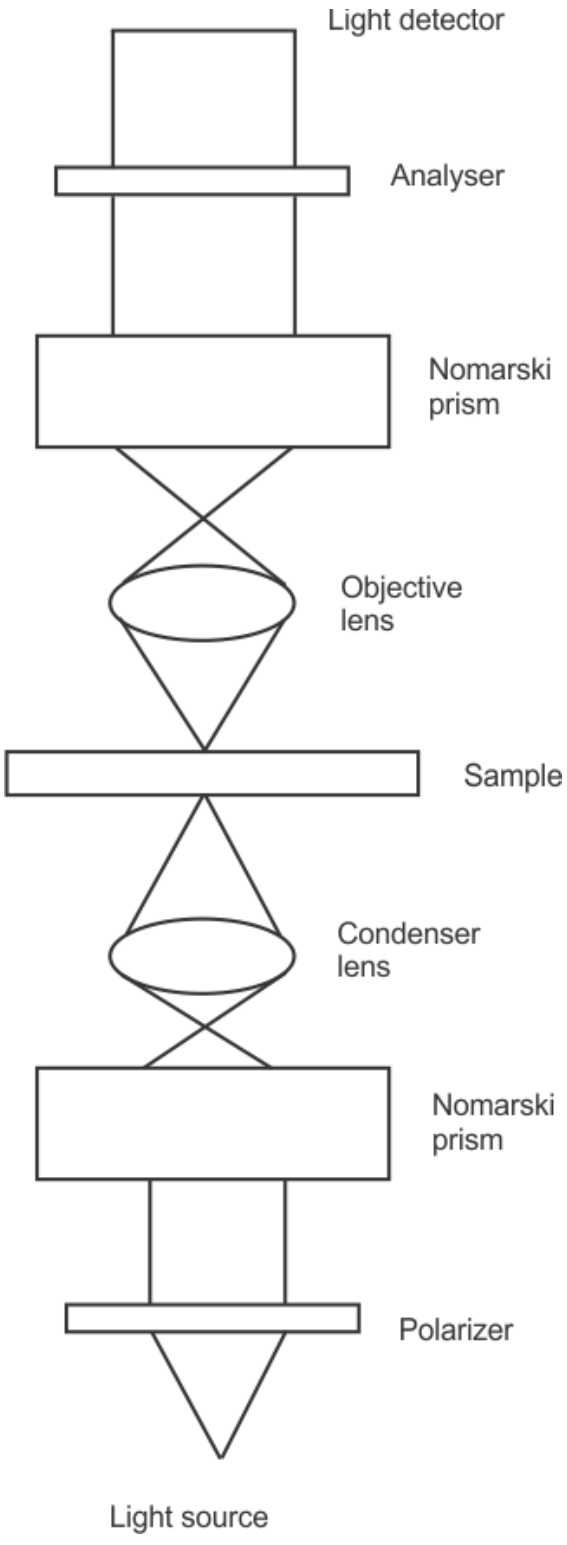

Figure 13: Schematic illustrating Nomarski optical microscopy. Light pass through polarizer, Nomarski prisms, lens, and analyzer finally to the detector.

2.6 Atomic force microscopy

Atomic force microscopy is used to examine surface morphology of grown samples. Atomic force microscopy or scanning force microscopy is technique based on van-der-Waals and electrostatic forces between a probe tip and surface of the samples. This technique uses a sharp probe mounted to a cantilever that scans across the surface of samples.[33] There are three modes of atomic force microscopy: contact mode, non-contact mode and tapping mode. In this work, tapping mode is used to characterize the InAsSbBi sample surfaces because of advantages like higher lateral resolution, minor forces, and negligible probe/sample damage. In this mode, an oscillating probe tip taps the surface to map the topography. The cantilever oscillation frequency is measured using a reflected laser beam from cantilever onto a photo diode. The probe-surface interactions are used to measure the amplitude of surface height variations and display the result as an image on computer screen. Schematic illustrating tapping mode in atomic force microscope and its basic components are shown in Figure 14. The probe tip is attached to an oscillating cantilever which scans over the sample surface. A split photodiode detector, which is a position sensitive detector, detects the deflection of laser. A feedback loop maintains the constant oscillating amplitude. All AFM measurements are carried out in air using a Brucker multimode 8 with a lateral scan range of 100 microns and vertical scan range of 5.5 microns.

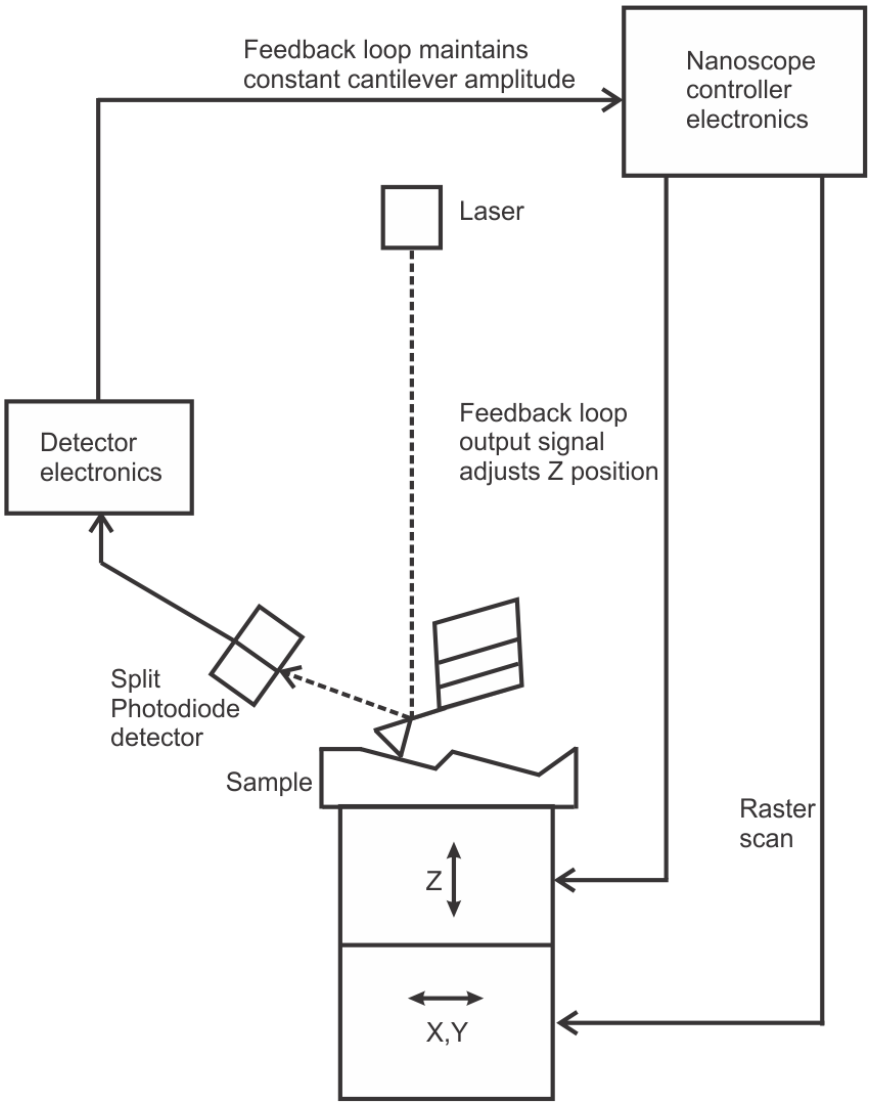

Figure 14: Schematic illustrating tapping mode in AFM and its basic components. The probe tip is attached to an oscillating cantilever which scans over the sample surface. A split photodiode detector, which is a position sensitive detector, detects the deflection of laser. A feedback loop maintains the constant oscillating amplitude.

2.7 Photoluminescence spectroscopy

Photoluminescence spectroscopy is used to study the electronic properties of semiconductor materials such as the band gap, position, and density of defect levels. In

this technique, the samples are excited by a focused laser beam with photon energy larger than the band gap. The photons interacting with the electrons in the valance band and excite them into the conduction band generating the carriers. These charge carriers then recombine and emit a photon which with approximately the energy of the band gap. Depending on the energy range this technique can be used to detect the band edge PL signal, defect levels within the band gap that act as non-radiative recombination centers. Bulk InAsSbBi samples were optically characterized by photoluminescence spectroscopy[5] (PL). Samples were mounted in a closed-loop He-refrigerated cryostat, enabling measurement at cryogenic temperatures as low as 12 K. Samples were optically pumped by a 785 nm laser diode at up to 120 W/cm^2 incident intensity. Infrared photoluminescence was collected by a Nicolet Magna-IR 760 Fourier Transform infrared spectrometer (FTIR) utilizing a liquid-nitrogen-cooled InSb detector (cutoff wavelength of ~5.5 µm). The pump laser is modulated at 50 kHz and the detector signal is fed through a phase-locked loop amplifier for improved signal-to-noise ratio. System throughput correction is achieved by measuring the spectrum of a Mikron M305 black body source at 800 °C and comparing the measurement with the theoretical black-body curve. Measurements were performed using two detector types. To cover the full infrared wavelength range, a HgCdTe detector with a cut-off of approximately 15.5 µm and a InSb detector with cut-off of 5.4 µm were used.

3. IMPACT OF GROWTH TEMPERATURE AND *As/In* FLUX ON STRUCTURAL PROPERTIES OF *InAsSbBi* LAYERS

The physical and chemical properties of 210 nm thick InAsSbBi layers grown by molecular beam epitaxy at temperatures between 400 and 430 °C on (100) GaSb substrates are investigated using Rutherford back scattering, X-ray diffraction, transmission electron microscopy, Nomarski optical microscopy, and atomic force microscopy.[34] The results indicate that the layers are nearly lattice matched, coherently strained, and contain dilute Bi mole fractions. Large surface droplets with diameters on the order of 1 μm and densities on the order of 10^6 cm^{-2} are observed when the InAsSbBi growth is performed with lean As overpressures around 1%. Surface droplets are not observed when the As overpressure is increased to 4%. Small crystalline droplets with diameters on the order of 70 nm and densities on the order of 10^{10} cm^{-2} are observed between the large droplets for InAsSbBi grown at 430°C. Analysis of one of the small droplets indicates a misoriented zinc blende crystal structure composed primarily of In, Sb, and Bi, with a lattice constant of 6.543 ± 0.038 Å. Lateral modulation in the Bi mole fraction is observed in InAsSbBi layers grown at 400 °C.

3.1 Samples studied

This work examines four $InAs_{1-x-y}Sb_yBi_x$ samples A, B, C, and D grown by solid-source molecular beam epitaxy[5] at a rate of 15 nm/min on GaSb (100) oriented substrates. The

sample cross-section is shown in Figure 5. The InAsSbBi layers are grown at temperatures from 400 to 430 °C, using V/In flux ratios 0.120 for Sb/In, 0.050 and 0.100 for Bi/In, and 0.911 and 0.940 for As/In. The temperatures and V/In flux ratios used during growth, and the in-plane biaxial strain of the InAsSbBi bulk layers are provided for each sample in Table 2. Droplets are observed on the two samples grown with the smallest As flux.

Table 2. InAsSbBi sample name, growth temperature, V/In flux ratios, in-plane bi-axial strain, and if Bi rich droplets are present on the surface.

Sample	Growth temperature	V/In flux ratios			Strain (%)	Surface droplets
		Bi/In	Sb/In	As/In		
A	430 °C	0.100	0.120	0.911	-0.142	Yes
B	420 °C	0.050	0.120	0.940	-0.080	No
C	400 °C	0.050	0.120	0.940	-0.061	No
D	400 °C	0.050	0.120	0.911	-0.111	Yes

All growths are performed at a constant In flux of 4.4×10^{14} $cm^{-2}s^{-1}$ corresponding to an InAsSbBi on GaSb growth rate of about 15 nm/min. The As/In and Sb/In fluxes are calibrated prior to each growth by growing InAs on InAs and InSb on InSb and slowly lowering the V/In flux ratio until the transition from a group-V to a group-III rich surface reconstruction is observed using reflection high energy electron diffraction. This procedure accurately and repeatably calibrates the one-to-one group-V to In flux ratios for As and Sb, from which existing ion gauge measurements of the As and Sb fluxes as a function of valve position are employed to set the flux with a precision better than 1%. The Bi flux is calibrated using scanning electron microscope measurements of the thickness of

190 nm of elemental Bi deposited on GaAs at 100 °C. The substrate temperature is measured using an Ircon Modline 3 (model 3G-10C05) pyrometer.

All growths are performed under group-V rich surface reconstructions where all of the incident In flux incorporates at these growth temperatures. The individual group-V fluxes are set in terms of excess elemental overpressure, defined as the difference between the incident flux for a given element (specified by the V/In flux ratio for that element) and the fraction of the incident flux incorporated (specified by the elemental mole fraction). In particular the As overpressure, set at either 1 or 4% for the InAsSbBi growths examined here, is found to strongly influence Bi incorporation and surface morphology.

3.2 Strain and Composition

The RBS measurements and simulations of the InAsSbBi samples are shown in Figure 15. The experimental measurements are shown as solid blue curve. The simulated profile shown as the red solid curve is the sum of simulated ion yields for each element shown as solid curves. Although the In, As, Sb, and Bi signals arise from the same InAsSbBi layer, the backscattered ion yield for these increasingly heavier elements occur at progressively larger backscattered ion energies. As the element with the largest atomic mass, Bi yields a high energy shoulder from 1.765 to 1.858 MeV in the backscattering spectrum that is typically sensitive to small 0.1% variations in the Bi mole fraction of bulk layers.[22] Nevertheless, the analysis overestimates the Bi mole fraction in InAsSbBi samples that have Bi-rich surface features, due to a large backscattering signal from the surface. This

is evident from the backscattered ion yield in Figure 15a (sample A), where the elemental Bi signal is not what is expected from a uniform bulk layer. The fact that the Bi signal exhibits a non-uniform peak at the highest energies indicates the presence of Bi-rich regions near and at the sample surface. This particular Bi signal is reproduced in the simulation by using a model with multiple Bi containing layers that comprises 160 nm of $InAs_{0.919}Sb_{0.055}Bi_{0.026}$, 50 nm of $InAs_{0.923}Sb_{0.039}Bi_{0.038}$, 10 nm of $AlSb_{0.955}Bi_{0.045}$, and 10 nm of $InAs_{0.950}Bi_{0.050}$. This indicates approximately 5% Bi coverage on or near the sample surface that is a consequence of the accumulation of unincorporated Bi on the growth surface that does not evaporate with the other group-V elements As and Sb. The simulated Bi mole fractions are 0.1% and 0.4% for samples B and C that do not have Bi-rich surfaces and 2.6% and 1.1% for samples A and D that have Bi-rich surfaces (see Figure 15).

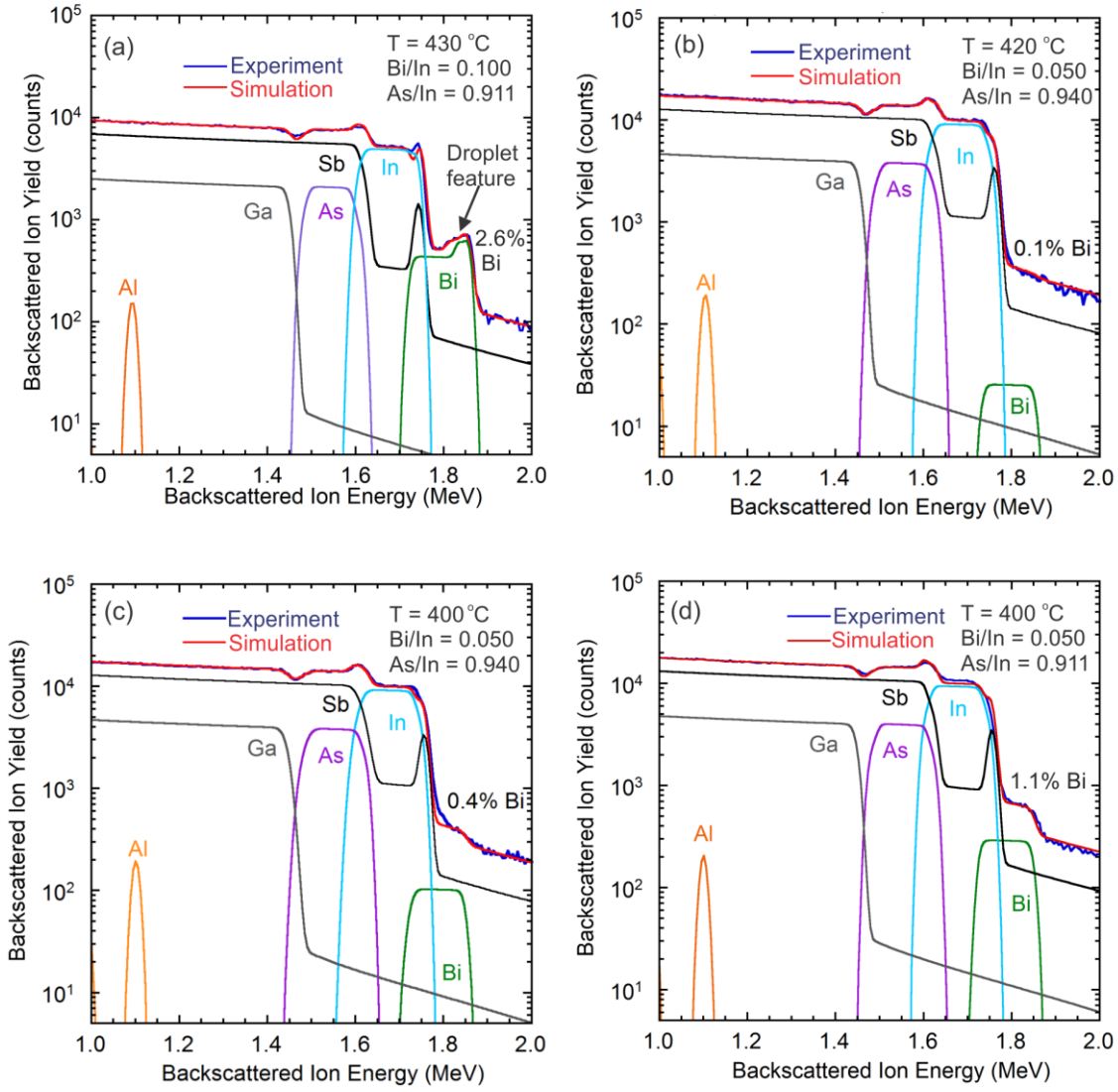

Figure 15: Random Rutherford backscattering ion yield as a function of backscattered ion energy from bulk InAsSbBi (samples A through D), labeled (a) through (d) respectively. The blue curve is the experimentally measured ion yield and the red curve is the aggregate simulated yield obtained from the sum of the individual simulated ion yields shown for each element. The growth temperature and Bi/In and As/In flux ratios are shown for each sample; the Sb/In flux ratio is constant at 0.120 for all samples.

Measurements and simulations of (400) ω-2θ coupled XRD scans from the four samples are shown in Figure 16. The measured diffraction patterns are given by the solid

black curves and the simulations by the solid red curves. The InAsSbBi layers are coherently strained with in-plane compressive-strains from -0.061% to -0.142%. The lattice mismatch is sufficiently small that the critical thicknesses (240 to 630 nm) exceed that of the 210 nm thick InAsSbBi layers grown. The simulated epilayer thickness are 180 nm (A), 210 nm (B), 210 nm (C), and 194 nm (D). A lower than expected intensity for the InAsSbBi layer peak and Pendellösung fringes in samples A and D indicates diminished interface quality, due to the presence of Bi-rich surface features that permeate InAsSbBi layer and barriers. Broadening of the InAsSbBi layer peak in samples C and D indicates fluctuations in the material composition within the layer. In addition to the compressively strained InAsSbBi layer peak, a tensile peak is observed near the GaSb substrate peak that is due to the unintentional incorporation of As in the GaSb buffer. The dilute As mole fractions range from 0.17% to 0.48% and are insufficient to induce relaxation in the 500 nm buffer as the critical thicknesses are greater than 1.2 μm for all samples. The unintentional As originates from the As background pressure in the growth chamber.

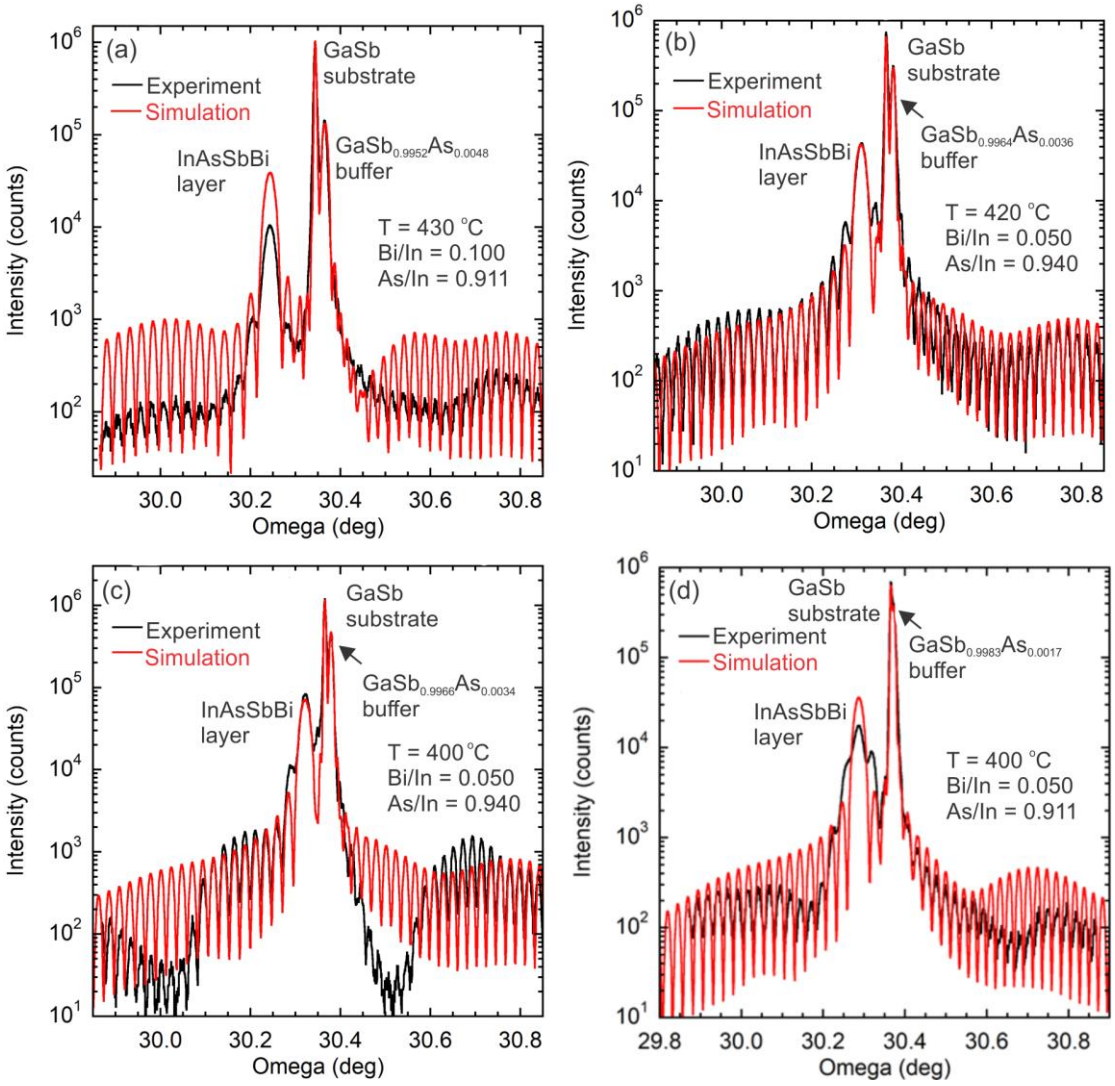

Figure 16: Coupled ω-2θ X-ray diffraction scans from the (400) plane (black curves) and simulations (red curves) for bulk InAsSbBi, (samples A through D), shown in (a) through (d) respectively. The compressively strained InAsSbBi peak is located on the left and provides a measure of tetragonal distortion and subsequent in-plane biaxial strain of the layer. The tensile peak is a result of unintentional incorporation of As in the GaSb buffer that comes from the As background pressure in the growth chamber. The growth temperature and Bi/In and As/In flux ratios are shown for each sample and the Sb/In flux ratio is held constant at 0.120 for all samples.

The XRD analysis provides the in-plane strain values reported in Table 3. The Bi and Sb mole fractions of strained InAsSbBi are linearly related in the analysis,[5,35] a result of

the linear relationship between the constituent binary lattice constants assumed in Vegard's Law. In the limit with no Bi, the in-plane strain establishes maximum Sb and minimum As mole fraction limits for the InAsSbBi layers, which are reported in the XRD section of Table 3. The RBS analysis has a limited sensitivity to the Sb mole fraction because the Sb signal overlaps the much larger In signal from the InAsSbBi layer. Likewise, the As signal overlaps the much larger Sb signal from the GaSb buffer layer. When fit independently, the RBS simulated Sb mole fractions exceed the maximum possible mole fraction given by XRD by about 0.01 for the droplet free samples and by about 0.2 for the droplet covered samples. Therefore, the Sb and As mole fractions used in the RBS simulations are the limits provided by XRD.

The Bi mole fraction, x, provided by the RBS simulations in Figure 15 is reported in the RBS section of Table 3. The Sb mole fraction, y, given by its relationship to Bi mole fraction and layer strain is reported in the RBS+XRD section of Table 3 for the droplet free samples B and C. For completeness the As mole fractions are reported as $1 - x - y$. Since the RBS measurements of the droplet covered samples do not provide the Bi mole fraction of the InAsSbBi layer, it is not possible determine the Sb mole fraction for samples A and D using RBS and XRD. The mole fractions obtained directly from TEM dark field images of the InAsSbBi layers are reported in the TEM+XRD section of Table 3. The results are provided in the next section.

Table 3. InAsSbBi group-V mole fractions (%) determined from XRD, RBS, RBS+XRD, and TEM+XRD.

Sample	XRD		RBS	RBS+XRD		TEM+XRD		
	Sb	As	Bi	Sb	As	Bi	Sb	As
A	≤ 10.9	≥ 89.1	2.6			0.1	10.8	89.1
B	≤ 10.1	≥ 89.9	0.1	10.0	89.9	0.4	9.6	90.0
C	≤ 9.8	≥ 90.2	0.4	9.3	90.3	0.5	9.1	90.4
D	≤ 10.5	≥ 89.5	1.1			0.8	9.5	89.7

3.3 Lateral composition modulation

The composition distribution of the InAsSbBi layers is examined using cross-sectional TEM, 200 dark-field imaging, high-angle annular-dark-field imaging, and scanning TEM energy-dispersive X-ray spectroscopy. Low magnification bright-field TEM micrographs from the four InAsSbBi samples are presented in Figure 17. These results show the overall microstructure of the bulk material and indicate that the 210-nm-thick InAsSbBi layers are pseudomorphic with no visible defects over large lateral distances. Furthermore, contrast modulation due to inhomogeneous composition[34,36] is observed in samples B, C, and D shown in Figures 17b, 17c, and 17d respectively. As the growth temperature decreases, the Bi mole fraction increases, and the lateral composition modulation becomes more pronounced.

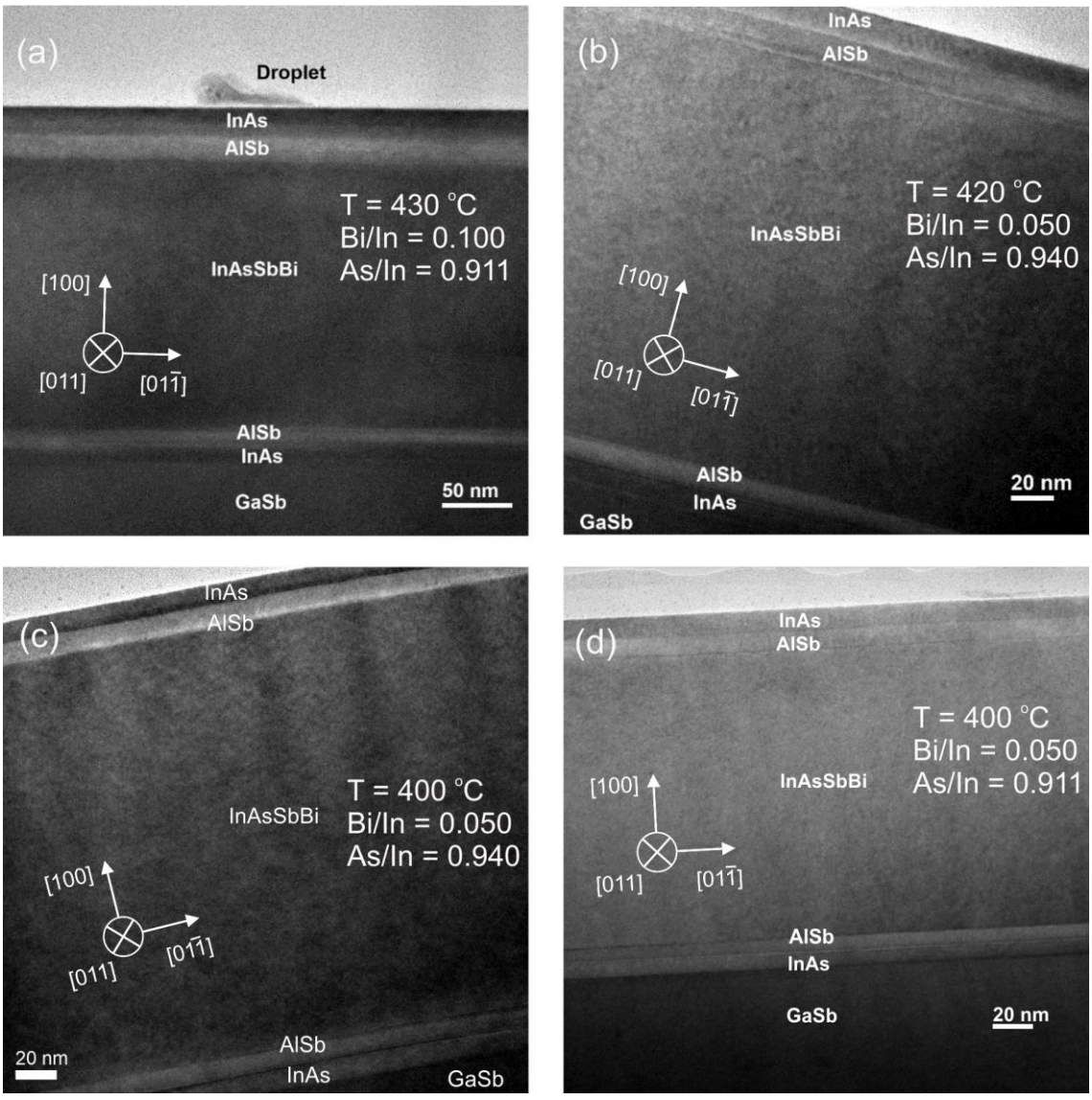

Figure 17: Bright field cross-section TEM images in the [011] projection showing the overall microstructure of InAsSbBi (samples A through D), in (a) through (d) respectively. A surface droplet consisting of mostly InSbBi is visible in (a). Contrast modulations perpendicular to the growth plane in (b), (c), and (d) show composition inhomogeneity with a modulation period of approximately 30 nm. The growth temperature and Bi/In and As/In flux ratios are shown for each sample; the Sb/In flux ratio is constant at 0.120 for all the samples.

A contrast-enhanced TEM cross-sectional image of sample C is shown in Figure 18 and illustrates that columns of heavy element-rich (dark regions) and heavy element-

deficient (light regions) form spontaneously with a period of approximately 30 nm as the growth progresses from the bottom to the top of the image.

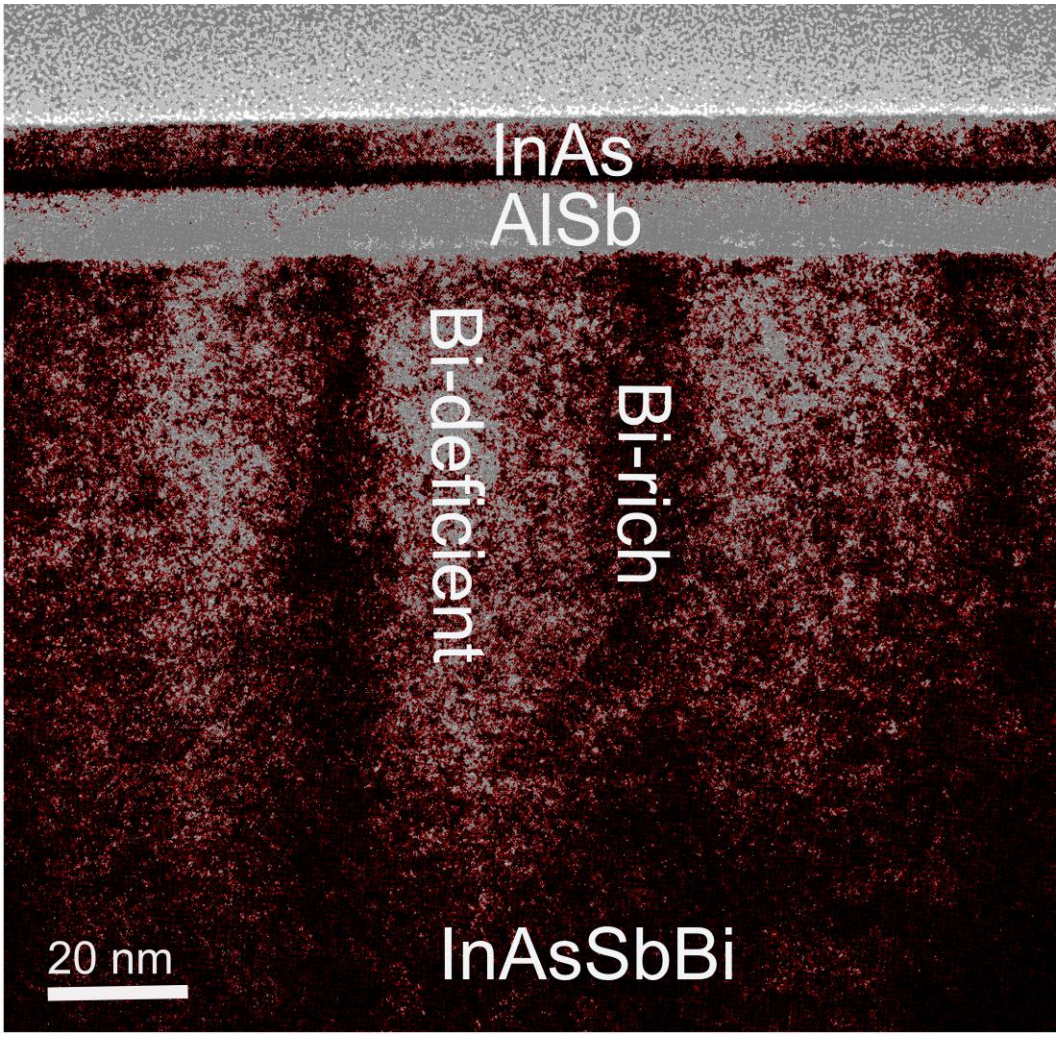

Figure 18: Contrast-enhanced TEM cross-sectional image of InAsSbBi (sample C) showing lateral composition modulation. Columns of heavy element-rich (dark regions) and heavy element-deficient (light regions) form spontaneously as growth proceeds from the bottom to top of the image. These heavy element-rich columns are periodic at roughly 30 nm.

The 200 dark-field imaging is a chemically sensitive technique in zinc blende alloys that provides local chemical information and has been employed to study composition modulation in InAs/AlAs and InAs/InAsSb superlattices,[37] GaAsBi,[9] and GaSbBi[12] alloys. The contrast arises primarily from difference in atomic scattering factors between the group-III and group-V constituent elements and qualitatively reflects the content of different atomic constituents in the alloy.[38] Dark-field TEM micrographs from samples C and D are shown in Figure 19, where intensity line profiles across the areas marked shows lateral quasi-periodic composition modulations with a period of approximately 30 nm. The contrast is chemically sensitive to the elemental content of the layer imaged in these micrographs. The bright areas likely correspond to Bi-rich regions and the dark areas correspond to Bi-deficient regions similar to that observed in GaAsBi[10] and InAsBi.[14] These features are consistent with the broadening of the InAsSbBi peak in the XRD patterns shown in Figures 16c and 16d and the low magnification transmission electron micrographs shown in Figures 17c and 17d.

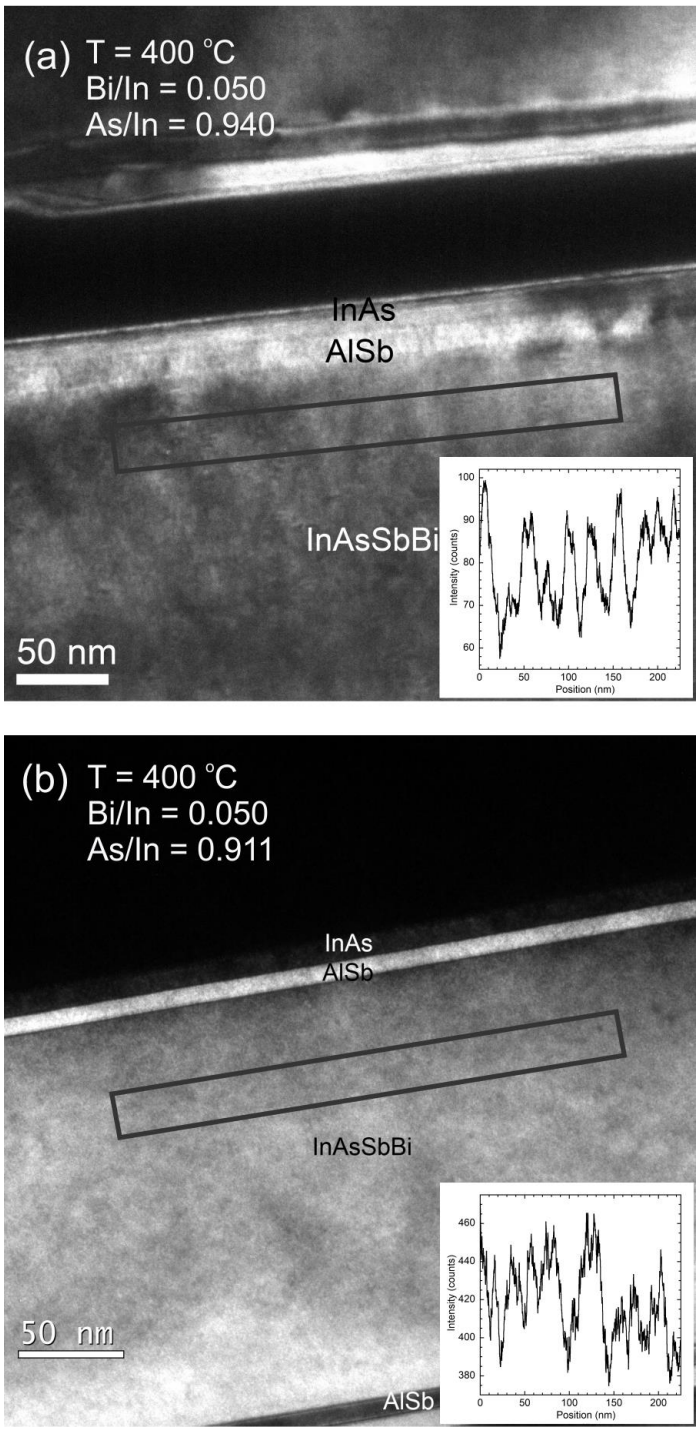

Figure 19: Chemically sensitive 200-dark field images from InAsSbBi (samples C and D) grown at 400 °C, shown in (a) and (b) respectively. Line scans of the image intensity from the regions marked by the rectangles parallel to the layer interface are shown in the insets.

The Bi mole fraction is estimated from the (200) dark field images using a method proposed by Bithell and Stobbs.[38] This method of composition analysis is applicable to the InAsSbBi samples as the atomic scattering factors of each element differ significantly, the material is not highly strained, and specimen thickness is much less than the 1.7 μm extinction distance. The samples have a thickness of approximately 80 nm and a biaxial strain that is less than 0.15%. The diffraction pattern satisfies the Bragg condition and is absent of double diffraction. The samples imaged at an under-focus condition where spherical aberrations are minimal and contrast reversals are not present.

In this method, according to kinematical approximation, the intensity of the dark field reflection, $I_{200,InAsSbBi}$, is proportional to the square of the specimen thickness d and the square of the structure factor for the (200) reflection that satisfies the selection rule $h + k + l = 4n + 2$. This relation is expressed in terms of the atomic scattering factors[39] and atomic mole fractions as

$$I_{200,InAsSbBi} \propto d^2[f_{In} - (1 - x - y)f_{As} - yf_{Sb} - xf_{Bi}]^2 . \quad (3.1)$$

Thus, by considering the ratio of intensity scattered by InAsSbBi into the 200 reflection to that scattered by AlSb at same specimen thickness, the constant of proportionality and the specimen thickness are eliminated, and the ratio of the intensities is given as

$$\frac{I_{200,InAsSbBi}}{I_{200,AlSb}} = \frac{[f_{In} - (1 - x - y)f_{As} - yf_{Sb} - xf_{Bi}]^2}{[f_{Al} - f_{Sb}]^2} . \quad (3.2)$$

Using this relationship, the Bi mole fraction is expressed in terms of the scattering factors, the Sb mole fraction, and the ratio of the intensities, with

$$x = \frac{f_{As} - f_{In} + (f_{Sb} - f_{As})y + (f_{Al} - f_{Sb})\sqrt{\frac{I_{200,InAsSbBi}}{I_{200,AlSb}}}}{f_{As} - f_{Bi}}. \quad (3.3)$$

The atomic scattering factors f_{Al}, f_{In}, f_{As}, f_{Sb}, and f_{Bi} for Al, In, As, Sb, and Bi used in the analysis are provided in Table 4. These scattering factors are determined from Doyle and Turner[39] by linearly interpolating their tabulated values to the relevant scattering angle parameter $s = 1/a^{\perp}_{InAsSbBi}$, where $a^{\perp}_{InAsSbBi}$ is the out-of-plane lattice constant of the InAsSbBi layer.

The Sb mole fraction $y(x, a_{InAsSbBi})$ is a function of the Bi mole fraction x and the unstrained InAsSbBi lattice constant $a_{InAsSbBi}$ provided by the XRD analysis. The lattice constant of the coherently strained InAsSbBi layer is distorted in the growth direction and matched to the substrate lattice in the growth plane and is given as[40]

$$a_{InAsSbBi} = \left[\left(\frac{1 - \nu_{InAsSbBi}}{1 + \nu_{InAsSbBi}}\right)\varepsilon_{\perp} + 1\right] a_{GaSb}\,. \quad (3.4)$$

Where $\varepsilon_{\perp}$ is the tetragonal distortion of the unit cell, a_{GaSb} is the GaSb substrate lattice constant, and $\nu_{InAsSbBi}$ is Poisson's ratio that is estimated using a linear interpolation of the binary values ν_{InAs} = 0.3521,[6] ν_{InSb} = 0.3530,[6] and ν_{InBi} = 0.3503.[22] For the InAsSbBi compositions examined, its value varies by less than 1 part in 1000 from 0.35213 to 0.35219 and is assumed to be constant with $\nu_{InAsSbBi}$ = 0.3522. This simplifies the relation in Equation 3.4 as a given tetragonal distortion corresponds to a unique lattice constant, regardless of the mole fraction distribution. The out-of-plane lattice constant[40] is $a^{\perp}_{InAsSbBi} = [\varepsilon_{\perp} + 1]a_{GaSb}$ and the in-plane lattice constant is $a^{\parallel}_{InAsSbBi} = a_{GaSb}$.

Assuming Vegard's law,[41,62] the $InAs_{1-x-y}Sb_yBi_x$ lattice constant is given as a linear combination of the known binary lattice constants a_{InAs} = 6.0583 Å, a_{InSb} = 6.4794 Å, and

a_{InBi} = 6.611 Å for InAs,[6] InSb,[6] and InBi.[22] From Vegard's law the Sb mole fraction in terms of the InAsSbBi lattice constant and the Bi mole fraction is

$$y(x, a_{InAsSbBi}) = \frac{a_{InAsSbBi} - a_{InAs}}{a_{InSb} - a_{InAs}} - x\frac{a_{InBi} - a_{InAs}}{a_{InSb} - a_{InAs}}. \quad (3.5)$$

This relationship provides a family of Sb and Bi mole fractions for a given InAsSbBi lattice constant with $dy/dx = (a_{InBi} - a_{InAs})/(a_{InSb} - a_{InAs})$ = 1.3120. The in-plane biaxial strain is defined as $\varepsilon_{xx} = \varepsilon_{yy} = a_{GaSb}/a_{InAsSbBi} - 1$ and is reported in Table 2. The resulting out-of-plane uniaxial strain is $\varepsilon_{zz} = a^{\perp}_{InAsSbBi}/a_{InAsSbBi} - 1 = -\varepsilon_{xx}2\nu_{InAsSbBi}/(1 - \nu_{InAsSbBi})$, and the tetragonal distortion in terms of the in-plane and out-of-plane strains is $\varepsilon_{\perp} = (\varepsilon_{zz} - \varepsilon_{xx})/(1 + \varepsilon_{xx})$.

Table 4. InAsSbBi unstrained lattice constant $a_{InAsSbBi}$, out-of-plane strained lattice constant $a^{\perp}_{InAsSbBi}$, scattering angle parameter s, and atomic scattering factors for Al, In, As, Sb, and Bi.

Sample	$a_{InAsSbBi}$ (Å)	$a^{\perp}_{InAsSbBi}$ (Å)	s (Å^{-1})	f_{Al} (Å)	f_{In} (Å)	f_{As} (Å)	f_{Sb} (Å)	f_{Bi} (Å)
A	6.1046	6.1140	0.16356	2.903	6.479	4.530	7.013	8.772
B	6.1008	6.1061	0.16377	2.900	6.473	4.526	7.007	8.765
C	6.0996	6.1036	0.16384	2.899	6.472	4.525	7.005	8.763
D	6.1027	6.1101	0.16366	2.901	6.476	4.528	7.010	8.768

The subsequent lateral profiles in the Bi mole fraction are shown in Figure 20 for all samples. The values shown are averages over the approximately 80 nm thick specimen cross-section. The lateral Bi mole fraction varies from 0.13 to 0.16% with an average of 0.14% in sample A, from 0.35 to 0.38% with an average of 0.36% in sample B, from 0.43 to 0.58% with an average of 0.52% in sample C, and from 0.73 to 0.83% with an average

of 0.78% in sample D. In comparison, the RBS measurements specify an average Bi value of 0.1% for sample B and 0.4% for sample C that have little or no excess Bi on a smooth surface, and 2.6% for sample A and 1.1% for sample D that have excess Bi on a droplet covered surface. The Sb mole fractions specified by the dark field and XRD measurements are 10.80%, 9.61%, 9.13%, and 9.52%, for samples A through D respectively.

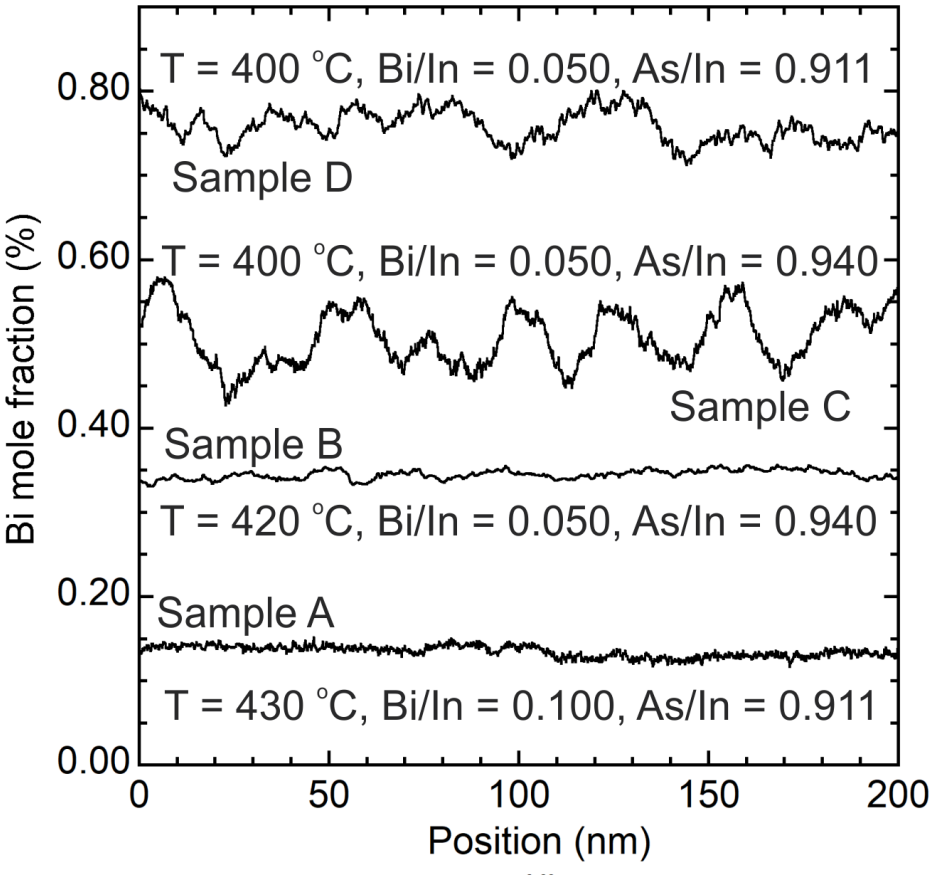

Figure 20: Lateral Bi mole fraction profiles obtained from chemically sensitive 200-dark field images of InAsSbBi (samples A through D), with the significant growth conditions shown for each.

High angle annular dark field scanning transmission electron micrographs from samples C and D are shown in Figures 21a and 21b respectively. These images, commonly

referred to as Z-contrast images,[27] provide mass thickness contrast that is primarily dependent on atomic number, and are particularly well suited for detecting heavier elements such as Bi, and confirming the presence of lateral composition modulation. Energy dispersive X-ray spectrum (EDX) maps from samples C and D are shown in Figure 21 to the right of the Z-contrast images. These images provide spatial maps of the elemental distribution of In, As, and Sb, where the signal for each corresponds to the L electron shell transition with energies at 3.29 keV, 1.29 keV, and 3.60 keV, respectively. These maps show that these elements are essentially homogeneous in the lateral direction. The decrease in signal observed from the lower to upper AlSb markers is due to a decrease in sample thickness. The X-ray signal from the comparatively dilute Bi mole fractions is insufficient to map. The EDX analysis indicates that the observed lateral composition modulation is not due to variations in the In, As, or Sb mole fractions.

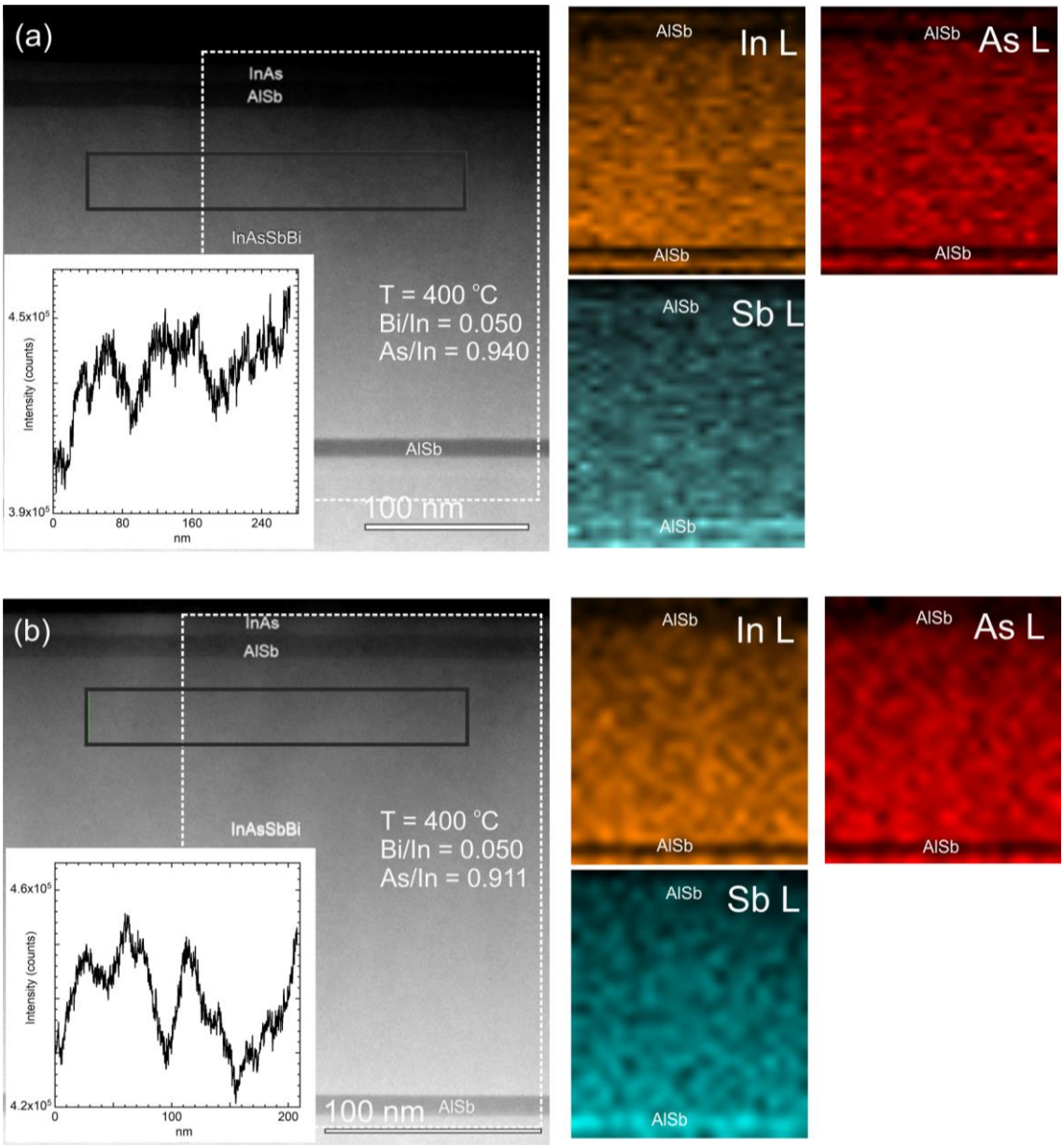

Figure 21: High angle annular dark field scanning transmission micrographs from InAsSbBi (samples C and D) are shown in (a) and (b) respectively. Line scans of the image intensity parallel to the layer interface in the black rectangles are shown as insets. Scanning TEM energy dispersive x-ray maps of the spatial distribution of elemental In (orange), As (red), and Sb (cyan) from the regions marked by white dotted rectangles are shown to the left.

The Bi-rich columns originate during the early stages of bulk layer growth and become more pronounced as growth proceeds. The diffusivity of Bi plays a role in the formation of these Bi-rich columns, therefore kinetic factors such as growth temperature influence the development of these features. The composition modulation period is approximately the same in the samples although the layer strain varies (see Table 2), indicating that strain plays little to no role in development of these nanocolumns.[11] Similar Bi-rich nanostructures have been reported for GaAsBi bulk layers[9] and quantum wells.[42] The phase separation and surface segregation of Bi likely occurs because of a preferential attraction of Bi atoms towards Bi rich areas.

3.4 Surface morphology

Nomarski optical microscopy images of the surface of InAsSbBi samples A through D, labeled (a) through (d), are shown in Figure 22. The images are 200 µm wide by 150 µm high and the significant growth conditions are shown for each. Figures 22b and 22c show that samples B and C are optically smooth. While sample A (Figure 22a) exhibits droplet features with 1.5 µm diameters and 3×10^6 cm^{-2} densities and sample D (Figure 22d) exhibits droplet features with 3 µm diameters and 0.5×10^6 cm^{-2} densities.

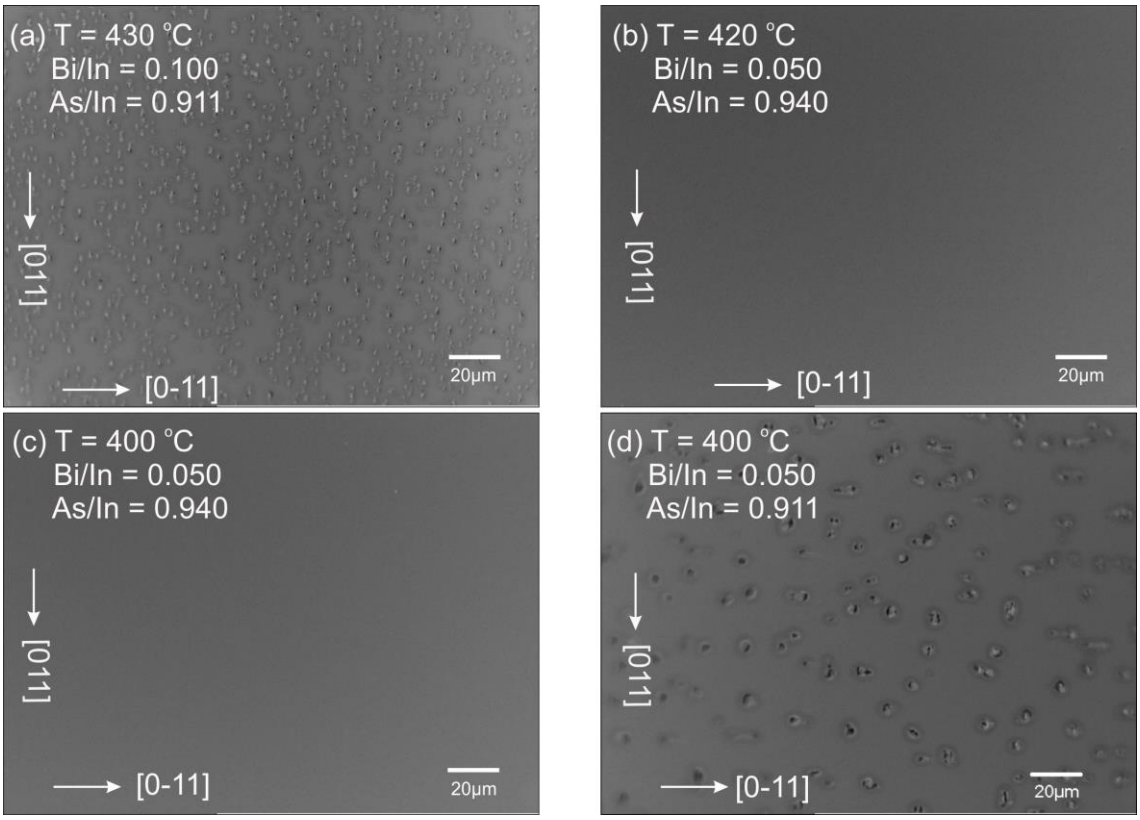

Figure 22: Nomarski optical measurements of surface morphology of bulk InAsSbBi (samples A through D), shown in (a) through (d) respectively. Image dimensions are 200 μm by 150 μm. The growth temperature and Bi/In and As/In flux ratios are shown for each sample; the Sb/In flux ratio is constant at 0.120 for all samples.

Atomic force microscopy images of the surface morphology of the InAsSbBi samples A through D, labeled (a) through (d), are shown in Figure 23. The images are 100 μm by 100 μm on the left with a zoomed in 5 μm by 5 μm measurement on the right. The root mean square (RMS) roughness over the entire area imaged is shown for each and summarized in Table 5. The optically smooth samples B and C are remarkably flat on the 5 μm length scale with a RMS roughness less than 1 nm. The droplet-covered samples A and D are rough on 100 μm length scale with droplets over 100 nm high and a RMS roughness around 40 nm. When zoomed in between the large droplet features of sample

D it is observed to be relatively smooth on the 5 μm length scale with a RMS roughness less than 1 nm. While a second set of much smaller and higher density droplets is observed between the large droplets on sample A. The droplets are isotropic, indicating the absence of a preferential direction in diffusion of the Bi atoms.

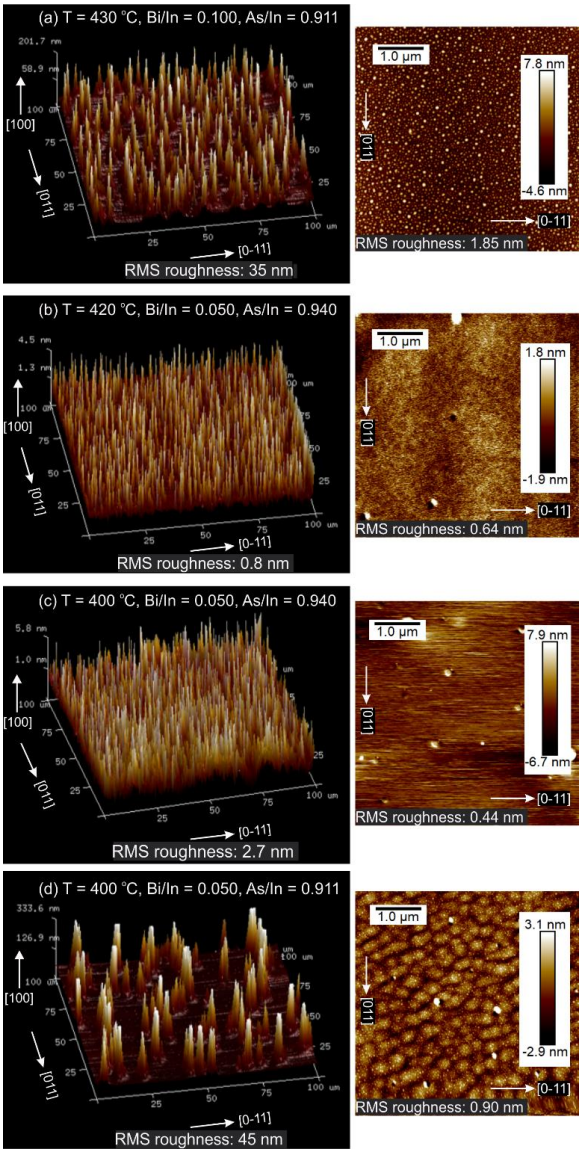

Figure 23: Atomic force microscopy images of surface morphology of bulk InAsSbBi (samples A through D), shown in (a) through (d) respectively. Images dimensions are 100 μm by 100 μm on the left and 5 μm by 5 μm on the right. RMS roughness measurements at $(100\ \mu m)^2$ scale range from 0.8 to 45 nm and at $(5\ \mu m)^2$ from 0.44 nm to 1.85 nm. The

growth temperature and Bi/In and As/In flux ratios are shown for each sample; the Sb/In flux ratio is constant at 0.120 for all samples.

Table 5. Root mean square (RMS) surface roughness of samples A through D from AFM measurements over surface areas of 100 µm by 100 µm, 5 µm by 5 µm, and 1 µm by 1 µm. The significant growth conditions are provided for each InAsSbBi layer.

Sample	Growth temperature	Flux ratios			RMS roughness (nm)		
		Bi/In	Sb/In	As/In	100 µm by100 µm	5 µm by 5 µm	1 µm by 1 µm
A	430 °C	0.100	0.120	0.911	35	1.85	1.80
B	420 °C	0.050	0.120	0.940	0.8	0.64	0.17
C	400 °C	0.050	0.120	0.940	2.7	0.44	0.38
D	400 °C	0.050	0.120	0.911	45	0.90	0.46

The droplet sizes and densities are summarized in Table 6. Samples A and D both have large droplet features and sample A has a second set of much higher density (2.3×10^{10} cm^{-2}) of much smaller droplets between the large droplets. The small droplet diameters range from 30 to 100 nm with an average of 70 nm. An estimation of the fraction of the surface covered by the droplets and the average droplet volume per unit area are reported in Table 6. The volume of each droplet set is roughly 5% of the InAsSbBi layer volume. Sample A grown with the largest Bi flux and at the highest temperature has the largest surface droplet coverage.

Table 6. Surface droplet density, diameter, height, fraction of surface area covered, and aggregate volume per unit area for samples A and D and the measurement method.

Sample	Sample A			Sample D	
Method	Nomarski	AFM		Nomarski	AFM
Droplet size	Large	Large	Small	Large	Large
Density (cm^{-2})	3.0×10^{6}	2.5×10^{6}	2.3×10^{10}	0.5×10^{6}	0.5×10^{6}
Diameter (μm)	1.5	1.5	0.07	3	3
Height (nm)		210	10		310
Coverage (%)		4	90		4
Volume/unit area (nm)		9	9		11

To aid the incorporation of Bi during the growth of InAsSbBi at these temperatures,[5] small excess As overpressures are used. Since the samples contain about 90% As, about 1% of the 0.911 incident As/In flux is not incorporated and desorbs from the surface of the droplet covered surfaces, and about 4% of a larger 0.940 incident As/In flux is not incorporated and desorbs from the smooth surfaces. This indicates that the Bi-As interaction on the surface plays an important role in the incorporation and desorption of Bi adatoms from the total group-V surface reservoir. Under a larger As flux, the Bi-Bi interaction and the surface diffusion of Bi may be suppressed, while the Bi-As interaction leads to enhanced Bi desorption. For the rough, feature covered, samples A and D, some of the excess Bi remains on the surface and segregates, diffuses, and coalesces to form macroscopic droplets. Since this does not occur in the optically smooth samples B and C, the excess Bi desorbs from these surfaces along with the other excess group-V elements.

3.5 Cross-sectional analysis of small droplet

The small droplet imaged in Figure 16a is further examined using high resolution transmission electron microscopy. The results are presented in Figure 23, with a high-resolution micrograph in (a), a fast Fourier transform (FFT) of the high-resolution atomic image of the droplet in (b) and the InAs cap in (c), and the EDX spectrum in (d). The droplet is crystalline and 75 nm wide by 20 nm high and the results indicate that the droplet has a misoriented zinc blende structure and is primarily composed of In, Sb, and Bi.

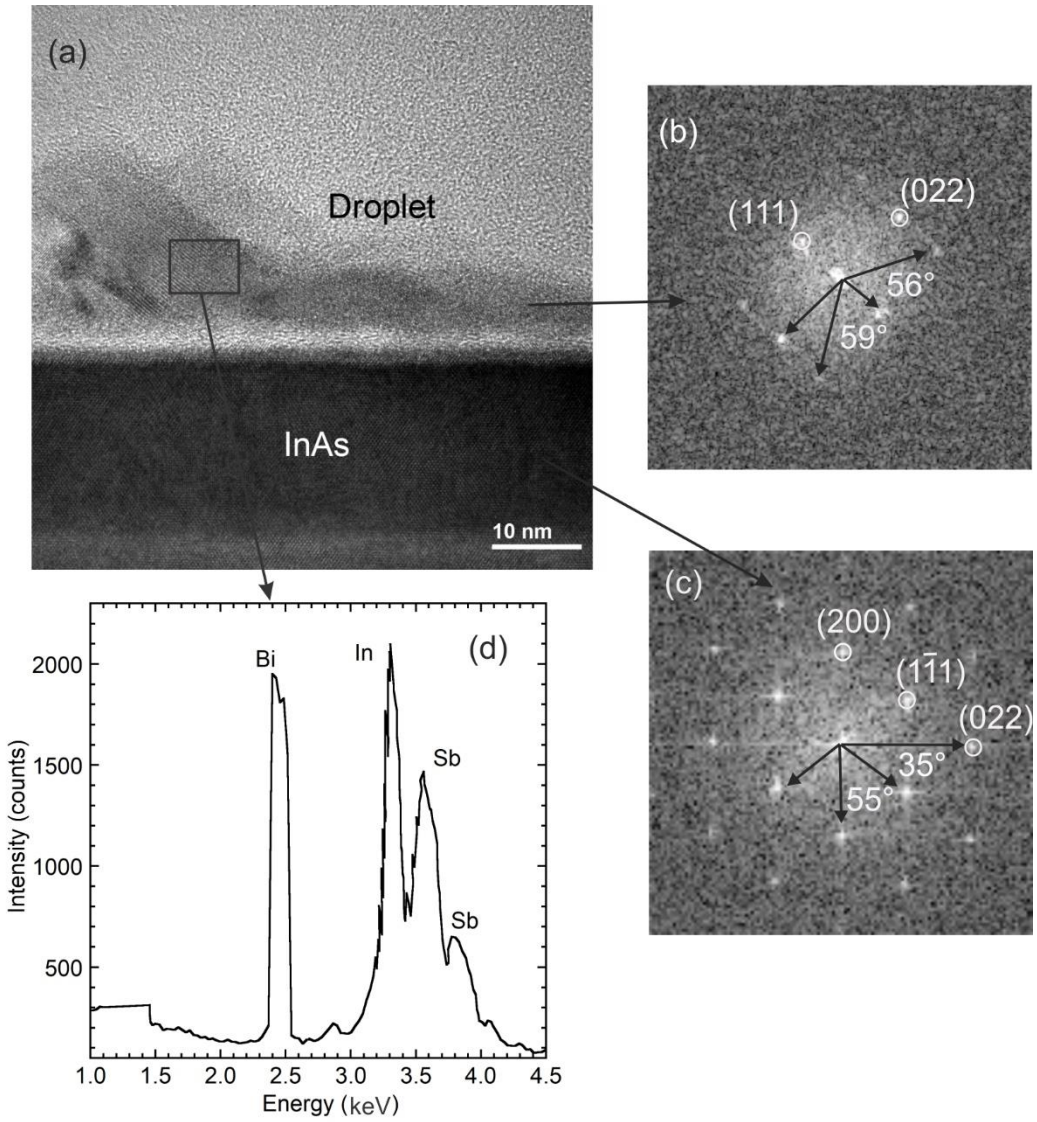

Figure 23: Cross-section high-resolution transmission electron micrograph of a surface droplet and InAs cap layer are shown in (a) for 430 °C grown InAsSbBi (sample A). Fast Fourier transforms (FFTs) with different diffraction spots and angles from both the imaged droplet and top InAs cap are shown in (b) and (c). The FFT from the InAs cap image indicates a zinc blende crystal structure and the FFT of the droplet image indicates a misoriented zinc blende crystal structure. The energy dispersive x-ray spectrum in (d) indicates the droplet is primarily composed of In, Sb and Bi.

The lattice constant, a, of the droplet feature is determined by the separation, r_{hkl}, between the FFT pattern spot (h, k, l) and the origin (0,0,0) with

$$a = \lambda L \left(\sqrt{h^2 + k^2 + l^2}\right) / r_{hkl} \ , \tag{3.6}$$

where λ is the wavelength of electron, L is the distance between the sample and the screen, and the camera constant λL is 121.2 Å, as determined using the indexed FFT from the InAs cap layer with known InAs lattice constant a_{InAs} = 6.0583. Nevertheless, the droplet lattice constant can be expressed in terms of the known InAs lattice constant as

$$a_{droplet} = a_{InAs} \frac{r_{hkl,InAs}\left(\sqrt{h^2 + k^2 + l^2}\right)_{droplet}}{r_{hkl,doplet}\left(\sqrt{h^2 + k^2 + l^2}\right)_{InAs}}. \tag{3.7}$$

The separations in units of pixels are $r_{022,InAs}$ = 40.02 ± 0.26 and $r_{111,InAs}$ = 24.47 ± 0.28 from Figure 23c and $r_{022,droplet}$ = 36.99 ± 0.14 and $r_{111,droplet}$ = 22.72 ± 0.21 from Figure 23b. From these values, the droplet lattice constant is found to be 6.553 ± 0.042 Å using the (022) spots and 6.525 ± 0.073 Å using the (111) spots for the analysis. The uncertainties provided for each value are reported as the standard deviation[43] in 10 separate measurements of separations in each diffraction spot set. Since each set of diffraction spots provides a slightly different value, the best estimate of the lattice constant is reported as a weighted mean and uncertainty of the two values, which is 6.543 ± 0.038 Å and lies between that of InSb and InBi. The weighting is inversely proportional to the standard deviation of each value and the uncertainty is reported as the standard deviation of the weighted mean.

Reports on the synthetization of other III-V Bi containing materials also indicate the formation of similar crystalline features attributed to difficulties in Bi incorporation. Including Bi-rich zinc blende Ga(As,Bi) clusters in GaAsBi after annealing,[44,45] InBi

clusters with a distorted PbO structure in InAsBi,[46] and Bi-rich surface droplets with distorted zinc blende structures with a 80° tilt in InAsBi.[14]

3.6 Chapter 3 Summary

The chemical and structural properties of InAsSbBi layers grown by molecular beam epitaxy on GaSb at 400, 420, and 430 °C are examined. The layers are 210 nm thick, coherently strained, with sharp interfaces, and contain dilute Bi mole fractions. Lateral modulation of the Bi mole fraction is observed in the InAsSbBi layers and is particularly pronounced in the two samples grown at the lowest 400 °C temperature where more Bi is incorporated. The two growths with As overpressures around 1% resulted in the formation of Bi-rich surface droplet features with diameters much larger than the InAsSbBi layer thickness and a volume per unit area of about 5% of the InAsSbBi layer. The two growths with As flux overpressures around 4% resulted in droplet-free surfaces, indicating that the presence of excess surface As plays a role in the desorption of excess Bi from the surface. The sample grown at the highest 430 °C temperature and the largest 0.10 Bi/In flux ratio also contains a much larger surface density of much smaller microscopic crystalline droplets with a misoriented zinc-blende crystal structure primarily composed of In, Sb, and Bi, and a lattice constant of 6.543 ± 0.038 Å that is between that of InSb and InBi.

4. IMPACT OF SUBSTRATE OFFCUT ON STRUCTURAL PROPERTIES OF *InAsSbBi* LAYERS

Three InAsSbBi samples are grown by molecular beam epitaxy at 400 ºC on GaSb substrates with three different orientations: sample D is (100) on-axis, sample E is (100) offcut 1° to (011), and sample F is (100) offcut 4° to (111)A. These samples are investigated using transmission electron microscopy, X-ray diffraction, atomic force microscopy, and Nomarski optical microscopy. Bismuth rich surface droplets are observed on all samples. The epilayers are 210 nm thick, coherently strained, and show no observable defects. Strain-induced crystallographic tilt is observed in the InAsSbBi layers grown on the (100) 1° to (011) and (100) 4° to (111)A offcut substrates. A mathematical model relating the tilt angle to the out of plane distortion and substrate offcut is developed. The Bi mole fraction is homogeneous throughout the layer for growth on the (100) offcut 1° to (011) substrate, while lateral composition modulation is observed for growth on the (100) on axis and (100) offcut 4° to (111)A substrates. InAsSbBi grown on (100) on-axis and (100) offcut 4° to (111)A substrates exhibits isotropic surface droplets, while InAsSbBi grown on the (100) offcut 1° to (011) substrate shows anisotropic surface droplets indicating preferential diffusion of Bi along the $[01\bar{1}]$ step edges.

4.1 Samples studied

This work examines $InAs_{1-x-y}Sb_yBi_x$ samples D, E, and F grown by solid-source molecular beam epitaxy on GaSb substrates with three orientations, (100) on axis, (100)

offcut 1° to (011), and (100) offcut 4° to (111)A respectively. The sample cross-section is shown in Figure. 5 and discussed in detail in Chapter 1. The InAsSbBi layers are grown at a temperature of 400 °C, using relative group-V to In flux ratios of 0.911 for As/In, 0.105 and 0.120 for Sb/In, and 0.050 for Bi/In. Of the incident Bi flux, about 15% incorporates substitutionally on the group-V sublattice, while about 53% desorbs with the excess As, and about 32% accumulates on the surface forming Bi rich droplets. The InAsSbBi layers and growth conditions are provided in Table 7.

Table 7. InAsSbBi sample name and substrate orientation, V/In flux ratios, average mole fractions, in-plane strain, and presence of surface droplet features. The growth temperature is 400 °C for all samples.

Sample	V/In flux ratios (%)			Mole fraction (%)			Strain(%)	Surface droplet
	Bi/In	Sb/In	As/In	Bi	Sb	As		
D, (100)	5.0	12.0	91.1	0.78	9.52	89.70	-0.111	Yes
E, (100) 1° to (011)	5.0	12.0	91.1	0.74	10.07	89.19	-0.146	Yes
F, (100) 4° to (111)	5.0	10.5	91.1	0.65	8.83	90.52	-0.052	Yes

The growth rate, calibration of flux ratios, and substrate temperature for these samples is described in Chapter 3. The As overpressure is set at 1% for the InAsSbBi growths examined in this chapter.

A schematic of the surfaces of the on-axis and two offcut substrates are shown in Figure 24. The offcut result in terraces and step edges. Terraces run along the $[01\bar{1}]$ direction on

(100) offcut surfaces. In both cases, monolayer step edges form along the [011] and [01$\bar{1}$] directions, which results in a smooth terrace edge.

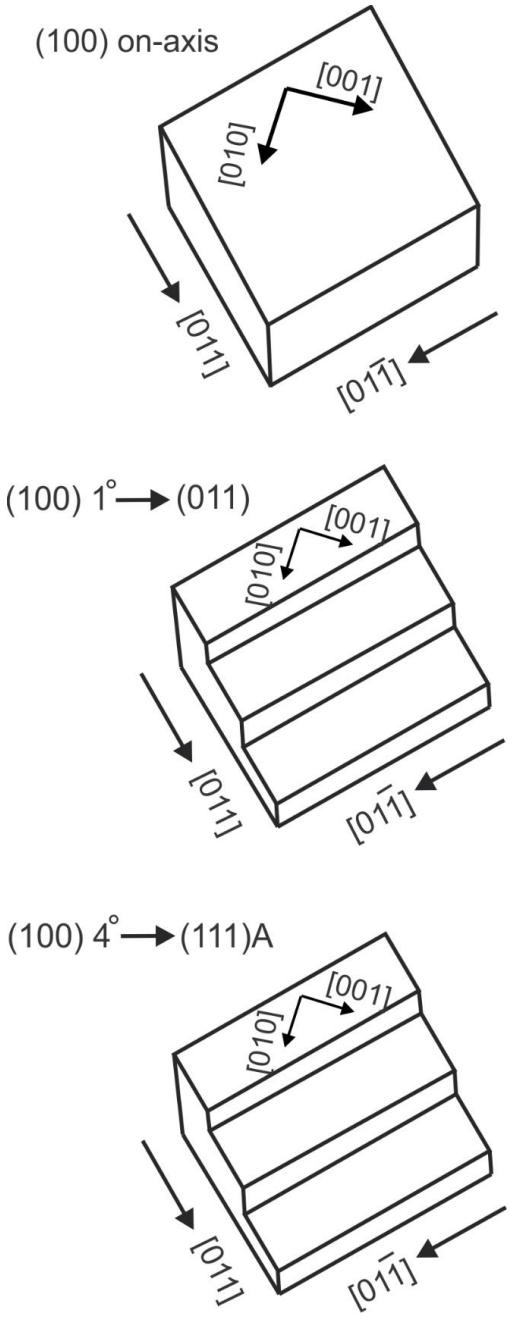

Figure 24: Surfaces of flat on-axis and terraced offcut substrates. The terrace edges are smooth and in the [01$\bar{1}$] direction on (100) surfaces offcut to (011) and to (111)A.

4.2 Surface morphology

Nomarski optical microscopy images of the surface of the three InAsSbBi samples are shown in Figure 25. The images are 200 μm wide by 150 μm high and the significant growth conditions are shown for each. Surface droplet features are observed on all samples. These features have respective diameters and densities of 3 μm and 5×10^5 cm^{-2} in sample D, 5 μm and 7×10^5 cm^{-2} in sample E, and 3 μm, and 8×10^5 cm^{-2} in sample F. Additionally, sample E (Figure 25b) with step edge density 5.7×10^5 cm^{-1} exhibits anisotropic surface droplet features, indicating preferential diffusion of the Bi atoms along the $[01\bar{1}]$ step edges.

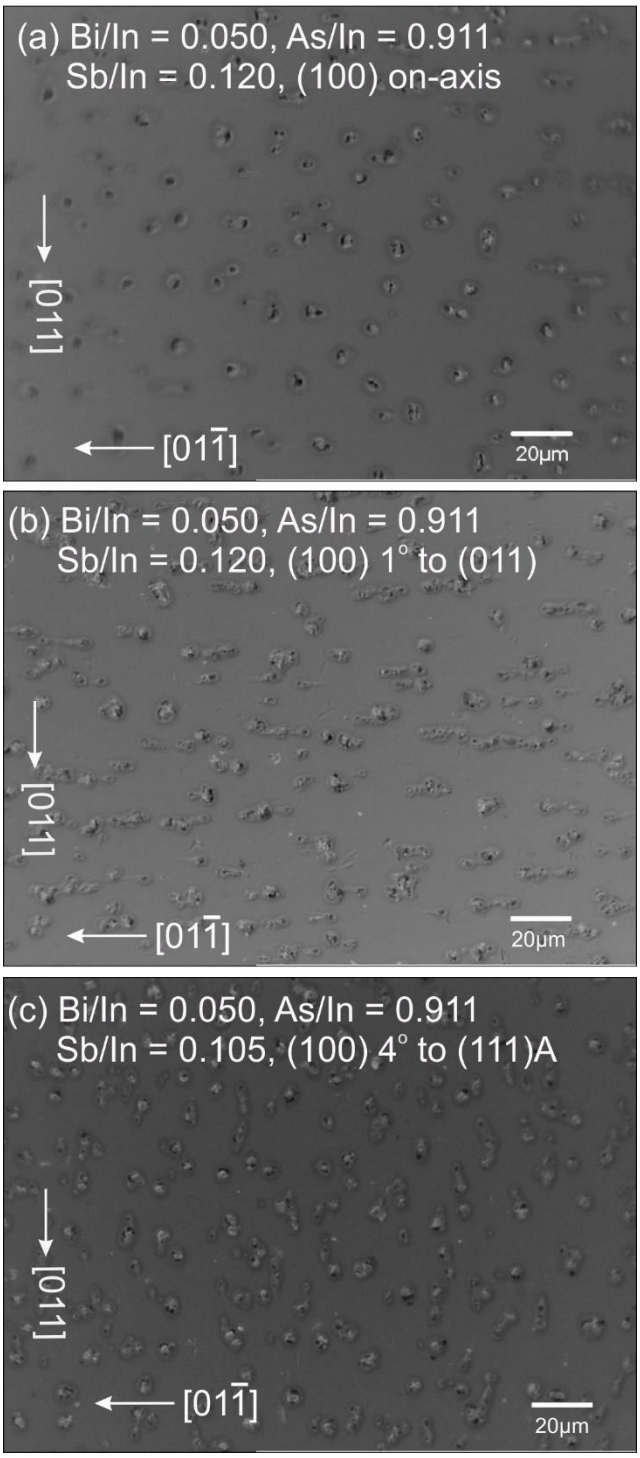

Figure 25: Nomarski optical measurements of the surface morphology of InAsSbBi samples D, E, and F, shown in (a) through (c) respectively. Image dimensions are 200 μm by 150 μm. The Bi/In, As/In, and Sb/In flux ratios and substrate orientation are shown for each sample.

Atomic force microscopy images of the surface morphology of InAsSbBi samples D through F, labeled a through c, are shown in Figure 26. The images are 100 µm by 100 µm on the left with a zoomed in 5 µm by 5 µm measurement on the right. The root mean square (RMS) roughness over each area imaged is shown in Table 8. With droplets over 200 nm high, the surfaces have a RMS roughness around 40 nm on the 100 µm length scale. The surface between the large droplet features is relatively smooth with a RMS roughness that is less than 1 nm on the 5 µm length scale. The difference in RMS roughness values attributed to minimization of surface energy by introduction of uniform array of monoatomic growth steps.[47]

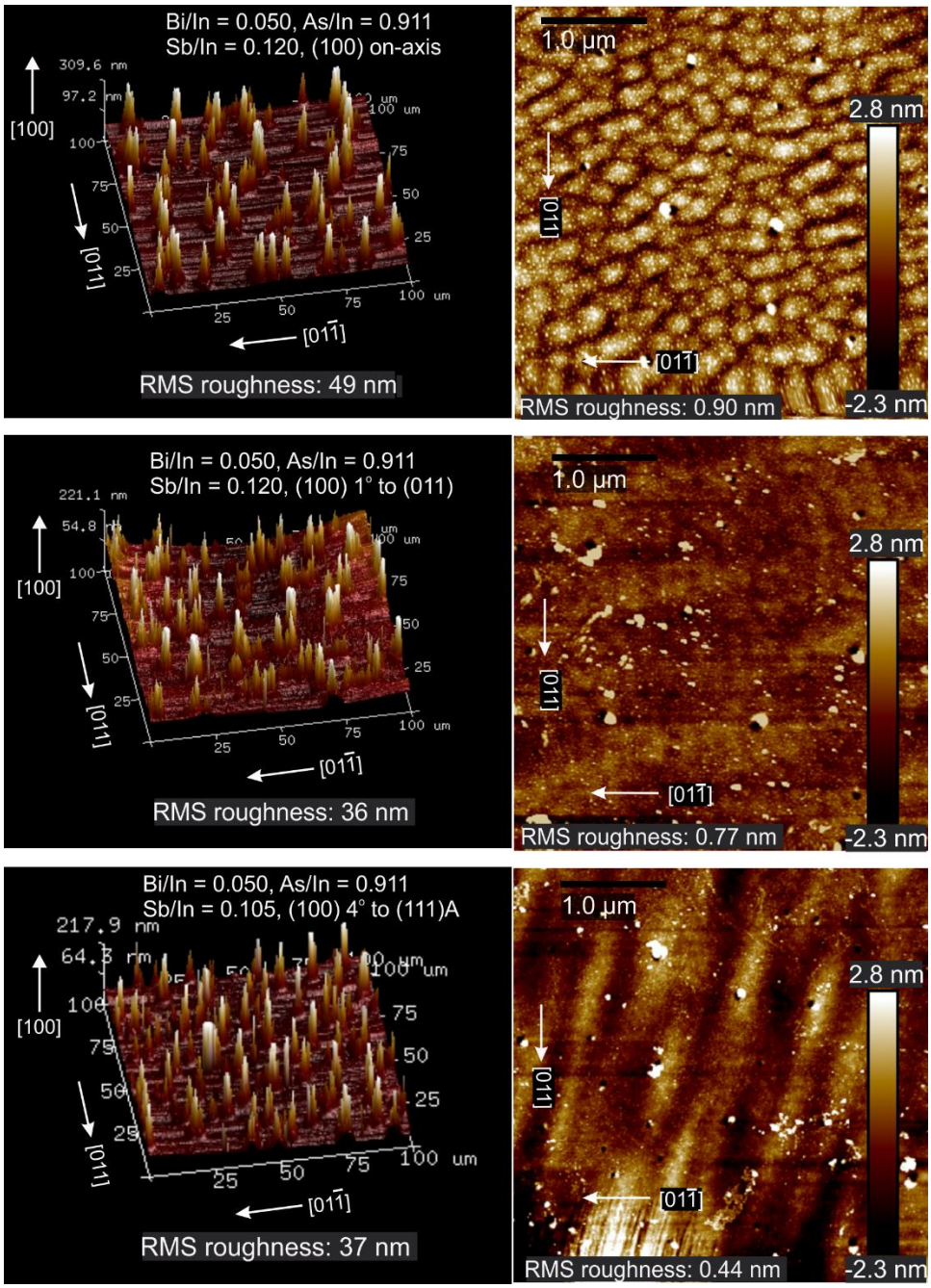

Figure 26: Atomic force microscopy images of the surface morphology of InAsSbBi samples D, E, and F, shown in (a) through (c) respectively. Images dimensions are 100 µm by 100 µm on the left and 5 µm by 5 µm on the right. The root mean square (RMS) roughness range from 45 nm to 37 nm over 100 µm length scale and 0.90 nm to 0.44 nm over 5 µm length scale. The Bi/In, As/In, and Sb/In flux ratios and substrate orientation are shown for each sample.

Table 8. Root mean square (RMS) surface roughness of samples D through F from AFM measurements over surface areas of 100 μm by 100 μm, 5 μm by 5 μm, and 1 μm by 1 μm. The growth information is provided for the InAsSbBi layer of each sample.

Sample	V/III flux ratios			RMS roughness (nm)		
	Bi/In	Sb/In	As/In	100 μm by100 μm	5 μm by 5 μm	1 μm by 1 μm
D, (100)	0.050	0.120	0.911	49	0.90	0.46
E, (100) 1° to (011)	0.050	0.120	0.911	36	0.77	0.52
F, (100) 4° to (111)	0.050	0.105	0.911	37	0.44	0.41

The droplet sizes and densities, an estimation of the fraction of the surface covered by droplets, and the average droplet volume per unit area are reported in Table 9. The droplet volume relative to the InAsSbBi layer volume is respectively 5%, 10%, and 7% for samples D through F. Sample E with preferential diffusion along the $[01\bar{1}]$ direction has the largest surface droplet coverage.

Table 9. Surface droplet density, diameter, height, fraction of surface area covered, and aggregate volume per unit area for each measurement method for samples D, E, and F.

Sample	D, (100) on-axis		E, (100) 1° to (011)		F, (100) 4° to (111)A	
Method	Nomarski	AFM	Nomarski	AFM	Nomarski	AFM
Density (cm^{-2})	5×10^5	5×10^5	7×10^5	7×10^5	8×10^5	8×10^5
Diameter (μm)	3	3	5	5	3	3
Average Height (nm)	-	310	-	220	-	220
Surface Coverage (%)	4	4	10	10	6	6
Volume/unit area (nm)	-	11	-	22	-	14

4.3 Step edges and Lateral composition modulation

The overall microstructure of the InAsSbBi layers is examined using cross-sectional TEM. Low magnification bright-field TEM micrographs from the three InAsSbBi samples are presented in Figure 27. The results indicate that the 210 nm thick InAsSbBi layers are pseudomorphic with no visible defects over large lateral distances. Furthermore, contrast modulation due to inhomogeneous composition[34,36] with a modulation period of approximately 30 nm is observed in samples D and F shown in Figures. 27a, and 27c respectively. Lateral composition modulation is not observed in sample E (see Figure 27b), which has relatively less density of step edges.

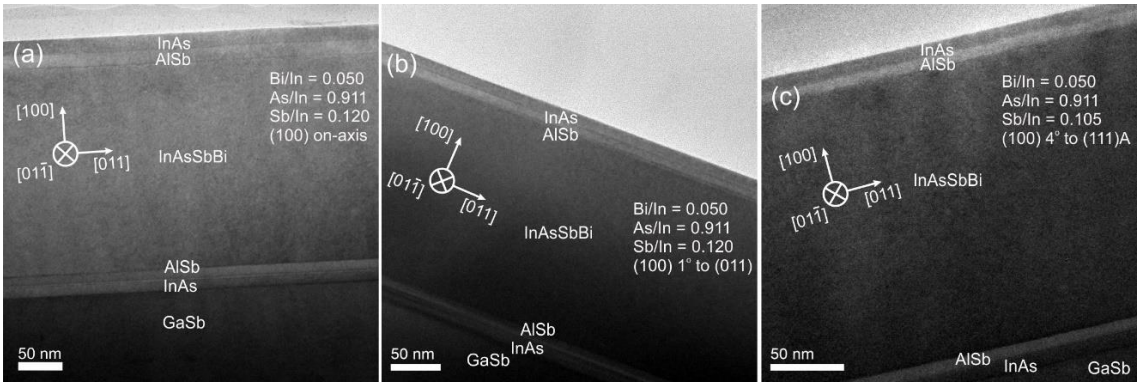

Figure 27: Bright field cross-section TEM images in the [01$\bar{1}$] projection showing the overall microstructure of InAsSbBi samples D, E, and F, in (a) through (c) respectively. Contrast modulation with period of approximately 30 nm is observed perpendicular to the growth plane in a, and c. The Bi/In, As/In, and Sb/In flux ratios and substrate orientation are shown.

The Bi mole fraction is estimated from chemically the sensitive (200) dark-field images using the method developed by Bithell and Stobbs as mentioned previously in Chapter 3. The Sb mole fraction $y(x, a_{InAsSbBi})$ is a function of the Bi mole fraction x and the unstrained InAsSbBi lattice constant $a_{InAsSbBi}$ provided by the XRD analysis in the next section.

The lateral Bi mole-fraction profiles obtained from chemically sensitive (200) dark field images are shown in Figure 28. The specimen cross sections examined are approximately 80 nm thick. The Bi mole fraction varies laterally from 0.73% to 0.83% with an average of 0.78% in sample D, from 0.72% to 0.75% with an average of 0.74% in sample E, and from 0.63% to 0.69% with an average of 0.65% in sample F. The average InAsSbBi mole fractions are also reported in the TEM + XRD section of Table 10. In comparison, the combined photoluminescence (PL) and XRD measurements specify an average Bi value[5] of 0.71% for sample D, 0.81% for sample E, and 0.58% for sample F, which are reported in the PL + XRD section of the table. The Bi incorporation coefficient defined as the ratio of the Bi mole fraction to the incident Bi/In flux ratio is also provided. The results indicate that the presence step edges on the offcut surfaces does not significantly impact Bi incorporation.

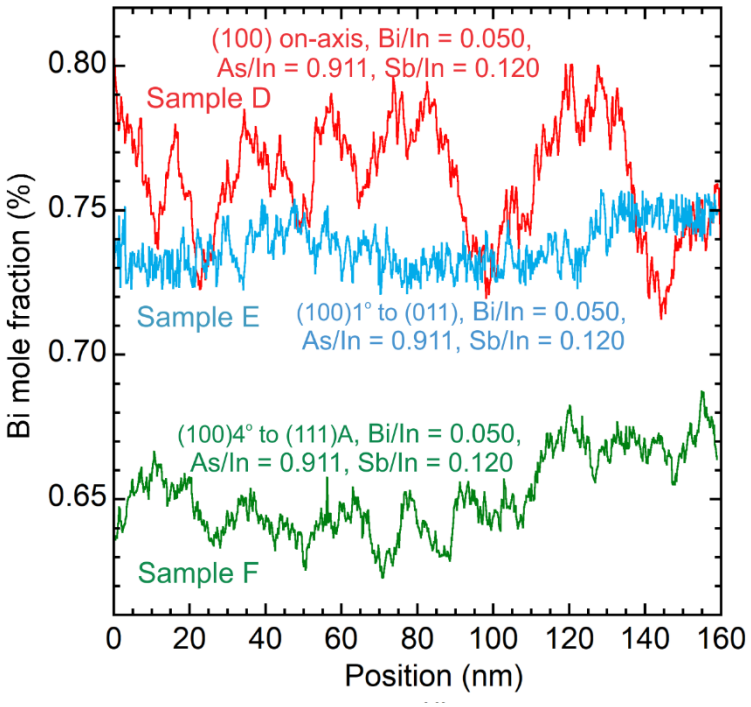

Figure 28: Lateral Bi mole fraction profiles obtained from chemically sensitive 200 dark-field images of InAsSbBi samples D, E, and F, with the significant growth conditions shown for each.

Table 10. InAsSbBi substrate orientation, average group-V mole fractions (%), and Bi incorporation coefficient (%) determined from X-ray diffraction (XRD) and dark field transmission electron microscopy (TEM + XRD) or photoluminescence[5] (PL + XRD).

Sample	TEM + XRD				PL + XRD			
	Bi	Sb	As	Bi Incorpo-ration (%)	Bi	Sb	As	Bi incorpo-ration (%)
D, (100)	0.78	9.52	89.70	15.6	0.71	9.61	89.68	14.2
E, (100) 1° to (011)	0.74	10.07	89.19	14.8	0.81	10.05	89.14	16.2
F, (100) 4° to (111)	0.65	8.83	90.52	13.0	0.58	8.92	90.50	11.6

High angle annular dark field scanning transmission electron micrographs from samples D, E, and F are shown in Figures 29a, b, and c respectively. Intensity line profiles across the areas marked in the micrographs are shown below the images. Lateral quasi-periodic composition variation with a period of approximately 30 nm is observed in samples D and F, while lateral composition modulation is not observed in sample E. These results are consistent with the bright field TEM micrographs in Figure 27 and the lateral Bi mole fraction profiles in Figure 28.

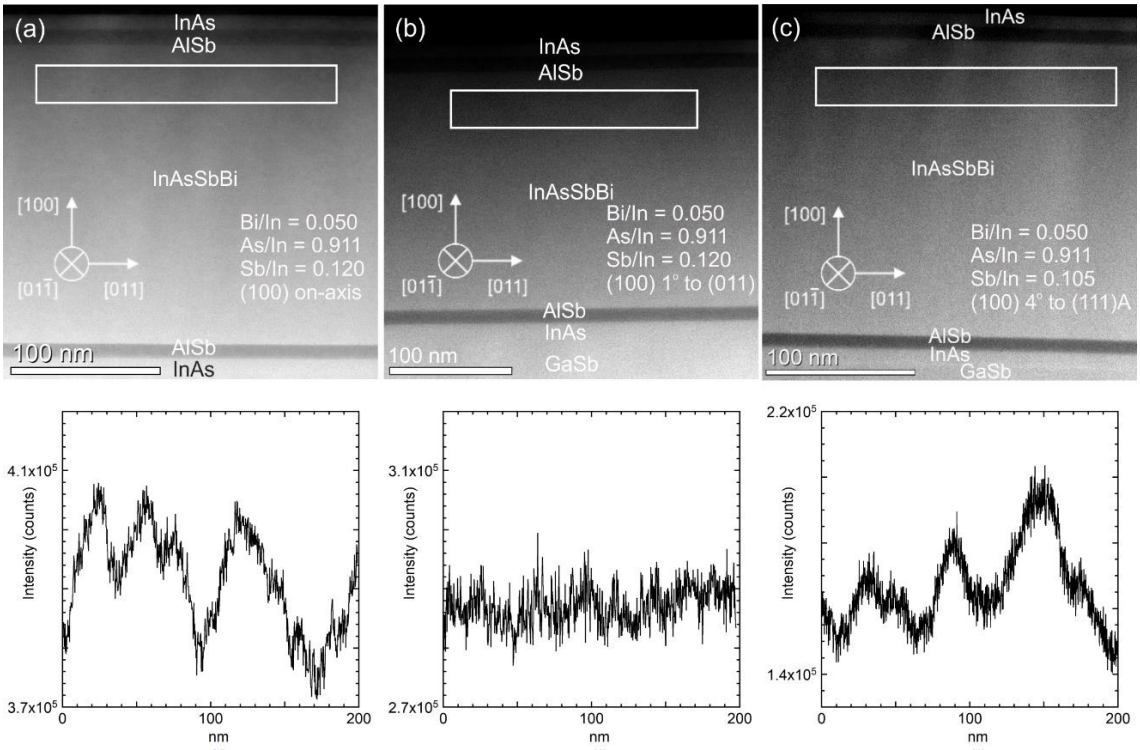

Figure 29: High angle annular dark field scanning TEM images in the [01$\bar{1}$] projection showing the overall microstructure of InAsSbBi (samples D, E, and F), in (a), (b), and (c) respectively. Line scans of the image intensity from the regions marked by the rectangles parallel to the layer interface are shown. Contrast modulations perpendicular to the growth direction in (a) and (c) show composition inhomogeneity with a modulation period of

approximately 30 nm. The Bi/In, As/In, and Sb/In flux ratios and substrate orientation are shown for all samples.

Atomic resolution aberration-corrected high-angle-annular dark-field scanning transmission electron micrographs from samples D, E, and F are shown in Figures 30a, b, and c respectively. Images in the [01$\bar{1}$] projection shows the top and bottom interfaces of InAsSbBi samples. Individual atomic columns are observed.[48] The micrographs indicate that the InAsSbBi layers have high quality interfaces with no misfit dislocations. Atomic steps are observed on the surface of the offcut samples E and F.

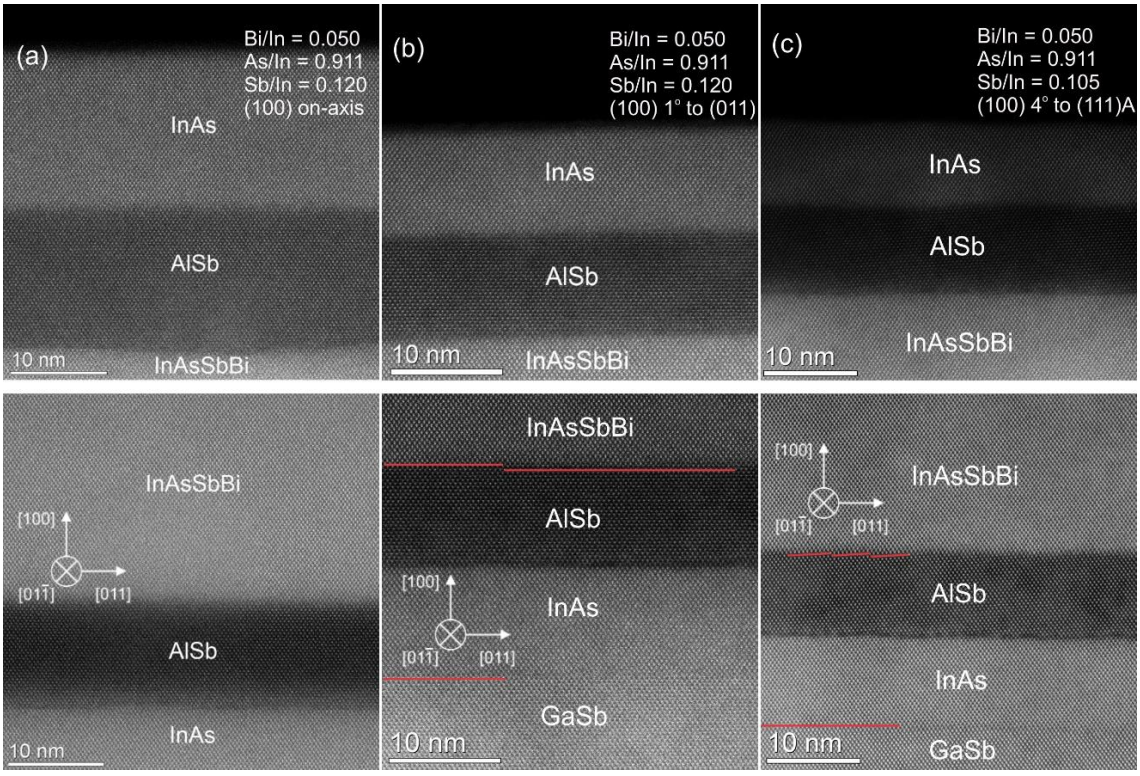

Figure 30: Atomic resolution high-angle-annular dark-field scanning TEM images in the [01$\bar{1}$] projection showing the top and bottom interfaces of InAsSbBi samples D,E, and F, in (a) through (c) respectively. Atomic steps are observed and marked in (b) and (c). The Bi/In, As/In, and Sb/In flux ratios and substrate orientation are shown.

4.4 Layer tilt and Out of plane distortion

Diffraction angle space maps derived from (400) measurements in the [011] directions are shown in Figures 31a, b, and c for samples D, E, and F. The offset angle $\omega - \theta$ is shown on the vertical axis and the diffraction angle difference $(\theta_{GaSb} - \theta)/\tan\theta_{GaSb}$ is shown on the horizontal axis. The position of GaSb substrate and the compressively strained InAsSbBi layer peaks are identified and marked as solid black circles in each map. The out-of-plane distortion $\varepsilon_{\perp}$ of the InAsSbBi layer relative to the substrate peak is shown in the horizontal direction. The strained InAsSbBi layers grown on misoriented offcut substrates are observed to be tilted relative to the (100) substrate lattice. The tilt angle τ is shown in the vertical direction on each plot. As is apparent in the figures, the magnitude of the InAsSbBi layer tilt is proportional to the out of plane distortion and substrate offcut angle.

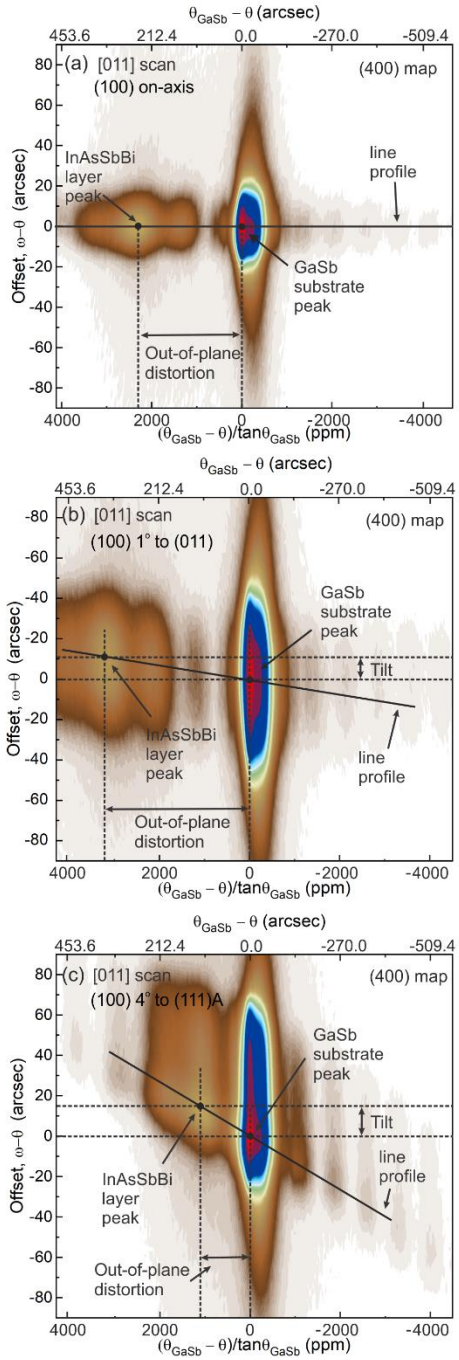

Figure 31: Diffraction angle area-scan contour-plots about the symmetric (400) reflection for samples D, E, and F labelled (a), (b), and (c). The GaSb substrate and InAsSbBi layer peaks are shown as solid black circles. Also shown is the out-of-plane distortion $\varepsilon_{\perp}$ and the InAsSbBi layer tilt angle τ that results from the growth of strained material on offcut substrates. The illustrated (400) line profile goes through both the substrate and layer peaks and is extracted from the area scan data for dynamical simulation analysis.

Coupled scans are collected by repeating a sequence of offset angle values, $\omega - \theta$ as shown in Figure 32a to obtain diffraction angle space maps. Schematic shows the plane of diffraction, the incident beam is inclined at an angle, θ with respect to crystal planes; diffracted beam is at an angle, 2θ with respect to the incident beam, and the offset angle is $\omega - \theta$. Schematic of the (400) X-ray diffraction measurements in reciprocal space are shown in Figure 32b. The layer tilt angle is observed via the scan of the offset angle $\omega - \theta$. The diffraction angle space maps show the diffraction peaks for each scan direction for a given sample, indicating the crystallographic distortion of the strained InAsSbBi layers.

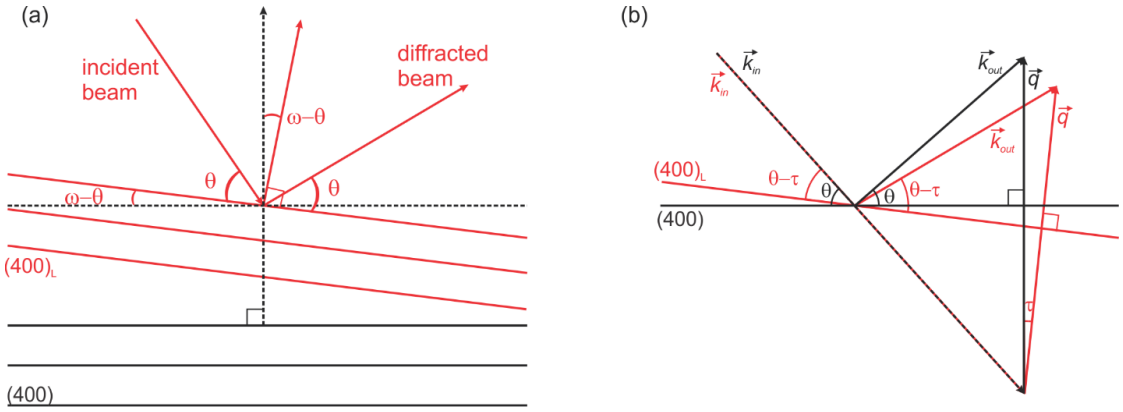

Figure 32: (a) Illustration showing the plane of diffraction in real space, the incident beam is inclined at an angle θ with respect to crystal planes; diffracted beam is at an angle 2θ with respect to the incident beam, and the offset angle is $\omega - \theta$. (b) Illustration showing the plane of diffraction in reciprocal space, where the incident beam is inclined at an angle θ with respect to crystal planes. The diffracted beam is at an angle 2θ with respect to the incident beam, and the tilt angle is τ.

In order to perform dynamical simulations of coupled diffraction scans that go though both the substrate peak and the layer peak, a line profile of intensity as a function of the diffraction angle θ is extracted from the (400) angle maps shown in Figure 31. For the offcut substrates, the line profile data is adjusted for layer tilt by projecting the intensity profile onto the horizontal axis. The line profiles are plotted in Figure 33 as a function of

diffraction angle θ for samples D, E, and F. Broadening of the InAsSbBi layer peak in samples D and F indicates fluctuations in the material composition within the layer. The lower intensity of the InAsSbBi layer peak in sample E is possibly due to the larger accumulation of excess Bi on the surface. In addition to the compressively strained InAsSbBi layer peak, a tensile peak is observed near the GaSb substrate peak that is due to the unintentional incorporation of As in the GaSb buffer. The dilute As mole fractions are 0.17% and are insufficient to induce relaxation in the 500 nm thick buffer layer. The unintentional As originates from the As background pressure in the growth chamber. The Pendellösung fringes arise in InAsSbBi layer due to thin film X-ray interference from the InAs and AlSb layers.

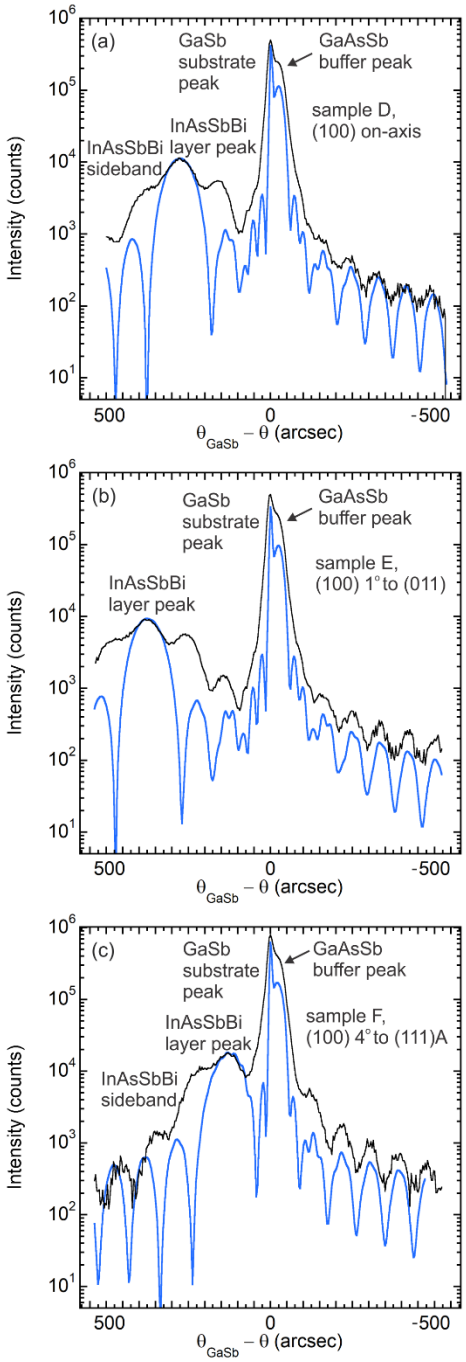

Figure 33: Extracted scans from area scans as contour plots with angle scales from (400) reflection and simulations for InAsSbBi samples D, E, and F, shown in (a) through (c) respectively. The GaSb substrate peak, compressive InAsSbBi layer peak, the tensile GaAsSb buffer peak are shown. Also shown in samples D and F is the compressive InAsSbBi sideband peak that results from composition fluctuations in the layer. The Bi/In, As/In, and Sb/In flux ratios are 0.05, 0.91, and 0.10 to 0.12 for all the samples.

In the simulations, the InAsSbBi layers are assumed to be pseudomorphic as the lattice mismatch is sufficiently small that the critical thickness[7] significantly exceeds that of the InAsSbBi layer in all samples. The InAsSbBi simulated epilayer thickness, in-plane biaxial strain, and out-of-plane distortion determined from the simulations are summarized in Table 11. X-ray diffraction pattern that exhibit strong Pendellösung fringes due to thin film interference requires a dynamical simulation that accounts for these effects to determine the precise diffraction angles. The dynamical simulation is used to ascertain the actual separation between the Bragg angles of the GaSb substrate and the coherently strained InAsSbBi layer, the difference is 7.5, 8.5, and 9.5 arcsec less for samples D, E, and F compared to the peak separation determined directly from the diffraction pattern peaks. The significance of the performing dynamical simulations on the results is that shifts in the diffraction peak due to thin film interference are taken into account, as it is the Bragg angle that determines the measured parameters of the layer.

Also shown in Table 11 are the tilt angle, and the offcut angle. The tilt angle dependence on the measured out-of-plane distortion and the offcut angle are further discussed with the model and equation later in the discussion section. The exact manufacturer specified offcut angle values of the substrate are $0.00° \pm 0.02°$, $0.96° \pm 0.00°$, and $4.04° \pm 0.00°$ and these are used in the calculation.[5]

Table 11. The substrate orientation, scan direction, simulated thickness, diffraction angle difference, out-of-plane distortion, in-plane strain, offcut angle, tilt angle epilayer for samples D, E, and F.

Sample		D (100) on-axis	E (100) 1° to (011)	F (100) 4° to (111)A
Scan direction		[011]	[011]	[011]
Simulated thickness (nm)		194	190	190
$\theta_{GaSb} - \theta_{Peak}$ (arcsec)		288.0	385.2	140.4
$\theta_{GaSb} - \theta_{InAsSbBi}$ (arcsec)		280.5	376.7	130.9
Out-of-plane distortion $\varepsilon_{\perp}$ (%)		0.235	0.313	0.107
In-plane biaxial strain (%)		-0.11132	-0.14905	-0.05183
Offcut angle, δ	(deg)	0.00 ± 0.02	0.96 ± 0.00	4.04 ± 0.00
	(arcsec)	0	3500	14500
Layer tilt, τ (arcsec)		0.0 ± 0.0	10.8 ± 0.0	15.3 ± 1.6

Schematic illustrating Bragg's law in reciprocal space for a tilted layer (in red) on a substrate (in black) for (511) plane is shown in Figure 34. The incident beam is represented as a wave vector $\vec{k}_{in}$ and the diffracted beam is represented as a wave vector $\vec{k}_{out}$. These wave vectors together define a scattering vector $\vec{q}$. For a strained epilayer, the reciprocal lattice point is shifted due to tilt. For further, strain analysis this tilt angle, τ has to be taken into consideration. By rotating the layer reciprocal lattice point in the reciprocal space by tilt angle along the ω scan direction the zero-tilt layer reciprocal lattice point is obtained. This is shown as shift given by difference in the reciprocal lattice vector parallel and perpendicular components indicated as $\Delta\vec{q}_{\parallel}$ and $\Delta\vec{q}_{\perp}$.

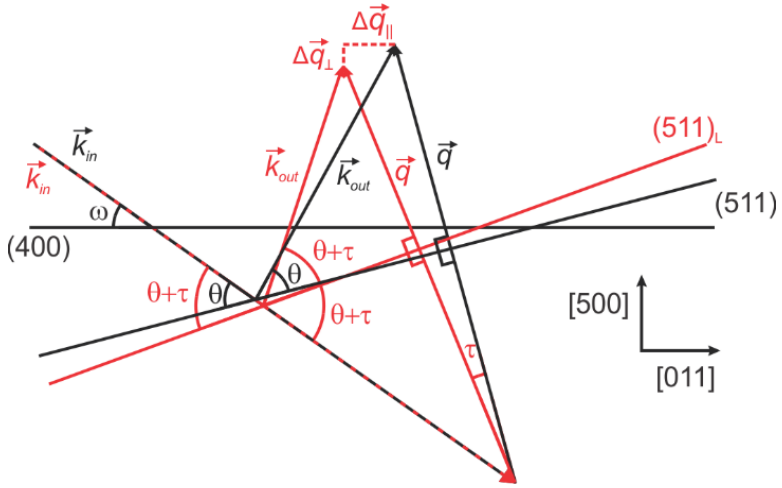

Figure 34: Illustration of Bragg's law in reciprocal space for the tilted layers (in red) and substrate (in black) for (511) plane. Incident beam is represented as a wave vector $\vec{k}_{in}$ and the diffracted beam is represented as a wave vector $\vec{k}_{out}$. These wave vectors together define a scattering vector $\vec{q}$. Difference in the reciprocal lattice vector parallel and perpendicular components are indicated as $\Delta\vec{q}_{\parallel}$ and $\Delta\vec{q}_{\perp}$.

The two reciprocal space maps taken about the asymmetric [51$\bar{1}$] and [511] reflections are shown in Figures 35a, b, and c for samples D, E, and F. The reciprocal lattice vector parallel and perpendicular components are on horizontal and vertical axes respectively. The positions of the peak diffraction intensities for the GaSb substrate and the strained InAsSbBi layer are identified and marked as solid circles in each reciprocal lattice map. The vertical line passing through the substrate reciprocal lattice point in [500] direction corresponds to the same in-plane lattice constant and hence a fully strained state in reciprocal space. Also shown for a strain tilted layer are the shifts $\Delta\vec{q}_{\parallel}$ and $\Delta\vec{q}_{\perp}$along the reciprocal lattice vector parallel and perpendicular components to obtain zero tilt layer reciprocal lattice points.

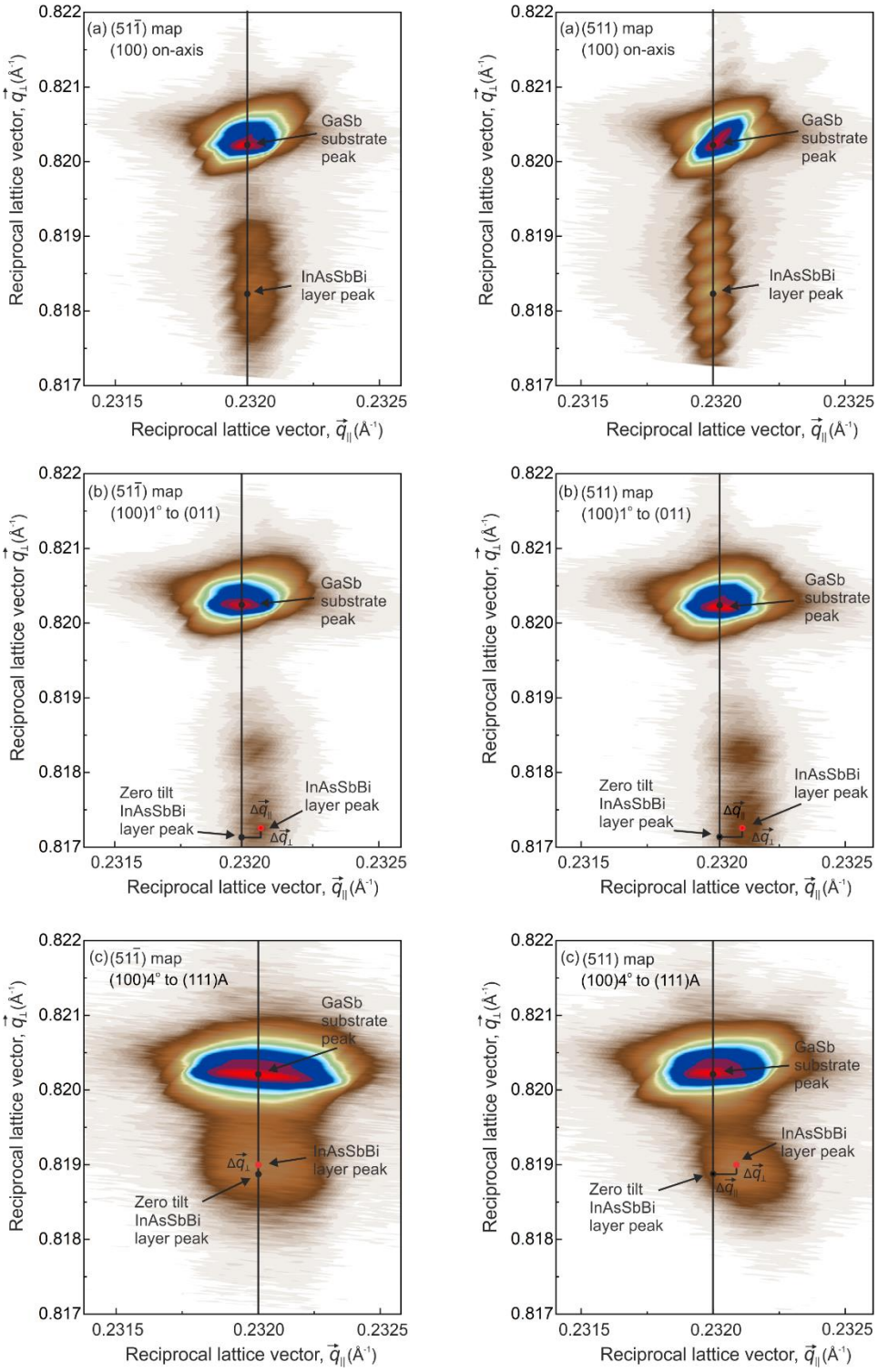

Figure 35: Reciprocal space area scan contour plots about the asymmetric (511) reflection for samples D, E, and F labelled a, b, and c. The measurements shown on the left are taken

along the [$01\bar{1}$] direction and the ones on the right along the [011] direction. The GaSb substrate and InAsSbBi layer reciprocal lattice points are shown as black solid circles respectively. Also shown are the strain tilted layer reciprocal lattice points as red solid circles with the shifts $\Delta\vec{q}_{\parallel}$ and $\Delta\vec{q}_{\perp}$along the reciprocal lattice vector parallel and perpendicular components to obtain zero tilt layer reciprocal lattice points. A vertical line crossing the substrate reciprocal lattice point corresponds to the fully strained state.

These maps show that both the substrate and zero tilt layer reciprocal lattice points lie along the fully strained line. This indicate that the InAsSbBi layer is pseudomorphic. Further, the InAsSbBi reciprocal lattice point lies below that of the substrate confirming the compressive strain state in all the samples.

The measured in-plane and out-of-plane distortions from the (511) maps is shown in Table 12 below. The error bar is reported as standard deviation in three separate in-plane and out-of-plane lattice constants measured in each direction for each sample.

Table 12. The substrate orientation, directions, and measured in-plane and out-of-plane distortion from the (511) maps for samples D, E, and F.

Sample	Substrate orientation	Direction	$\frac{a_{\parallel}-a_{GaSb}}{a_{GaSb}}$(%)	$\frac{a_{\perp}-a_{GaSb}}{a_{GaSb}}$(%)
D	(100) on-axis	[$01\bar{1}$]	-0.0271±0.0312	0.2573±0.0132
		[011]	-0.0239±0.0666	0.2294±0.0739
E	(100) 1° to (011)	[$01\bar{1}$]	-0.0119±0.0321	0.3303±0.0721
		[011]	0.0111±0.0424	0.3422±0.0105
F	(100) 4° to (111)A	[$01\bar{1}$]	-0.0169±0.0313	0.1476±0.0132
		[011]	0.0009±0.0200	0.1476±0.0200

4.5 Discussion of layer tilt and lateral composition modulation

For growth on an on-axis substrate, the epilayer lattice planes are registered in-the-plane to the substrate lattice, where a strained epilayer undergoes tetragonal distortion in the vertical out-of-plane direction to accommodate lattice mismatch. When the substrate is offcut, the epilayer boundary conditions are such that the epilayer is registered both in-the-plane on the step terrace and out-of-the-plane at the step edge. As a result, a strained epilayer tilts relative to substrate lattice planes to accommodate the lattice mismatch and boundary conditions. The diagram of the tilt is shown for a compressively strained layer in the Figure 36, where the vertical and horizontal lattice planes of the epilayer (in red) are registered to the respective lattice planes of the substrate (in black). The substrate offcut angle is labeled δ (delta) for offcut and the epilayer tilt angle is labeled τ (tau) for tilt. As the growth progresses away from the substrate, the distorted epilayer lattice planes form a tilted set of orthogonal lattice planes as shown in red in the cross-section in figure, which is valid for epilayers that are much thicker than the epilayer lattice constant.

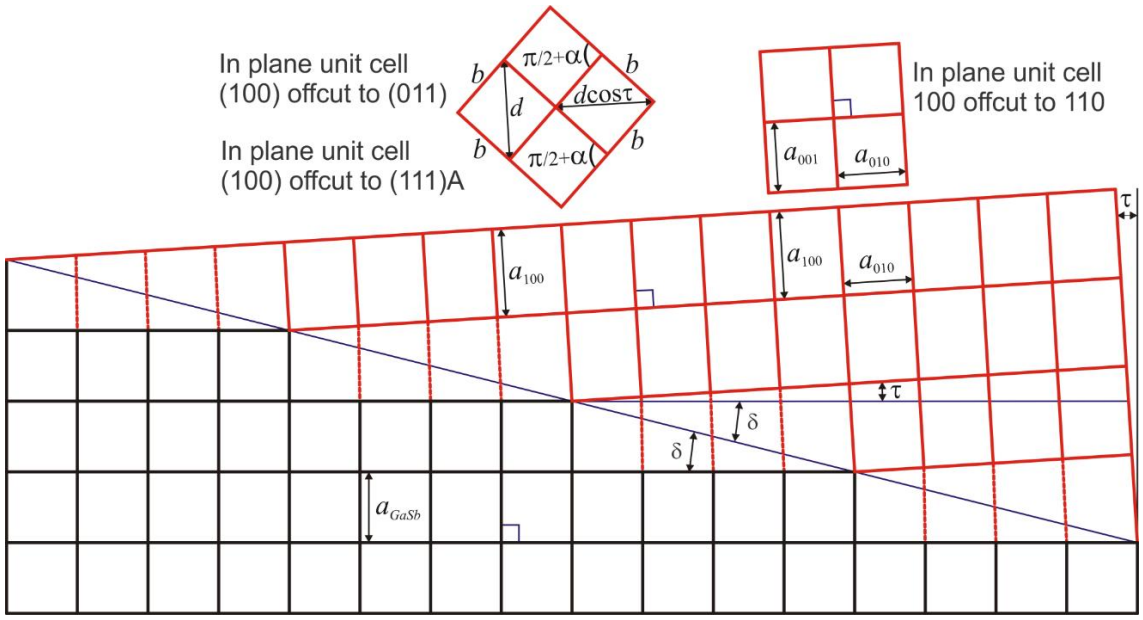

Figure 36: Schematic of InAsSbBi layers grown on offcut GaSb substrates illustrating strain induced crystallographic tilt. The vertical and horizontal lattice planes of the epilayer (in red) are registered to the respective lattice planes of the substrate (in black). The substrate offcut angle is labeled δ (delta) for offcut and the epilayer tilt angle is labeled τ (tau) for tilt. The substrate lattice constant and the epilayer out-of-plane lattice constant in the [100] direction $a_{\perp}$ are labeled a_{GaSb} and a_{100} respectively. In plane unit cell is shown for offcut samples on the top. In sample with offcut towards (110) the in-plane lattice distortions in the [010] direction along the offcut slope and in the [001] direction perpendicular to the offcut slope labeled a_{010} and a_{001}. In samples E and F the in-plane distortion of the epilayer unit cell is distorted diagonally into the step edge where the lengths of the sides of the in-plane unit cell are equal, shown as length b in the figure. The angular distortion of the in-plane unit cell is shown as $\pi/2 + \alpha$.

For the tilted epilayer, the ratio of the out-of-plane lattice constant a_{100} and the in-plane substrate lattice constant a_{GaSb} is

$$\frac{a_{100}}{a_{GaSb}} = \varepsilon_{\perp} + 1 = \frac{\sin(\tau + \delta)}{\sin\delta} = \cos\tau + \frac{\sin\tau}{\tan\delta}, \tag{4.1}$$

where δ is the substrate offcut angle, τ is the measured tilt angle of the epilayer, and $\varepsilon_{\perp}$ is the measured out-of-plane distortion, with

Solving for tilt angle in terms of the out-of-plane distortion and offcut angle

$$\tau = \sin^{-1}(\sin\delta\,(\varepsilon_\perp + 1)) - \delta\,, \tag{4.2}$$

$$= \left[\sin^{-1}(\sin\delta) + \left[\frac{\sin\delta}{\sqrt{1-\sin^2\delta}}\right]\varepsilon_\perp + \frac{1}{2}\left[\frac{\sin^3\delta}{\left(\sqrt{1-\sin^2\delta}\right)^3}\right]{\varepsilon_\perp}^2 + \cdots\right] - \delta\,,$$

$$\tau = \varepsilon_\perp \tan\delta\left(1 + \frac{\varepsilon_\perp \tan^2\delta}{2} + \cdots\right) \cong \varepsilon_\perp \tan\delta\,, \tag{4.3}$$

where the approximation is to first order in the out-of-plane distortion that is typically small in coherently strained epilayers. Since epilayer tilt, out-of-plane distortion, and substrate offcut can be measured, the relationships in the model shown in Figure 36 and Equations 4.1 through 4.3 is experimentally verified in Figure 37. Furthermore, for small offcut angles $\delta^2/3 \ll 1$ and $\tau \cong \varepsilon_\perp\delta$.

The measured tilt angle τ is plotted as a function of measured out-of-plane distortion $\varepsilon_\perp$ times the tangent of the offcut angle in Figure 37 for the three samples. Data points shown as solid red circles correspond to out-of-plane distortion measured from diffraction angle area-scan contour-plots about the symmetric (400) reflection shown in Figure 31. Data points shown as solid cyan circles correspond to out-of-plane distortion measured from extracted scans by performing dynamical simulations shown in Figure 33. The error bar is reported as standard deviation of four separate peak measurements using the centroid peak finding routine in Xpert epitaxy software.[13] The solid black line is the model $\varepsilon_\perp \tan\delta$ described in Figure 36 and Equation 4.3.

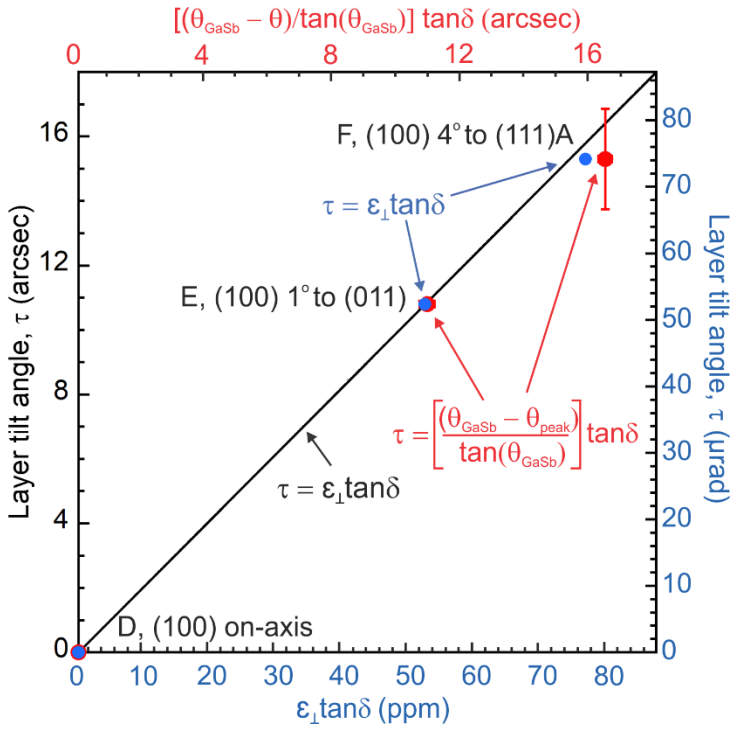

Figure 37: The measured tilt angle τ versus the measured out-of-plane distortion $\varepsilon_{\perp}$ multiplied by the tangent of the substrate offcut angle δ is plotted for each of the [400] measurement for samples D, E, and F. Data points shown as solid red circles correspond to out-of-plane distortion measured from diffraction angle area-scan contour-plots about the symmetric (400) reflection shown in Figure 31. Data points shown as solid blue circles correspond to out-of-plane distortion measured from extracted scans by performing dynamical simulations shown in Figure 33. The solid black curve is the model $\varepsilon_{\perp} \tan \delta$ described in Figure 36 and Equation. 4.3.

In the case of sample with (100) offcut toward (110) the relationship between the substrate lattice constant a_{GaSb} and the epilayer lattice constants a_{100} in the out-of-plane [100] direction, a_{010} in the in-plane [010] direction along the offcut slope, and a_{001} in the in-plane [001] direction perpendicular to the offcut slope, are

$$a_{001} = a_{GaSb} \tag{4.4}$$

$$a_{010} = \cos \tau \, a_{GaSb} \tag{4.5}$$

$$a_{100} = (\varepsilon_{\perp} + 1)a_{GaSb} = \left(\cos\tau + \frac{\sin\tau}{\tan\delta}\right)a_{GaSb} \tag{4.6}$$

In this sample the epilayer lattice planes undergo orthorhombic distortion that is expressed in terms of the distortion of the three orthogonal lattice planes of the unit cell, with

$$\frac{a_{010}}{a_{001}} - 1 = \cos\tau - 1 = -\frac{\tau^2}{2}\left(1 - \frac{\tau^2}{12} + \cdots\right) \tag{4.7}$$

$$\frac{a_{100}}{a_{010}} - 1 = \frac{\tan\tau}{\tan\delta} = \frac{\tau}{\tan\delta}\left(1 + \frac{\tau^2}{3} + \cdots\right) \tag{4.8}$$

$$\varepsilon_{\perp} = \frac{a_{100}}{a_{001}} - 1 = \frac{\sin\tau}{\tan\delta} + \cos\tau - 1 = \frac{\tau}{\tan\delta}\left(1 - \frac{\tau\tan\delta}{2} - \frac{\tau^2}{6} + \cdots\right) \tag{4.9}$$

Since the in-plane distortion is very small (second order in tilt angle) the orthorhombic distortion can be approximated with an average tetragonal distortion

$$\overline{\varepsilon_{\perp}} = \frac{a_{100}}{\overline{a_{\parallel}}} - 1 = \frac{2a_{100}}{a_{001} + a_{010}} - 1 = \frac{2(\varepsilon_{\perp} + 1)}{1 + \cos\tau} - 1 = \frac{\varepsilon_{\perp} - (\cos\tau - 1)/2}{1 + (\cos\tau - 1)/2} \cong \varepsilon_{\perp}\,. \tag{4.10}$$

In the case of sample E and F (100 offcut toward 011 and 111) the in-plane distortion of the epilayer unit cell is more complicated in that the in-plane unit cell is distorted diagonally into the step edge. This results in the monoclinic distortion of the epilayer lattice in the special case where the lengths of the sides of the in-plane unit cell are equal, shown as length b in Figure 36. The angular distortion of the in-plane unit cell is $\pi/2 + \alpha$ for compressively strained epilayers.

$$a_{010} = a_{001} = b = \frac{a_{GaSb}}{\sqrt{2}\sin(\pi/4 + \alpha/2)} \tag{4.11}$$

$$a_{100} = (\varepsilon_{\perp} + 1)a_{GaSb} = \left(\cos\tau + \frac{\sin\tau}{\tan\delta}\right)a_{GaSb} \tag{4.12}$$

Solving for the in-plane angular distortion α

$$\llcorner = \frac{\pi}{2} \rightarrow \frac{\pi}{2} + \alpha = \frac{\pi}{2} + \tan^{-1}\left(\frac{\sin\tau\tan\tau}{2}\right) = \frac{\pi}{2} + \frac{\tau^2}{2} + \frac{\tau^4}{12} + \cdots \tag{4.13}$$

which is second order in tilt angle. Since the in-plane distortion is very small (second order in tilt angle) the monoclinic distortion can also be approximated by an average tetragonal distortion

$$\overline{\varepsilon_\perp} = \frac{a_{100}}{\bar{a}_\parallel} - 1 = \frac{2\sqrt{2}a_{100}}{d + d\cos\tau} - 1 = \frac{2(\varepsilon_\perp + 1)}{1 + \cos\tau} - 1 = \frac{\varepsilon_\perp - (\cos\tau - 1)/2}{1 + (\cos\tau - 1)/2} \cong \varepsilon_\perp . \tag{4.14}$$

For a coherently strained epilayer, the symmetric (400) XRD reflection provides the lattice distortion in the perpendicular [100] direction relative to the substrate lattice constant a_{GaSb}, which is expressed in terms of the separation of the Bragg peaks $\theta_{GaSb} - \theta_{InAsSbBi}$ as

$$\begin{aligned}\varepsilon_\perp = \frac{a_{100}}{a_{GaSb}} - 1 &= \frac{\sin\theta_{GaSb}}{\sin\theta_{InAsSbBi}} - 1 \\ &= \frac{1}{\cos(\theta_{GaSb} - \theta_{InAsSbBi}) - \sin(\theta_{GaSb} - \theta_{InAsSbBi})\cot\theta_{GaSb}} - 1 \\ &= \frac{1}{\cos(\theta_{GaSb} - \theta_{InAsSbBi})}\left[\frac{1}{1 - \tan(\theta_{GaSb} - \theta_{InAsSbBi})/\tan\theta_{GaSb}}\right] \\ &\quad - 1\end{aligned} \tag{4.15}$$

Expanding to second order and making a first order approximation in peak separation.

$$\varepsilon_{\perp} = \frac{\tan(\theta_{GaSb} - \theta_{InAsSbBi})}{\tan\theta_{GaSb}\cos(\theta_{GaSb} - \theta_{InAsSbBi})} + \frac{\tan^2(\theta_{GaSb} - \theta_{InAsSbBi})}{\tan^2\theta_{GaSb}\cos(\theta_{GaSb} - \theta_{InAsSbBi})}$$

$$+ \frac{1}{\cos(\theta_{GaSb} - \theta_{InAsSbBi})} - 1 + \cdots$$

$$= \frac{\theta_{GaSb} - \theta_{InAsSbBi}}{\tan\theta_{GaSb}} + \frac{(\theta_{GaSb} - \theta_{InAsSbBi})^2}{\tan^2\theta_{GaSb}} + \frac{(\theta_{GaSb} - \theta_{InAsSbBi})^2}{2} \quad (4.16)$$

$$+ \cdots$$

$$= \frac{\theta_{GaSb} - \theta_{InAsSbBi}}{\tan\theta_{GaSb}}\left(1 + \frac{(2 + \tan^2\theta_{GaSb})}{2\tan\theta_{GaSb}}(\theta_{GaSb} - \theta_{InAsSbBi})\right.$$

$$\left. + \cdots\right) \cong \frac{\theta_{GaSb} - \theta_{InAsSbBi}}{\tan\theta_{GaSb}}$$

Although the model indicates a small monoclinic distortion in samples E and F, the difference in the in-plane distortion is too small to be observed experimentally. The XRD simulation provides a simulated lattice constant[20] of

$$a_{100} = \left[\left(\frac{1 - \nu_{InAsSbBi}}{1 + \nu_{InAsSbBi}}\right)\varepsilon_{\perp} + 1\right] a_{GaSb}\,. \quad (4.17)$$

However, since the in-plane strain of a tilted compressively strained epilayer is anisotropic with a slightly larger compressive strain into the step edge, the epilayer intrinsic lattice constant $a_{InAsSbBi}$ is most accurately described using the average in-plane lattice constant $\overline{a_{\parallel}}$ and average tetragonal distortion $\overline{\varepsilon_{\perp}}$, with

$$
\begin{aligned}
a_{InAsSbBi} &= \left[\left(\frac{1-\nu_{InAsSbBi}}{1+\nu_{InAsSbBi}}\right)\overline{\varepsilon_{\perp}}+1\right]\overline{a_{\parallel}} \\
&= \left(\frac{1-\nu_{InAsSbBi}}{1+\nu_{InAsSbBi}}\right)a_{100}+\left(\frac{2\nu_{InAsSbBi}}{1+\nu_{InAsSbBi}}\right)\overline{a_{\parallel}} \\
&= \left(\frac{1-\nu_{InAsSbBi}}{1+\nu_{InAsSbBi}}\right)a_{100}+\left(\frac{2\nu_{InAsSbBi}}{1+\nu_{InAsSbBi}}\right)\left(\frac{1+\cos\tau}{2}\right)a_{GaSb} \\
&= a_{100}-\left(\frac{2\nu_{InAsSbBi}}{1+\nu_{InAsSbBi}}\right)\left(\frac{1-\cos\tau}{2}\right)a_{GaSb} \\
&\cong a_{100}-\left(\frac{2\nu_{InAsSbBi}}{1+\nu_{InAsSbBi}}\right)\frac{\tau^2}{4}a_{GaSb}
\end{aligned}
\tag{4.18}
$$

The epilayer tilt is small in this work and the second order τ^2 and high order terms do not contribute significantly to the analysis. Nevertheless, the tilt can be significant for highly strained epilayers on substrates with large offcut and as such its impact is examined up to second order in this work. In sample D, the epilayer boundary conditions are that it is registered to substrate lattice in-plane and the lattice constant is same as the a_{GaSb}. In sample E and F, because of tilt and monoclinic distortion the in-plane lattice constants are slightly less than substrate lattice constant in the [01$\bar{1}$], and [011] directions. However, measuring these distortions is not possible.

For a tilted strained epilayer when the area scans in reciprocal space maps from (511) reflection are measured, the strain analysis requires the tilt angle, τ to be taken into consideration. The asymmetrical layer reciprocal lattice point must be rotated in the reciprocal space by tilt angle along the ω scan direction to obtain the zero-tilt layer reciprocal lattice point. To obtain the zero-tilt layer reciprocal lattice vector components, consider reciprocal space Bragg's law interpretation from (511) planes of layer as shown in Figure 34.

Incident beam is represented as a wave vector $\vec{k}_{in}$ and the diffracted beam is represented as a wave vector $\vec{k}_{out}$ both with magnitude $1/\lambda$. These wave vectors together define a scattering vector $\vec{q}$ where $\vec{q} = \vec{k}_{in} - \vec{k}_{out}$. The reciprocal lattice vector components for tilted layer are given as

$$|\overrightarrow{q_{\perp}}| = |\vec{q}| \sin[90 - (\theta + \tau) + \omega] = |\vec{q}| \cos(\theta + \tau + \omega) . \tag{4.22}$$

$$\left|\overrightarrow{q_{\parallel}}\right| = |\vec{q}| \cos[90 - (\theta + \tau) + \omega] = |\vec{q}| \sin(\theta + \tau + \omega) . \tag{4.23}$$

Also,

$$\frac{|\vec{q}|}{2} = \vec{k}_{out} \sin(\theta + \tau) . \tag{4.24}$$

$$\left|\vec{k}_{in}\right| = \left|\vec{k}_{out}\right| = \frac{1}{\lambda} . \tag{4.25}$$

$$|\vec{q}| = \frac{2}{\lambda} \sin(\theta + \tau) . \tag{4.26}$$

Substituting the value of $|\vec{q}|$ in the above equations

$$|\overrightarrow{q_{\perp}}| = \frac{2}{\lambda} \sin(\theta + \tau) \cos(\theta + \tau + \omega) . \tag{4.27}$$

$$\left|\overrightarrow{q_{\parallel}}\right| = \frac{2}{\lambda} \sin(\theta + \tau) \sin(\theta + \tau + \omega) . \tag{4.28}$$

Similarly, the reciprocal lattice vector components for substrate are given as

$$|\overrightarrow{q_{\perp}}| = \frac{2}{\lambda} \sin(\theta) \cos(\theta + \omega) . \tag{4.29}$$

$$\left|\overrightarrow{q_{\parallel}}\right| = \frac{2}{\lambda} \sin(\theta) \sin(\theta + \omega) . \tag{4.30}$$

The difference between the reciprocal lattice vector components is given as

$$|\Delta\overrightarrow{q_{\perp}}| = \frac{2}{\lambda} [\sin(2\theta + \omega) \sin^2 \tau - \cos(2\theta + \omega) \sin \tau \cos \tau] . \tag{4.31}$$

$$\left|\Delta\overrightarrow{q_{\parallel}}\right| = -\frac{2}{\lambda}\left[\cos(2\theta+\omega)\sin^2\tau + \sin(2\theta+\omega)\sin\tau\cos\tau\right] . \quad (4.32)$$

The crystallographic tilt of the InAsSbBi layer relative to GaSb substrate, in general, smaller for 1° offcut sample compared to 4° sample. As there are no misfit dislocations, this tilt arises mainly from miscut of the substrate.[49] Experimentally, this tilt has been reported in other systems InGaAs/GaAs,[50,51] InGaAs/GaP,[52] InGaP/GaP,[53] ZnSe/GaAs,[54] ZnSe/Ge,[55,56] CdTe/InSb,[55] and CdZnTe/GaAs.[55]

Small As overpressures of 1% are used during the growth of InAsSbBi to assist Bi incorporation.[5] Furthermore, the excess As that desorbs from the surface is observed to assist with the desorption of excess Bi.[5] However, in all the three samples some of excess Bi accumulates on the surface and segregates, diffuses, and coalesces to form macroscopic droplets resulting in rough, feature covered surfaces.[5] Additionally, the steps formed due to offcut provide possible nucleation sites as near proximity of the step is characterized by large number of nearest neighbors for the arriving atoms to coalesce and form islands in each step.[56] The Schwoebel potential barrier[57] at the step edges can significantly impede the surface diffusion of adatoms between the step's surfaces. Hence, preferential diffusion along the step edges is possible resulting in anisotropic features on the surface.

The phase separation of Bi-rich columns has been discussed in detail in Chapter 3. In the present samples as the growth temperature is held constant at 400°C, the diffusivity of Bi is mainly influenced by the offcut. Further, this is supported by preferential diffusion of adatoms along the step edges. Finally, leading to formation of a chemically homogeneous layer in (100) offcut 1° to (011) sample.

The epilayer tilt expressed in terms of in-plane and out-of-plane layer strain and substrate offcut indicate dependency on Poisson's ratio which previous studies[22] did not consider. Note that the tetragonal distortion can be express in terms of the epilayer strain[4] with

$$\varepsilon_{\perp} = \left(\frac{\varepsilon_{zz} - \varepsilon_{xx}}{1 + \varepsilon_{xx}}\right) = -\varepsilon_{xx}(1 - \varepsilon_{xx}) \left[\frac{1 + \nu_{InAsSbBi}}{1 - \nu_{InAsSbBi}}\right] \tag{4.33}$$

$$= \varepsilon_{zz} \left(\frac{1 + \nu_{InAsSbBi}}{2\nu_{InAsSbBi}}\right)\left(1 + \varepsilon_{zz} \frac{1 - \nu_{InAsSbBi}}{2\nu_{InAsSbBi}}\right). \tag{4.34}$$

where ε_{zz} is the out-of-plane strain and ε_{xx} is the in-plane strain. Therefore, the tilt angle can be expressed in terms of both in-plane and out-of-plane layer strain where Poisson's ratio does not appear, with

$$\tau = \left(\frac{\varepsilon_{zz} - \varepsilon_{xx}}{1 + \varepsilon_{xx}}\right) \tan \delta \, . \tag{4.35}$$

In terms of Poisson's ratio and in-plane strain

$$\tau = -\varepsilon_{xx}(1 - \varepsilon_{xx}) \left[\frac{1 + \nu_{InAsSbBi}}{1 - \nu_{InAsSbBi}}\right] \tan \delta \cong -2.0874 \varepsilon_{xx} \tan \delta \, . \tag{4.36}$$

In terms of Poisson's ratio and out-of-plane layer strain

$$\tau = \varepsilon_{zz} \left(\frac{1 + \nu_{InAsSbBi}}{2\nu_{InAsSbBi}}\right)\left(1 + \varepsilon_{zz} \frac{1 - \nu_{InAsSbBi}}{2\nu_{InAsSbBi}}\right) \tan \delta \cong 1.9196 \varepsilon_{zz} \tan \delta \, . \tag{4.37}$$

4.6 Chapter 4 Summary

The microstructural investigation of InAsSbBi layers grown by molecular beam epitaxy on (100) on-axis, (100) 1° to (011) and (100) 4° to (111) offcut GaSb substrates indicate high-quality, pseudomorphic, defect free layers with sharp interfaces. Excess Bi around 32% of the incident flux accumulates on the surface resulting in the optically rough

3 μm Bi rich droplet covered surfaces. Preferentially oriented surface features along $[01\bar{1}]$ step edge direction are observed for the growth on (100) 1° to (011) offcut substrate. Substrate offcut did not significantly change the Bi incorporation. Lateral modulation in Bi mole fraction is observed on (100) on-axis and (100) 4° to (111)A offcut substrates, which has a step edge density of 2.3×10^6 per cm. Bi composition modulation is not observed in the growth on the (100) 1° to (011) offcut substrate, which has a step edge density of 5.7×10^6 per cm. The layers are compressively strained, and pseudomorphic along with strain induced crystallographic tilt observed on offcut (100) 1° to (011) and (100) 4° to (111)A substrates. A tilt angle model as a function of out-of-plane distortion and the offcut angle is established which agrees well with the measured tilt.

5. STRUCTURAL PROPERTIES OF *InAsSbBi* GROWN ON *GaSb* AT LOW AND HIGH TEMPERATURE

The structural and optical properties of two 210 nm thick InAsSbBi layers grown by molecular beam epitaxy at 280 ºC and 400 ºC on (100) GaSb substrates are investigated using X-ray diffraction, Rutherford backscattering spectroscopy, transmission electron microscopy, and photoluminescence spectroscopy. The Bi mole fraction increases with a decrease in growth temperature. Lateral composition modulation in Bi mole fraction is observed in the layer grown at 400 ºC. The two variants of $CuPt_B$ -type atomic ordering is observed on the {111}*B* planes in the layer grown at 280 ºC. The epilayers are free of observable defects and surface features at both growth temperatures. Superior crystal quality with improved optical quality is realized as the growth temperature increases.

5.1 Samples Studied

This work examines $InAs_{1-x-y}Sb_yBi_x$ samples C and G grown by solid source molecular beam epitaxy at a rate of 15 nm/min on GaSb substrates. The sample cross-section is shown in Figure 5 and discussed in Chapter 1. Sample C has already been discussed in detail in Chapter 3 and is compared here with sample G. Sample G is grown at 280 °C, using V/In flux ratios 0.080 Sb/In, 0.017 for Bi/In, and 0.970 for As/In respectively. Both have droplet free surfaces with (2×4) and (2×3) surface reconstructions observed for sample C and sample G respectively.

5.2 Strain and Composition

The results of coupled $\omega - 2\theta$ XRD scans of the (400) plane are shown in Figure 39 with measured XRD scans given by the solid black curves and simulations by the solid red curves for both samples. The peaks corresponding to the GaSb substrate, and InAsSbBi layer are identified in both samples. Also identified is the Ga(As)Sb buffer peak in sample C. The InAsSbBi layers are nearly lattice matched and coherently strained with a compressive strain of - 0.061% for sample C and a tensile strain of 0.055% for sample G respectively. The InAsSbBi epilayer thickness used in the XRD simulation agrees with the nominal growth calibration of 210 nm in both the samples. Broadening of the InAsSbBi layer peak in the growth at 400 ºC (sample C) indicates fluctuations in the material composition within the layer that is not observed in the growth at 280 ºC (sample G). A lower than expected intensity for the InAsSbBi layer peak and Pendellösung fringes in the growth at 280 ºC indicates diminished interface quality compared to the growth at 400 ºC. The tensile GaAsSb peak in the sample grown at 400 ºC is a result of unintentional incorporation of As in the GaSb buffer. The unintentional As originates from the As background pressure in the growth chamber. Since the As background was lower during the growth at 280 ºC the unintentional As is too small to be observed with XRD.

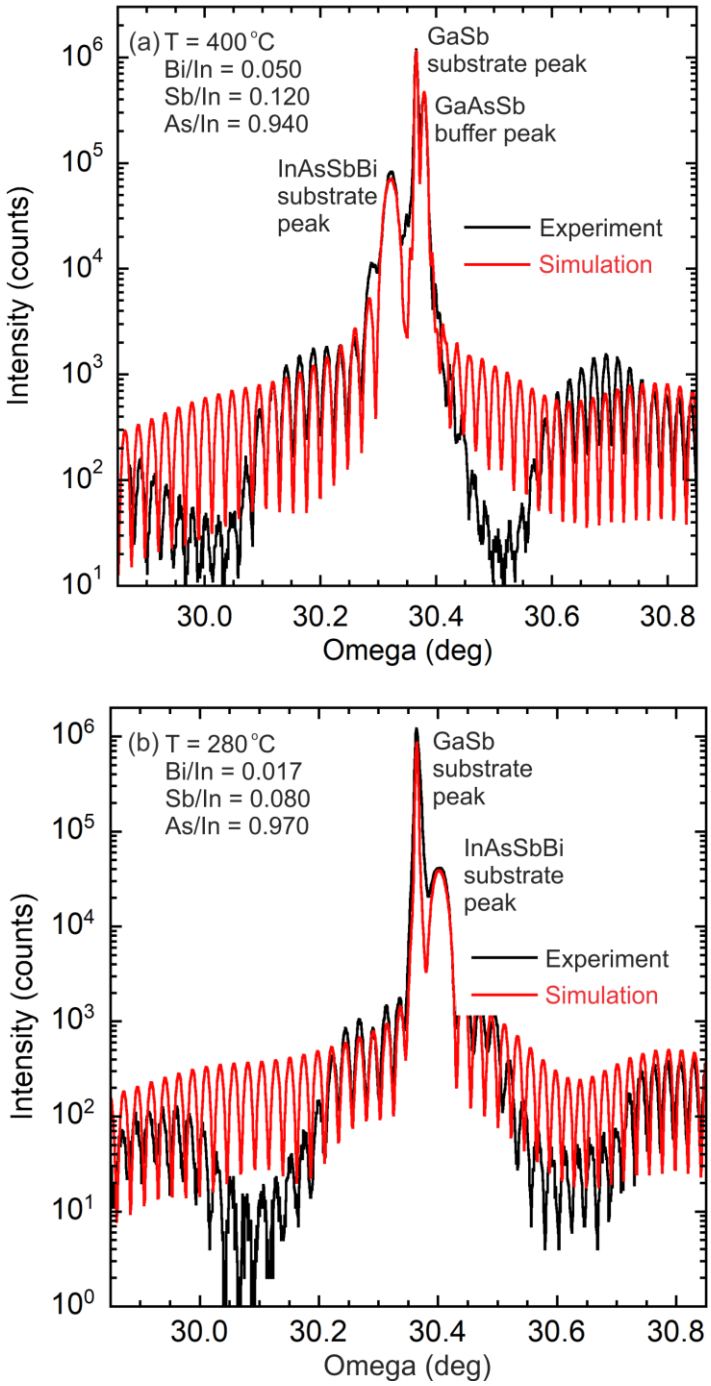

Figure 39: Coupled ω-2θ X-ray diffraction scans from the (400) planes (black curves) and simulations (red curves) from bulk InAsSbBi samples C and G labeled (a) and (b) respectively. The GaSb substrate, strained InAsSbBi peak are identified. Also shown is a GaAsSb buffer peak in the 400 ºC grown sample.

Using the analysis shown in Chapter 3 the Sb mole fraction in InAsSbBi is given by Vegard's law in terms of unstrained InAsSbBi lattice constant and the Bi mole fraction[4] in Equation 3.5. In addition to lattice constant measurements, an accurate measurement of either Bi or Sb mole fraction is required to precisely determine the InAsSbBi layer composition.

Random Rutherford back-scattering spectrometry (RBS) measurements and simulations are performed to determine the Bi mole fraction of the InAsSbBi layers. The measurements and their analysis is shown in Figure 40. The experimental measurements are shown as a solid black curve. The simulated profile is shown as a red solid curve, which is the sum of simulated ion yields for each element shown as solid curves for each element. The simulated Bi mole fractions are 0.4% and 1.6% for samples C and G. The Bi mole fraction x provided by RBS is reported in Table 13. The Sb mole fraction y is determined using Equation 3.5 and the Bi mole fraction. For completeness the As mole fraction is reported as $1 - x - y$. The InAsSbBi sample name, growth temperature, V/In flux ratios, and in-plane bi-axial layer strain are also reported in Table 13. A trend of increasing Bi incorporation with lower growth temperature is apparent, which is attributed to a reduced tendency of Bi to phase separate due to a lower diffusivity at reduced growth temperatures. The Sb incorporation coefficient is 78% for sample C and 75% for sample G. Therefore, the smaller Sb mole fraction in sample G is mainly a result of a smaller Sb flux.

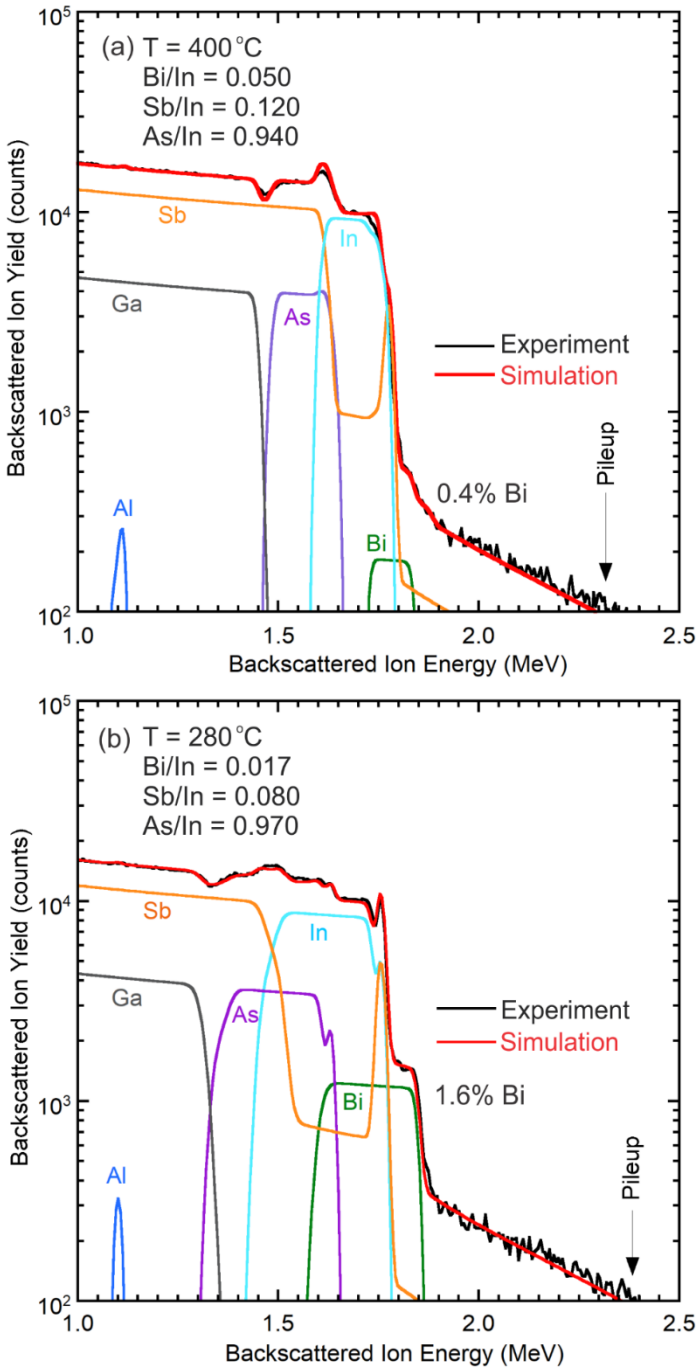

Figure 40: Rutherford backscattering ion yield as a function of backscattered ion energy from the two bulk InAsSbBi samples C and G labeled (a) and (b) respectively. The black curve is the experimentally measured ion yield and the red curve is the aggregate simulated

yield obtained from the sum of the individual simulated ion yields shown for each element as Al (blue), Ga (grey), Sb (orange), As (violet), In (cyan), and Bi (green) respectively.

TABLE 13. InAsSbBi sample name, growth temperature, V/In flux ratios, mole fractions (%) determined from RBS+XRD, and in-plane bi-axial strain.

Sample	Growth temperature	V/In flux ratios			Mole fraction (%)			Strain (%)
		Bi/In	Sb/In	As/In	Bi	Sb	As	
C	400 °C	0.050	0.120	0.940	0.4	9.3	90.3	-0.061
G	280 °C	0.017	0.080	0.970	1.6	6.0	92.4	0.055

5.3 Lateral composition modulation and Atomic ordering

The microstructure of the layers is investigated using cross-section transmission electron microscopy. Low magnification bright field TEM micrographs in the [011] projection from the two InAsSbBi samples are presented in Figure 41. These results show the overall microstructure of the material and indicate that the 210 nm thick InAsSbBi layers have no visible defects over large lateral distances. Contrast modulation is observed in the InAsSbBi layer grown at 400 °C, which is due to variations in the Bi composition with a modulation period of approximately 30 nm. Non-uniform, undulating interfaces are observed in the InAsSbBi sample grown at 280 °C, which is consistent with the observation of reduction of intensity in the XRD patterns.

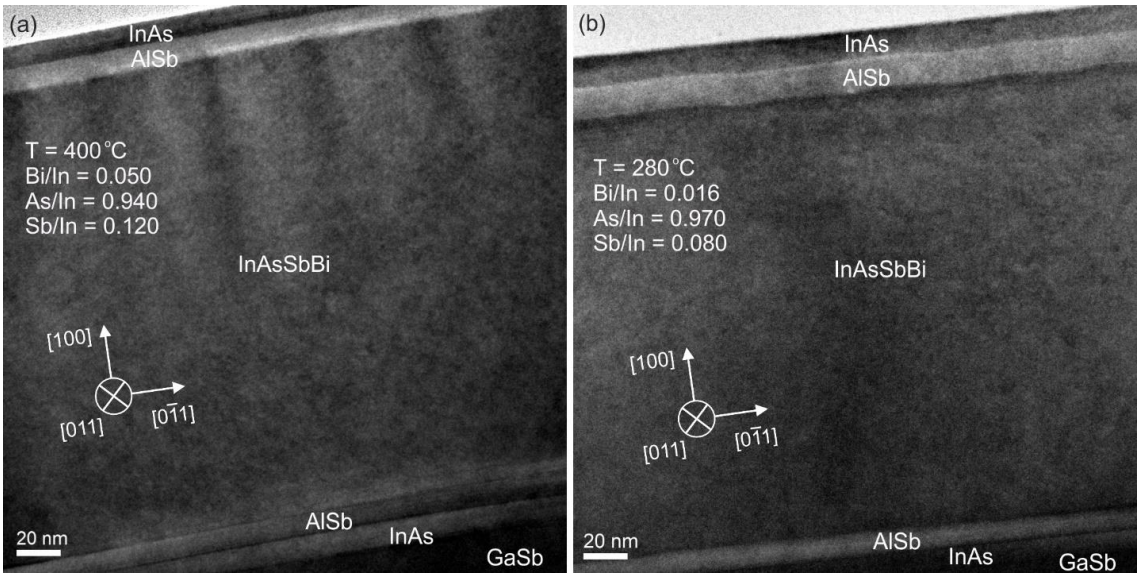

Figure 41: Bright field cross-section TEM images in the [011] projection showing the overall microstructure of the InAsSbBi samples C and G in a and b respectively. Contrast modulations perpendicular to the growth plane in (a) show composition inhomogeneity with a modulation period of approximately 30 nm. The growth temperature, Bi/In, Sb/In, and As/In flux ratios are shown for each sample.

Atomic resolution aberration-corrected high-angle-annular dark-field scanning transmission electron micrographs from samples C and G are shown in Figure 42a and b respectively. Images in the [011] projection show the bottom interfaces of InAsSbBi samples. Indexed fast Fourier transforms (FFT) from the regions marked by white solid squares are shown on the right. Diffraction spots from the (200), (111), and (022) planes in the zinc blende structure are identified in both FFTs. In addition to the main diffraction spots, extra super lattice reflections along the $\frac{1}{2}(11\bar{1})$ and $\frac{1}{2}(1\bar{1}1)$ are seen in the FFT images of the 280 °C layer indicating a $CuPt_B$ type ordering of the As, Sb, and Bi on both sets of $(111)B$ planes. The micrographs indicate that the InAsSbBi layers have no misfit dislocations near the interfaces.

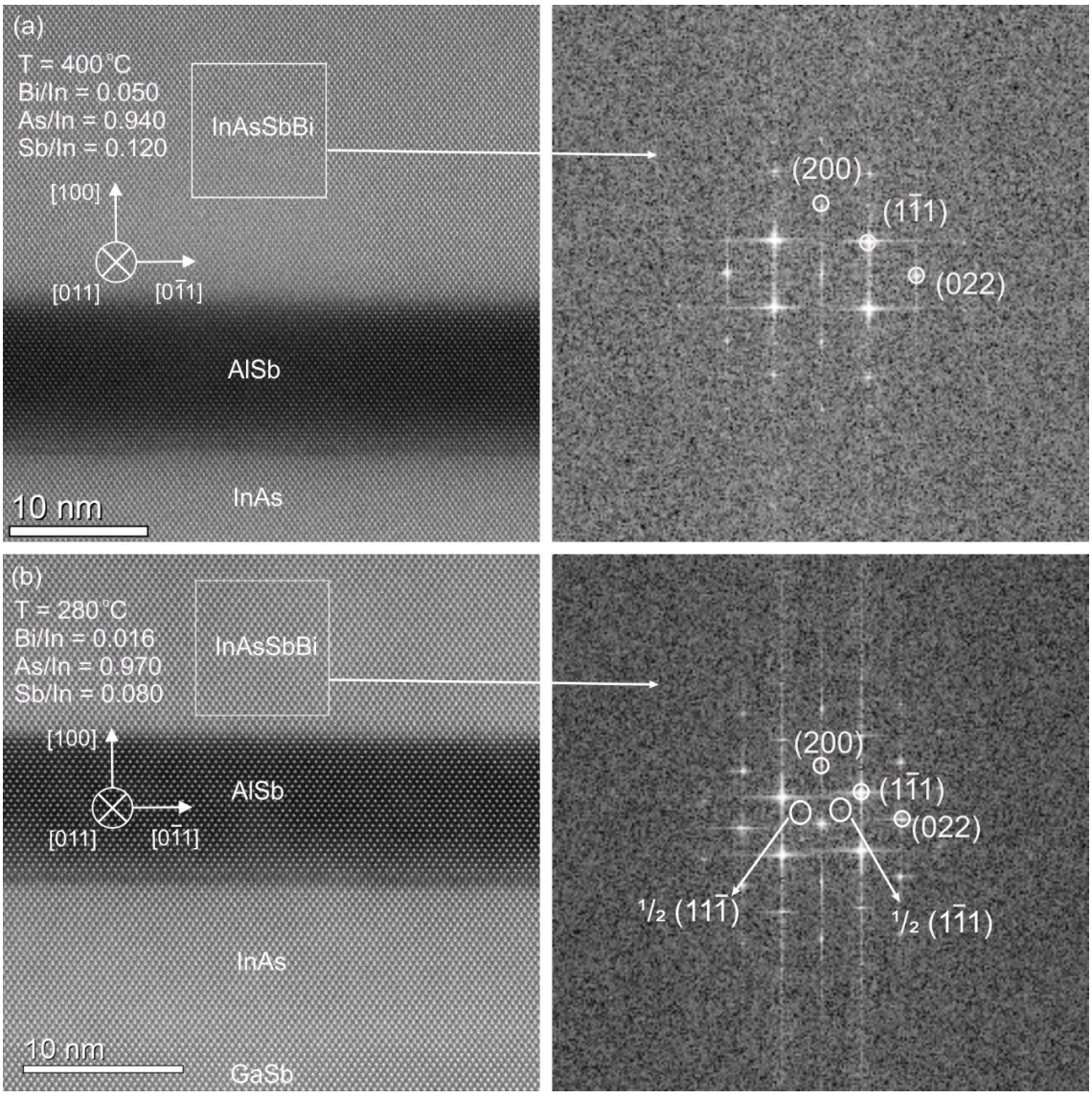

Figure 42: Scanning aberration corrected TEM images in the [011] projection showing the overall microstructure of InAsSbBi samples C and G shown in a and b respectively. Fast Fourier transforms with different diffraction spots from the InAsSbBi layer in both samples. Extra super lattice reflections along the $\frac{1}{2}(11\bar{1})$ and $\frac{1}{2}(1\bar{1}1)$ are seen in the FFT image of the 280 °C layer. The growth temperature, Bi/In, Sb/In, and As/In flux ratios are shown for each sample.

The phase separation of Bi-rich columns has been discussed in detail in Chapter 3. The diffusivity of Bi plays a role and hence the growth temperature influences the development

of these features. At low temperature, reduced diffusivity results in homogeneous Bi incorporation. At high temperature, increased diffusivity of Bi atoms towards Bi rich areas leads to phase separation.

The ordering is a phenomenon that occurs on {111} planes due to the distribution of atomic scale compressive and tensile strain sites. During incorporation at the surface, individual Bi atoms tend to move from nearest neighbors to next-nearest neighbors to minimize strain, thus generating atomic rows of alternating Bi and As. However, with dilute Bi incorporation, only a partially ordered structure is possible. This partial ordering indicates that the large difference in atomic size among the mixed group-V atoms provides a strong driving force for the atomic ordering to occur. No atomic ordering is observed in the 400 ºC grown material due a larger diffusivity and a reduced incorporation of Bi. Previous studies from the literature indicated a similar type of ordering in GaAsBi,[58,59] where $CuPt_B$ type partial ordering of Bi has been reported.

5.5 Photoluminescence

The InAsSbBi samples are examined using temperature-dependent photoluminescence spectroscopy. The measurements are performed at various temperatures ranging from 12 to 295 K using an average pump power of 100 mW that provides an active layer excitation intensity of 120 W/cm^2. Photoluminescence spectra measured for InAs reference sample (black line), 400 ºC grown InAsSbBi sample C (red line), and 280 ºC grown InAsSbBi sample G (blue line) are shown in Figure 43.

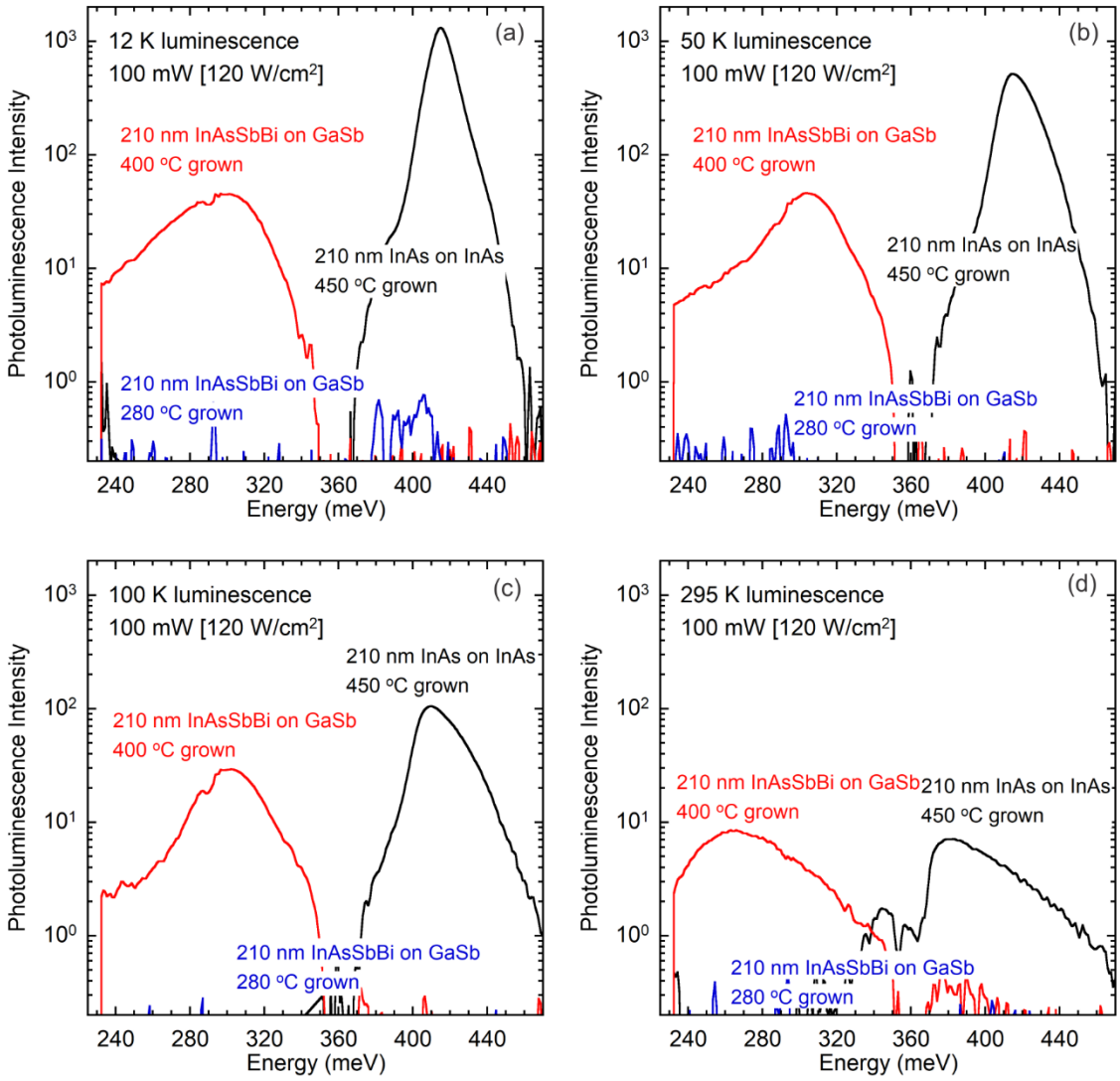

Figure 43: Photoluminescence spectra measured at 12K, 50K, 100K, and 295K with a 100 mW (120 W/cm^2) excitation for InAs reference sample (black line), 400 ºC grown InAsSbBi (sample C) (red line), and 280 ºC grown InAsSbBi (sample G) (blue line).

The 280 °C grown sample fails to luminesce under conditions of high excitation, 100 W/cm^2, and low temperature, 12 K. Further measurements performed at temperatures up to 295 K confirm the low temperature grown material is optically inactive. This is likely due to a high concentration of point defects incurred by low-temperature growth.[60,61] In

contrast, the 400 °C grown sample luminesces at approximately 305 meV (4.06 μm) at low temperature[5] down to excitation densities as low as 4.8 W/cm.

A thermal annealing study was performed on the 280 °C grown sample. Cleaved portions of the sample were thermally annealed in a molecular beam epitaxy chamber for a duration of 5 minutes at temperatures of 400 °C, 500 °C, and 600 °C. The thermal annealing cycle ramped from a baseline temperature of 250 °C to the target anneal temperature at a rate of 50°C/min. No group-V flux overpressure was provided during the annealing cycle. Photoluminescence spectroscopy measurements were performed on the annealed samples. The annealed material also failed to luminesce under conditions of high excitation (120 W/cm^2) and low temperature (12 K).

5.6 Chapter 5 Summary

In summary, the structural and optical properties of InAsSbBi grown at 400 and 280 ºC are compared. The InAsSbBi layers are nearly lattice matched, coherently strained, and either slightly compressive or tensilely strained. The Bi mole fraction is larger in the low temperature grown material as the Bi flux more readily incorporates due to reduced surface segregation and diffusivity. The Sb mole fraction is reduced in sample G mainly due to a 50% lower Sb flux and partially due to a 3% larger As flux that reduced the Sb incorporation rate by 3%. Lateral composition modulation in the Bi mole fraction is observed in the layer grown at 400 ºC due to phase separation of the Bi at high temperature

growth. Improved crystal and optical quality is observed in the material grown at 400 ºC and $CuPt_B$ type atomic ordering is observed on the $\{111\}B$ planes in the material grown at 280 ºC.

6. CONCLUSIONS

The quaternary alloy InAsSbBi grown on commercially available GaSb substrates offers active material that affords independent control of pseudomorphic strain and bandgap energy through the independent adjustment of the Sb and Bi mole fractions. Furthermore, adding Bi offers improved hole confinement compared to InAsSb/GaSb.

This work investigates seven sample structures containing 210 nm thick InAsSbBi layers grown on GaSb substrates by molecular beam epitaxy. These samples are examined using Rutherford backscattering spectrometry, X-ray diffraction, transmission electron microscopy, Nomarski optical microscopy, atomic force microscopy, and photoluminescence. The InAsSbBi layers are observed to be of high-quality, coherently strained, misfit dislocation free, with a Bi mole fraction that ranges from 0.1% to 1.6%. The Bi incorporation coefficient is observed to increase as i) the growth temperature decreases and ii) the As flux decreases.

Lateral composition modulation with around a 30 nm period is observed in the Bi mole fraction when InAsSbBi is i) grown at 400 °C and 420 °C on (100) on-axis substrates and ii) grown at 400 °C on (100) 4° to (111)A substrates. Composition modulation is not observed in low temperature (280 °C) grown InAsSbBi, indicating that high temperature growth enhances the phase separation of Bi. Composition modulation is not observed in high temperature (400 °C) grown InAsSbBi when the (100) substrates are offcut 1° to (011), which has a step edge density of 5.7×10^{5} cm^{-1} indicating reduced phase separation of Bi. Improved crystal and optical quality is observed in the high temperature grown

InAsSbBi and $CuPt_B$ type atomic ordering on the {111}B planes is observed in low temperature grown InAsSbBi.

For high temperature (400, 420, and 430 °C) grown InAsSbBi with 1% excess As overpressures, the excess unincorporated Bi tends to remain on the surface and segregates into Bi rich, 3 μm diameter, droplet features. Increasing the excess As flux to 4%, results in droplet-free surfaces, indicating that desorption of excess As from the growth surface aids in the desorption of excess Bi. A preferential orientation of the large surface droplets along the $[01\bar{1}]$ direction for InAsSbBi grown on (100) substrates offcut 1° toward (011) is attributed to anisotropic diffusion on the surface with less density of step edges (5.7×10^5 cm^{-1}). During low temperature growth, Bi rich droplets are not observed, as the Bi flux incorporates leaving little excess Bi on the surface. For InAsSbBi grown at the highest growth temperature (430 °C) and the highest Bi flux (Bi/In = 0.10), a high density of small, 70 nm diameter, misoriented, zinc-blende, crystals with a 6.55 Å lattice constant are observed on the surface between the large Bi rich droplets. The larger lattice constant indicates that the small surface crystallites contain a much greater Bi mole fraction than the bulk InAsSbBi layer.

Induced crystallographic tilt is observed in and modeled for coherently strained InAsSbBi epilayers grown on offcut (100) 1° to (011) and (100) 4° to (111)A GaSb substrates. It is experimentally observed and shown in the model that the tilt angle is a product of the substrate offcut angle and the out-of-plane distortion of the epilayer. The origin of the observed tilt is explained using a geometric model where in the process of registering to the in-plane and out-of-plane crystal planes at the step edges, a coherently

strained layer grows with a tilt angle relative to the substrate lattice planes in order to accommodate the lattice constant differences at the step edge. Even small crystallographic tilt on the order of 10 arcsec appears in both the symmetric (400) and asymmetric (511) reflections. The tilt angle is directly observable in the offset angle of the symmetric XRD measurement and is used to interpret the measurement of the in-plane reciprocal lattice parameter from the asymmetric reciprocal space maps. The shift due to tilt is modeled in reciprocal space facilitate the direct comparison of the in-plane layer and substrate lattice parameters, thus confirming that the tilted InAsSbBi layers are coherently strained.

REFERENCES

[1]M. A. Kinch, “Fundamentals of Infrared Detector Materials,” SPIE, (2007).

[2]C. Downs and T. E. Vandervelde, "Progress in Infrared Photodetectors since 2000," Sensors **13**, 5054 (2013).

[3]P. T. Webster, A. J. Shalindar, N. A. Riordan, C. Gogineni, H. Liang, A. R. Sharma, and S. R. Johnson, "Optical properties of InAsBi and optimal designs of lattice-matched and strain-balanced III-V semiconductor superlattices," J. Appl. Phys. **119**, 225701 (2016).

[4]P. T. Webster, N. A. Riordan, S. Liu, E. H. Steenbergen, R. A. Synowicki, Y.-H. Zhang, and S. R. Johnson, "Measurement of InAsSb bandgap energy and InAs/InAsSb band edge positions using spectroscopic ellipsometry and photoluminescence spectroscopy," J. Appl. Phys. **118**, 245706 (2015).

[5]S. T. Schaefer, R R. Kosireddy, P. T. Webster, A. J. Shalindar, S. R. Johnson, "Molecular Beam Epitaxy and Optical Properties of InAsSbBi," J. Appl. Phys. **126**, 083101 (2019).

[6]I. Vurgaftman, J. R. Meyer, and L. R. Ram-Mohan, “Band parameters for III-V compound semiconductors and their alloys,” J. Appl. Phys. **89**, 5815 (2001).
[7]J. W. Matthews and A. E. Blakeslee, “Defects in Epitaxial Multilayers: I. Misfit Dislocations,” J. Cryst. Growth **27**, 118 (1974).

[8]M. A. Berding, A. Sher, A. B. Chen, and W. E. Miller, "Structural properties of bismuth-bearing semiconductor alloys," J. Appl. Phys. **63**, 107 (1988).

[9]E. Luna, M. Wu, J. Puustinen, M. Guina, and A. Trampert, "Spontaneous formation of nanostructures by surface spinodal decomposition in $GaAs_{1-x}$ Bi_x epilayers," J. Appl. Phys. **117**, 185302 (2015).

[10]M. Wu, M. Hanke, E. Luna, J. Puustinen, M. Guina, and A. Trampert, "Detecting lateral composition modulation in dilute Ga(As,Bi) epilayers," Nanotechnology **26**, 425701 (2015).

[11]E. Luna, J. Puustinen, M. Wu, J. Hilska, M. Guina, and A. Trampert, " The Role of Epitaxial Strain on the Spontaneous Formation of Bi-Rich Nanostructures in Ga(As,Bi) Epilayers and Quantum Wells," Nanosci. Nanotechnol. Lett. **9**, 1132 (2017).
[12]E. Luna, O. Delorme, L. Cerutti, E. Tournié, J. B. Rodriguez, and A. Trampert, "Microstructure and interface analysis of emerging Ga(Sb,Bi) epilayers and

Ga(Sb,Bi)/GaSb quantum wells for optoelectronic applications," Appl. Phys. Lett. **112**, 151905 (2018).

[13]A. Duzik and J.M. Millunchick, "Surface morphology and Bi incorporation in GaSbBi(As)/GaSb films," J. Cryst. Growth **390**, 5 (2014).

[14]J. Lu, P. T. Webster, S. Liu, Y. H. Zhang, S. R. Johnson, and D. J. Smith, "Investigation of MBE-grown $InAs_{1-x}Bi_x$ alloys and Bi-mediated type-II superlattices by transmission electron microscopy," J. Cryst. Growth **425**, 250 (2015).

[15]A. Trampert, J.-M. Chauveau, K. H. Ploog, E. Tournié, and A. Guzmán, "Correlation between interface structure and light emission at 1.3–1.55 μm of (Ga,In)(N,As) diluted nitride heterostructures on GaAs substrates," J. Vac. Sci. Technol. B Microelectron. Nanom. Struct. **22**, 2195 (2004).

[16]S. A. Islamov, S. B. Evgen'ev, O. V. Sorokina, V. B. Umfitev, and A. V. Mikhailov, "Equilibrium Diagrams in the In-As-Bi and In-P-Bi Systems," Russ. J. Inorg. Chem. **29**, 1355 (1984).

[17]W. K. Chu, J. W. Mayer, and M. A. Nicolet, "Backscattering Spectrometry," Backscattering Spectrom. **37**, 378 (1978).

[18]T. L. Alford, L. C. Feldman, and J. W. Mayer, Fundamentals of Nanoscale Film Analysis (Springer, Hidelberg, 2007), 43-47.

[19]Rutherford Backscattering Spectrometry Analysis Package (RUMP), http://www.genplot.com.

[20]Bernard D. Cullity, Elements of x-ray diffraction (Addison-Wesley, Reading, 1978), 86-88.

[21]X'pert Epitaxy software, PANalytical B. V., Almelo, The Netherlands.
[22]A. J. Shalindar, P. T. Webster, B. J. Wilkens, T. L. Alford, and S. R. Johnson, "Measurement of InAsBi mole fraction and InBi lattice constant using Rutherford backscattering spectrometry and X-ray diffraction," J. Appl. Phys. **120**, 145704 (2016).

[23]P. P. Ewald, "International Tables for X-Ray Crystallography," Nature **171**, 4361 (1953).

[24]J. C. H. Spence, High-resolution electron microscopy, 3rd ed. Oxford: Oxford University Press, (2009).

[25]D. Williams and C. Carter, Transmission Electron Microscopy: A Textbook for Materials Science. (Boston, MA: Springer US, 2009).

[26]D. J. Smith, Instrumentation and Operation for High-Resolution Electron Microscopy 11. Academic Press Limited, (1989).

[27]S. J. Pennycook et al., "Aberration-corrected scanning transmission electron microscopy: from atomic imaging and analysis to solving energy problems," Philos. Trans. R. Soc. A Math. Phys. Eng. Sci. **367**, 1903 (2009).

[28]R. F. Egerton, Electron energy-loss spectroscopy in the electron microscope (New York: Plenum Press, 1996).

[29]J. M. Cowley, "Image contrast in a Transmission Scanning Electron Microscope," Appl. Phys. Lett. **15**, 58, (1969).

[30]L. Reimer, Transmission electron microscopy : physics of image formation and microanalysis, 4th ed. Berlin ; New York: Springer, (1997).

[31]A. V Crewe and J. Wall, "A scanning microscope with 5 Å resolution," J. Mol. Biol. **48**, 375, (1970).

[32]D. R. Schmitt, "Characterization of high-quality surfaces by Nomarski microscopy and light scattering," Precis. Eng. **13**, 263 (1991).

[33]G. Haugstad, Atomic Force Microscopy: Understanding Basic Modes and Advanced Applications (Wiley, New Jersey, 2012), 1–18.

[34]R. R. Kosireddy, S. T. Schaefer, A. J. Shalindar, and S. R. Johnson, "Microstructure and surface morphology of InAsSbBi grown by molecular beam epitaxy," J. Appl. Phys. **126**,095108 (2019).

[35]P. T. Webster, A. J. Shalindar, S. T. Schaefer, and S. R. Johnson, "Bandgap and composition of bulk InAsSbBi grown by molecular beam epitaxy," Appl. Phys. Lett. **111**, 082104 (2017).

[36]R. R. Kosireddy, S. T. Schaefer, A. J. Shalindar, P. T. Webster, and S. R. Johnson, "Examination of the Structural Quality of InAsSbBi Epilayers using Cross Section Transmission Electron Microscopy," Microsc. Microanal. **24**, 36 (2018).

[37]R. D. Twesten, D. M. Follstaedt, S. R. Lee, E. D. Jones, J. L. Reno, J. M. Millunchick, A. G. Norman, S. P. Ahrenkiel, and A. Mascarenhas, "Characterizing composition modulations in InAs/AlAs short-period superlattices," Phys. Rev. B **60**, 13619 (1999).

[38]E. G. Bithell and W. M. Stobbs, "Composition determination in the GaAs/(Al, Ga)As system using contrast in dark-field transmission electron microscope images," Philos. Mag. A **60**, 39 (1989).

[39]P. A. Doyle and P. S. Turner, "Relativistic Hartree–Fock X-ray and electron scattering factors," Acta Crystallogr. Sect. A **24**, 390 (1968).

[40]Z. R. Wasilewski, M. M. Dion, D. J. Lockwood, P. Poole, R. W. Streater, and A. J. SpringThorpe, "Composition of AlGaAs", J. Appl. Phys. **81**, 1683 (1997).

[41]L Vegard, "Die Konstitution der Mischkristalle und die Raumfüllung der Atome", Z. Phys **5**, 17-26 (1921).

[42]E. Luna, M. Wu, M. Hanke, J. Puustinen, M. Guina, and A. Trampert, "Spontaneous formation of three-dimensionally ordered Bi-rich nanostructures within GaAs1-xBix/GaAs quantum wells," Nanotechnology **27**, 325603 (2016).

[43]M. P. Barde and P. J. Barde, "What to use to express the variability of data: Standard deviation or standard error of mean?," Perspect. Clin. Res. **3**, 113 (2012).

[44]M. Wu, E. Luna, J.Puustinen, M. Guina. and A. Trampert, "Formation and phase transformation of Bi-containing QD-like clusters in annealed GaAsBi," Nanotechnology **25**, 205605 (2014).

[45]L. Wang, L. Zhang, L. Yue, D. Liang, X. Chen, Y. Li, P. Lu, J. Shao, and S. Wang, "Novel Dilute Bismide, Epitaxy, Physical Properties and Device Application," Crystals **7**, 63 (2017).

[46]L. Dominguez, D. F. Reyes, F. Bastiman, D. L. Sales, R. D. Richards, D. Mendes, J. P. R. David, and D. Gonzalez, "Formation of Tetragonal InBi Clusters in InAsBi/InAs(100) Heterostructures Grown by Molecular Beam Epitaxy," Appl. Phys. Express **6**, 112601 (2013).

[47]R. K. Tsui, J. A. Curless, G. D. Kramer, M. S. Peffley, and D. L. Rode, "Effects of substrate misorientation on the properties of (Al, Ga)As grown by molecular beam epitaxy," J. Appl. Phys. **58**, 2570 (1985).

[48]D. J. Smith, J. Lu, T. Aoki, M. R. McCartney, and Y. H. Zhang, "Observation of compound semiconductors and heterovalent interfaces using aberration-corrected scanning transmission electron microscopy," J. Mater. Res. **32**, 921 (2017).
[49]J.E. Ayers, S.K. Ghandhi and L.J. Schowalter, "Crystallographic tilting of heteroepitaxial layers," J. Cryst. Growth **113**,430 (1991).

[50]H. Nagai, "Structure of vapor-deposited $Ga_xIn_{1-x}As$ crystals," J. Appl. Phys. **45**, 3789 (1974).

[51]G.H. Olsen and R.T. Smith, "Misorientation and tetragonal distortion in heteroepitaxial vapor-Grown III–V structures," Phys. Status Solidi A **31**, 739 (1975).

[52]A. Ohki, N. Shibata and S. Zembutsu, "Nitrogen Doped p-Type ZnSe Layer Grown by Metalorganic Vapor Phase Epitaxy," J. Appl. Phys. **64**, 694 (1988).

[53]J. Kleiman, R.M. Park and HA. Mar, "On epilayer tilt in ZnSe/Ge heterostructures prepared by molecular-beam epitaxy," J. Appl. Phys. **64**, 1201 (1988).

[54]E. Yamaguchi, I. Takayasu, T. Minato, and M. Kawashima, "Growth of ZnSe on Ge(100) substrates by molecular-beam epitaxy," J. Appl. Phys. **62**, 885 (1987).
[55]I.B. Bhat, K. Patel, N.R. Taskar, J.E. Ayers and S.K.Ghandhi, "X-ray diffraction studies of CdTe grown on InSb," J. Cryst. Growth **88**, 23 (1988).

[56]J. Tersoff,"Step Energies and Roughening of Strained Layers," Phys. Rev. Lett. **74**, 4962 (1995).

[57]Richard L. Schwoebel, Edward J. Shipsey, "Step Motion on Crystal Surfaces," J. Appl. Phys. **37**, 3682 (1966).

[58]A. G. Norman, R. France, and A. J. Ptak,"Atomic ordering and phase separation in MBE $GaAs_{1-x}Bi_x$," J. Vac. Sci. Technol. B **29**, 03C121 (2011).

[59]D. F. Reyes, F. Bastiman, C. J Hunter, D. L. Sales, A. M. Sanchez, J. P. R. David, and D. Gonzalez,"Bismuth incorporation and the role of ordering in GaAsBi/GaAs structures," Nanoscale Research Letters **9**, 23 (2014).

[60]W.-X. Ni, W. M. Chen, I. A. Buyanova, A. Henry, G. V. Hansson, and B. Monemar, "Some critical issues on growth of high quality Si and SiGe films using a solid-source molecular beam epitaxy system," J. Cryst. Growth **157**, 242 (1995).

[61]M. H. Chan, S. K. So, K. T. Chan, and F. G. Kellert, “Defect density measurements of low temperature grown molecular beam epitaxial GaAs by photothermal deflection spectroscopy,” Appl. Phys. Lett. **67**, 834 (1995).

[62]T.Tiedje, E. C. Young, and A. Mascarenhas, “Growth and properties of the dilute bismide semiconductor $GaAs_{1-x}Bi_x$ a complementary alloy to the dilute nitrides,” International J.Nanotechnology . **5**, 963 (2008).

APPENDIX A

PUBLICATIONS

[1] D. Holec, Rajeev R. Kosireddy, T. Klein, H. Clemens, “Preferential site occupancy of alloying elements in TiAl-based phases,” J. Appl. Phys. **119**, 205104, published May 2016; 9 pages

[2] Rajeev R. Kosireddy, Stephen T. Schaefer, Arvind J. Shalindar, Preston T. Webster, Shane R. Johnson, “Examination of the Structural Quality of InAsSbBi Epilayers using Cross Section Transmission Electron Microscopy,” Microscopy and Microanalysis 24 (S1), 36-37, published Aug 2018; 2 pages

[3] Stephen T. Schaefer, Rajeev R. Kosireddy, Preston T. Webster, and Shane R. Johnson, “Molecular beam epitaxy and optical properties of InAsSbBi,” J. Appl. Phys. **126**, 083101 (2019), published Aug 2019; 15 pages

[4] Rajeev R. Kosireddy, Stephen T. Schaefer, Arvind J. Shalindar, and Shane R. Johnson, “Microstructure and surface morphology of InAsSbBi grown by molecular beam epitaxy,” J. Appl. Phys. **126**, 095108 (2019), published September 2019; 14 pages

[5] Stephen T. Schaefer, Shang Gao, Preston T. Webster, Rajeev R. Kosireddy, and Shane R. Johnson, “Absorption edge characteristics of GaAs, GaSb, InAs, and InSb,” accepted J. Appl. Phys.

[6] Rajeev R. Kosireddy, Stephen T. Schaefer, Marko S. Milosavljevic, and Shane R. Johnson, “Structural properties of InAsSbBi epilayers grown by molecular beam epitaxy on offcut GaSb substrates,” to be submitted to J. Appl. Phys.

[7] Rajeev R. Kosireddy, Stephen T. Schaefer, Preston T. Webster, and Shane R. Johnson, “Atomic ordering and phase separation in InAsSbBi epilayers grown by molecular beam epitaxy on GaSb substrates,” to be submitted to Appl. Phys. Lett.